České vysoké učení technické v Praze

Fakulta elektrotechnická

Katedra řídicí techniky

The role of structural dynamics in energy dissipation and layer exfoliation in Transition Metal Dichalcogenides

---

Doctoral Thesis

submitted by

Florian Belviso

for the degree of *Doctor of Philosophy*

Ph.D. Program: P0533D110030 - APPLIED PHYSICS

Supervisor: **Dr. Antonio Cammarata**

July 2021

"The best that most of us can hope to achieve in physics is simply to misunderstand at a deeper level."

Wolfgang Pauli

Acknowledgements

Aux miens, que j'emporte où que j'aille.

I would like to take the opportunity to thank all the people from Advanced Material Group in Prague. From the precious insights about scientific techniques, to the out of control and unspeakable discussions, this working and human environment was the best a rookie scientist could hope for.

To Štěpánka, our beautiful nanny, for her competence and efficiency in solving all the problems that the gods of administration tried to throw at us.

To Tomáš and his distant but constant supervision, for knowing to push when necessary.

To my Drunkle Paolo, for sharing his advice and knowledge with me, along with his time (a scarce resource in the world of research).

To my friend Ben, who is always ready to give a hand, and have the patience to correct my frenglish.

To my supervisor Antonio, for his time and assistance, for helping me to improve myself. A scientist to look up to, on top of being one of the nicest person i know.

To Eric Bousquet and his fellow colleagues of ABINIT team, for welcoming me and teaching me about methods and code implementation, and being involved in my doctoral examination.

To the people of the SOLUTION project, for the conferences, the exchanges and the adventures.

Finally, this project has received funding from the European Union's Horizon2020 research and innovation programme under grant agreement No. 721642: SOLUTION. This work has been done with the support of the Czech Science Foundation (project No. 17-24164Y), and by the project "Novel nanostructures for engineering applications" No. CZ.02.1.01/0.0/0.0/16 026/0008396. This work was also supported by The Ministry of Education, Youth and Sports from the Large Infrastructures for Research, Experimental Development and Innovations projects "e-Infrastructure CZ — LM2018140" and e-INFRA CZ (ID:90140).

Summary

In materials science, understanding friction between surfaces is challenging, as it calls for a multiscale approach. Yet, finding ways to control the friction at the nanoscale is a growing necessity for the fabrication and operation of optimal nano-engineered devices.

Throughout this thesis, the author demonstrates how the use of external electric fields and contaminant molecules can influence the frictional behaviour of MX_2 Transition Metal Dichalcogenides. The study is based on Density Functional Theory calculations and phonon spectrum analysis of the considered materials. Electronic descriptors allow us to describe the changes in the electronic structures, while we quantify the dynamical response in terms of atomic participations to the vibrational behavior. We present the theoretical tools and the methodology used, along with the computational details.

Three distinct investigations are described in the Results part. The first study examines the effect of an electrostatic field on the frictional properties of the material. The analysis shows that a specific charge accumulation within the material favors the relative layer sliding, hence reduces the nanoscale friction. A second study discusses the effect of the intercalation of N_2 and CO_2 contaminants on the same materials, and how the valence band is correlated to the layer-layer frictional response. Finally, the third study shows how the insertion of an N_2 contaminant molecule in the interlayer region of the systems can stabilise the frictional response of the materials exposed to an electrostatic field.

The obtained results constitute guidelines on how to select proper fields and contaminants to design new tribological materials with a customized frictional response.

Souhrn

Pochopení jevu tření mezi dvěma materiály je v oboru materiálového inženýrství náročné, protože vyžaduje velmi komplexní přístup. Pro výrobu a provoz nanotechnologických zařízení je třeba stále více řešit způsoby řízení třecího procesu v nanoměřítku.

Tato práce je zaměřena na studium vlivu vnějších elektrických polí a vlivu přítomnosti cizích částic na třecí vlastnosti materiálů na bázi dichalkogenidů přechodových kovů MX_2. Analýzy jsou založeny na výpočtech metodou teorie funkcionální hustoty (DFT) a na studiu fononových spekter těchto materiálů. S využitím elektronických deskriptorů je možné popsat změny elektronických struktur a zároveň kvantifikovat jejich dynamickou odezvu ve smyslu příspěvku jednotlivých atomů do vibračních spekter. Práce prezentuje použité teoretické nástroje, metodiku výpočtů a další detaily.

Praktická část práce je členěna do třech částí. V první části jsou popsány výsledky studia vlivu elektrostatického pole na třecí vlastnosti materiálu. Tato analýza ukázala, že akumulovaný měrný náboj v materiálu zlepšuje skluz vrstev, což vede ke snížení tření v nanoměřítku. Druhá část je zaměřena na vliv interkalace cizích částic (N_2 a CO_2) do MX_2 materiálu a dále na korelaci vlastností valenčních pásů s třením mezi jednotlivými vrstvami materiálu. Poslední část popisuje vliv molekuly N_2 vložené mezi vrstvy materiálu MX_2 na zlepšení a stabilizaci třecích vlastností materiálu v přítomnosti vnějšího elektrostatického pole.

Výsledky této práce přinášejí ucelený postup volby vhodných elektrostatických polí a cizích částic při vývoji nových tribologických materiálů s řízenou třecí odezvou.

Contents

Chapter 1

Introduction

In 2004, the experimental proof of the achievability of creating free-standing graphene layers [1] started a new era in materials science. Graphene is the first representative compound of a new class of materials possessing extraordinary different properties compared with those with conventional bulk. It exibits strong anisotropy [2] and reduced dimensionality, the latter yielding singular quantum effects and outstanding mechanical properties [3, 4]. This made it a prime candidate in many fields of applications. For example, graphene filled into polymer matrices can significantly increase the mechanical resistance to shear stress [5]. Single-layer graphene electrodes are used to develop new organic n-type FET transistors (OFETs) based on Chemical Vapor Deposited graphene sheets [6]. Since then, the search of atomically thin materials "beyond graphene" have been fruitful. Several non-graphene elemental 2D-analogs, like silicene [7] and phosphorene [8], have been successfully produced. Many other compounds, that have been predicted or synthesized in atomically thin form, were later introduced in this expanding list [9]. Thousands of 2D materials have been proposed by computational studies [10], while dozens of them have already been synthesized. So far, 15 groups of compounds have been distinguished, depending on the possible applications (Figure 1.1). Apart from their mechanical, optical and electronic properties, 2D materials are interesting also for their applications in biology [11] and in tribology [12, 13].

Tribology is the science of friction, wear and lubrication, focusing on phenomena occurring at the contact zone between two surfaces in relative motion. Despite the fact that tribological contacts are responsible for about 23% of the world's total energy consumption [14], friction phenomena are still not well understood at the nanoscale; a total control of the tribological processes is then paramount for a sustainable worldwide development [15]. Many 2D materials are excellent solid lubricants, and are used in a range of applications where pressure or temperature

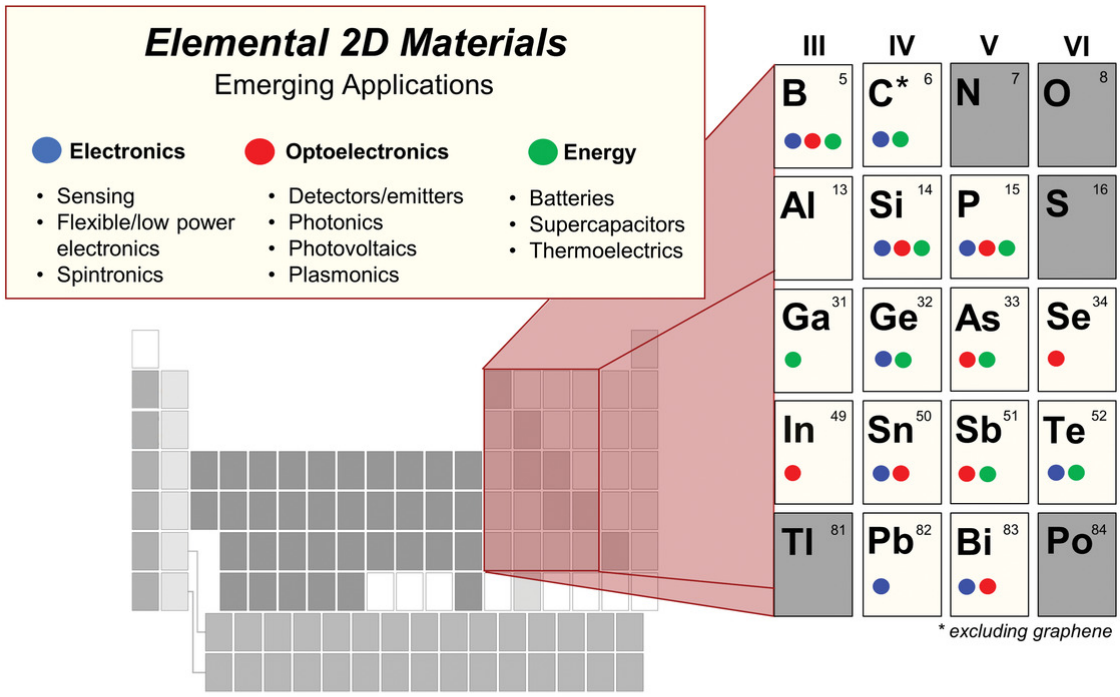

Figure 1.1: Arrangement of the various elements implied in 2D applications. Figure reproduced from [9].

conditions exclude the use of fluids [16, 17]. The idea is to create a coating at the surface of contact between the moving parts of a device, using low friction compounds. Unfortunately, due to mechanical pressure, these materials can wear out very rapidly, often preventing their use at large scales.

The knowledge of the frictional behavior of 2D materials is also of utmost importance when designing microscale devices that operate at nanoscale precision, such as nanogenerators and Micro/Nano Electro Mechanical Systems (MEMS/NEMS) [18, 19]. Because of their size, such devices often require the use of atomically thin layers of material to favor the motion of some parts and extend their lifetime. These layers can be obtained from the bulk material in several ways, such as adhesive-tape technique [20] or chemical exfoliation with ion intercalation [21, 22], to name a few. Developing such methods requires a precise understanding of the frictional behavior of materials down to the nanoscale; however, the microscopic mechanisms determining how the single layers are separated from the bulk material remain unclear.

Among the 2D compounds, the Transition Metal Dichalcogenides (TMDs) are a family of materials that have shown a wide range of applicability in the last decade. The TMD structure consists of hexagonally-ordered planes of M cations (transition metal), inserted between two hexagonally-ordered planes of X anions (chalcogens).

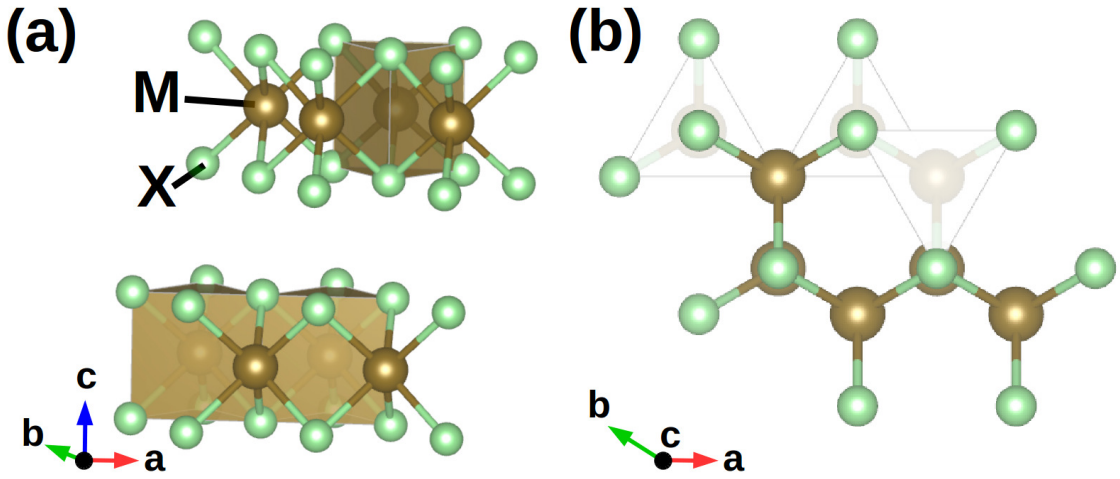

Figure 1.2: Model structure of the hexagonal $P6_3/mmc$ 2H polymorph of the MX_2 crystal. The **a**, **b**, **c** vectors represent the crystallographic axes, indicating the cell relative orientation. M stands for transition metal atom, X for chalcogen atom. The parallel layers are bounded by weak van der Waals forces. (a) View of the interlayer plane; (b) top view of the plane perpendicular to the lattice vector **c**.

This layered motif produces X-M-X "sandwiches", held together by weak van der Waals forces and yielding a lamellar structure (Figure 1.2). This type of structure is responsible for their lubricating properties, by allowing the parallel sliding of one layer with respect to the other. In passing, we mention that they have other applications such as in photovoltaic devices, lithium ion batteries, hydrogen evolution catalysis, transistors, photodetectors, DNA detection, and memory devices [23, 24, 25, 26, 27, 28, 29, 30]. If one considers heterostructures, the chemical and structural complexity is increased even more. The alternation of strong intralayer covalent bonds and weak van der Waals interlayer coupling makes it relatively easy to manipulate layers or 2D flakes and to vertically stack them, in order to build devices for different applications [2, 31]: the number of possible combinations then becomes virtually infinite (Figure 1.3).

The focus of this work is on the tribological properties of prototype materials, which originates from the sliding between layers at the atomic scale. The investigated materials are transition metal dichalcogenides with general stoichiometry MX_2 (Figure 1.2). The theoretical description of friction in this regime is challenging, as the electronic structure plays an important role, either directly contributing to the energy dissipation or indirectly when determining the geometry of the interface. Quantum mechanical computational methods cannot reach the timescale of sliding events and effectively explore out-of-equilibrium phenomena, like the stick-slip motion [32, 33]. Approaches found in the literature rely on parameterised clas-

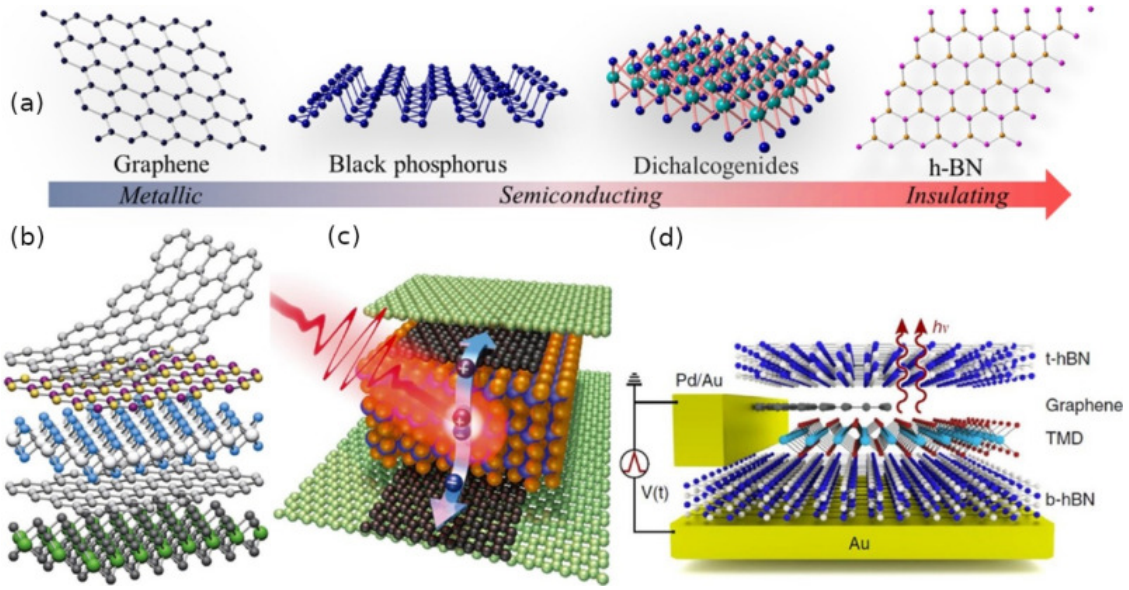

Figure 1.3: (a) Schematic illustrations of prototypical 2D materials ranging from metallic to insulating. Each layer can be seen as a building block for fabrication of complex 2D van der Waals heterojunctions. (b) Schematic diagram of a general 2D vdW "LEGO®" heterostructure. (c) Photoexcited carrier dynamics in a heterostructure made of h-BN/G/WSe2/G/h-BN. Pulsed-laser excitation generate excitons (electron–hole pairs), separated and transfered to the graphene electrodes. (d) h-BN/Graphene/TMD/h-BN device created by sandwiching the monolayer TMD and graphene between two multilayer h-BN flakes. Picture adapted form Ref.[31].

sical potentials (*Force Fields*) and classical Molecular Dynamics (MD) simulations able to investigate systems and timescales far larger than their quantum counterparts [34, 35], or they estimate the frictional behavior from equilibrium properties, like phonon-spectrum based descriptors [36, 37]. The latter will be the one that interests us the most here.

The question to formulate is the following: can we develop a procedure in order to have a deeper understanding of the entanglement between the electro-dynamic features of TMD systems and their nanofrictional response? Among all the studies dealing with TMDs, only a few of them were devoted to the tribological aspects involved in these materials [38, 39, 40]. A few studies showed how to modify the frictional behaviour between TMD layers by means of external load or charge injection [41, 36, 42]. Yet, further investigations of the consequences of the electro-phonon coupling is necessary.

In the thesis presented here, we also consider the presence of an electrostatic field and how it affects the layer sliding events. Some anterior theoretical studies have dealt with the effect of electric fields on the optical, electric or vibrational

characteristics of MoS_2 [43, 44, 45]. A first experimental study has shown that electric fields can be used to change the frictional properties. On KBr or NaCl surfaces, it was shown that selective excitations of mechanical resonances reduced the friction force in particular ranges of field and load, perpendicular to the direction of sliding [46]. In 2015, an experimental work proposed a method for the manipulation of free-standing atomic layers of MoS_2 using an Atomic Force Microscope (AFM) tip to create an in-plane potential gradient [47]. In 2019, an experimental result showed that the friction between an AFM tip and flakes of 2D MoS_2 decreases with the application of an in-plane potential gradient [33]. In this context, the present theoretical work aims to provide guidelines for the development of new protocols using the electrostatic field as a knob to adjust the frictional behavior of TMDs. By investigating how the mode frequencies change the electro-vibrational coupling, we will be able to identify the nanoscale contributions to the macroscopic frictional properties and finally design new TMDs with a targeted tribological response.

Chapter 2

Simulations and scales

In this chapter, we briefly mention the main types of numerical methods used to simulate physical systems. These methods vary with the scale of the problem, and rely accordingly on classical or quantum descriptions. As such, some methods are more adapted to describe sliding events at the macroscopic scale (involving billions of atoms), or to bridge the gap between the micro and the macroscopic scale (mesoscopic scale), e.g. the Finite Elements Methods (FEM). While they are suitable for studying structural material deformations, they fail to give a proper description at the nanoscale. Nonetheless, in the context of NEMS/MEMS design, a complete theoretical description of the system with atomic details is necessary. The electronic structure indeed plays a direct role in the friction response, or an indirect one by influencing the geometry at the interface. This is where ab initio techniques must be used; however, these methods cannot be employed to simulate timescales of about 2 ns or system sizes of approximately 40 nm, because they are computationally very demanding. Molecular Dynamics approaches are able to treat much larger systems and timescales, and have the advantage of having a high scalability; the price to pay is the loss of the electronic detail and the description of the quantum effects. The various techniques and their associated time and length scales used to study the tribological response are summarized in Figure 2.1. For the systems discussed herein, the quantum mechanical treatment is mandatory.

2.1 Finite Elements

In order to understand and quantify the friction response occurring in continuous media, i.e., those where the atomic detail is not relevant, the Finite Elements Method (FEM) [49] is one of the numerical frameworks that is used. According to the kind of mechanical equations to solve (elliptic, hyperbolic or parabolic), it can

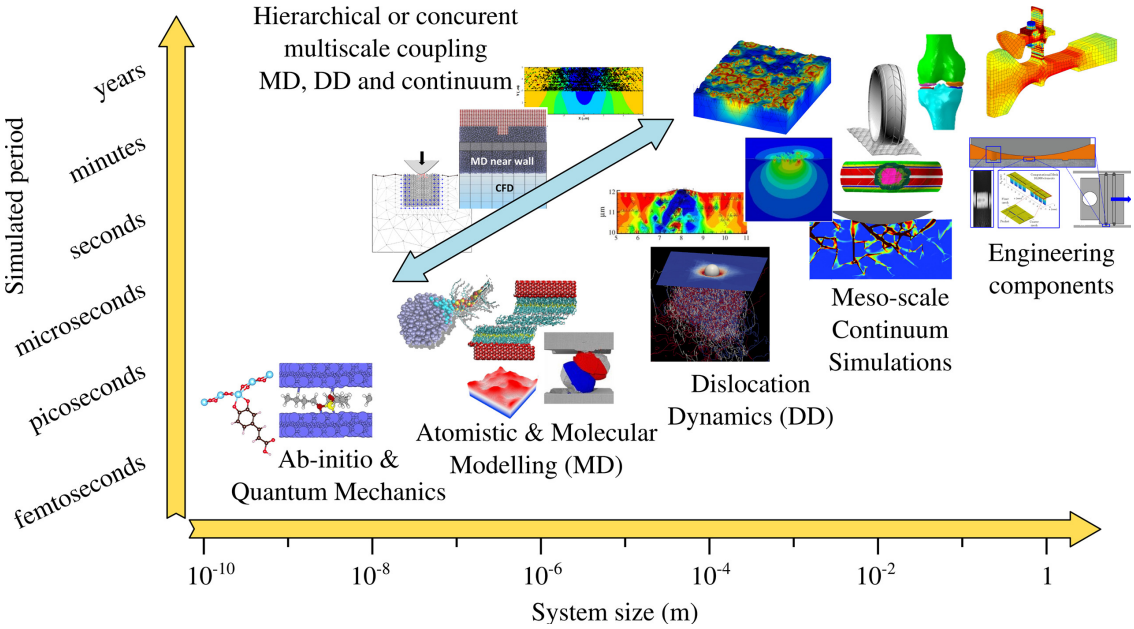

Figure 2.1: Diagram highlighting the general use of models developed in tribology as a function of time- and length-scale. Developing predictive tools in tribology calls for multiscale approaches. Figure reproduced from Ref. [48]

be necessary to vary the numerical procedures. The FEM procedure steps can be summarized as:

- Discretize the space by using a linear piece-wise approximation, hence the use of "finite elements"; numerically, this implies the choice of a mesh.
- Select functions to interpolate the field variables over the element. Often, polynomials are selected as interpolation functions. The degree of the polynomial depends on the number of nodes assigned to the element.
- Find the element properties. The matrix equation for the finite element should be established by relating the nodal values of the unknown function to other parameters. The used approaches can be of variational kind or of the Galerkin kind [50].
- Assemble the element equations to find the global equation system for the whole solution region. It requires the combination of local element equations for all the elements used for the discretization. Element connectivities are used for the assembly process and boundary conditions are imposed.

The principle of energy minimization, like in other frameworks, is central here [51]. The idea is that when a boundary condition is applied to the system (like a force for example), of all the possible configurations that the system can take, only the

configuration corresponding to a minimum of the energy can be considered to be the actual solution. For example, a multiscale model and study of roughness and friction between multilayer surfaces was made possible using FEM, allowing to predict the static friction coefficient, and taking into account the roughness of the contact area, the latter never being perfectly flat [39]. The time scales accessible with FEM allow for the study of the wear and abrasion at the interface between two "real sized" surfaces of coating, that is, following the sliding event across a distance up to the order of the mm. For example, it is possible to simulate a scratch sliding test on a CrAlSiN film, over a distance of few hundreds of μm and at speeds of about a tenth of ms^{-1} [52], or the tribological properties (friction coefficient and abrasive wear) of aluminum oxide nano-layers [53].

2.2 Molecular Dynamics

When the details of the electronic structure are not important for our purposes and we need to look at the system behavior with atomic detail, Molecular Dynamics methods are used. These methods allow simulations of systems involving up to one million atoms [54, 55, 56], but this comes at a computational cost. The other factor increasing the computational cost of an MD simulation is the size of the time step. In liquids and solids, if one wants to simulate the dynamics of the system, it is necessary to track the vibrational motion of atoms. This limits the time steps to the order of the femtosecond, which means that thousands of those time steps are required to simulate a picosecond of a real life event. These constraints on the number of atoms and time steps have lead to a lot of research and development for optimizing MD simulations for use on high performance computing clusters. Software packages such as NAMD [57] and LAMMPS [58] are optimized to scale the computation with an increasing number of cores [59].

More specifically, MD is a computer simulation technique relying on parameterized classical potentials, commonly referred to as Force Fields (FF) [60]. The time evolution of a set of interacting particles is described by integrating Newton's equations of motion

$$\mathbf{F}_i = m_i \mathbf{a}_i \tag{2.1}$$

where $\mathbf{F}_i$ is the force acting on a particle i with mass m_i, generating an acceleration $\mathbf{a}_i$. The equations of motion can be rewritten under the form of the Hamiltonian equations:

$$\begin{cases} \dot{q} = \frac{\partial H}{\partial p} = \{q, H\} \\ \dot{p} = -\frac{\partial H}{\partial q} = \{p, H\} \end{cases} \tag{2.2}$$

with "$\{\cdot,\cdot\}$" the Poisson brackets, and H the Hamiltonian

$$H = \sum_i \frac{\mathbf{p}_i}{2m_i} + U(\mathbf{q}_i) \tag{2.3}$$

containing the kinetic and the potential energy of the system. Here, $\mathbf{q}_i$ corresponds to the generalized coordinates of the atom i and $\mathbf{p}_i$ to its conjugate momentum. The integration of the equations of motion calls for the use of efficient algorithms, such as the Verlet or "leap frog" ones [61]. The time evolution of a system of interacting particles requires *i*) a set of initial conditions of all the particles in the system (initial positions and velocities), and *ii*) the interaction potential from which the forces among all the particles are derived. The computation of the forces acting on each particle is the most time consuming part of the MD computation. An appropriate description of a given system necessitates a model that takes into account as many interactions existing in the system as possible. The result of this process is the creation of the force field. The force field is a collection of equations and associated constants designed to reproduce molecular geometries and properties of test structures (e.g., electrostatic interactions, van der Waals forces and bond stretching). Depending on the kind of system, the need to simulate a large number of atoms can be overcome by using periodic boundary conditions: the system is described by a repeating unit formed by a minimal number of atoms. This description assumes that all the atoms in the images of the repeating unit move in exactly the same way.

The main weakness of MD is the limitation to a classical description of a system, that is not able to take into account the quantum effects of the atomic structure. Another weakness is represented by the non-versatility of the force fields: they are not able to properly describe systems different than those for which they have been designed. In other words, the transferability of the force fields is nearly absent. The definition of a force field can be made by using ab initio methods, in which the transferability of the description of the interactions is guaranteed in almost all the cases.

2.3 Ab initio

The term "ab initio" is a latin term meaning "from the beginning". It refers to methods that calculate the observables of a system by relying on basic and established laws of nature, without additional assumptions or special models in the form of ad hoc parameters. The electronic structure of a system, whether it be a molecule or

Table 2.1: Scalability in the hierarchy of common ab initio methods approximating the solution of the electronic SE. The scalability is expressed with respect to the order of the number of atoms M or of the number of basis functions N.

method	number of atoms	number of basis functions
CCSDT	$O(M^8)$	$O(N^8)$
CCSD(T)	$O(M^7)$	$O(N^7)$
CCSD	$O(M^6)$	$O(N^6)$
MP2	$O(M^5)$	$O(N^5)$
HF	$O(M^3)$	$O(N^4)$
DFT	$O(M^3)$	$O(N^3)$

a crystal, is described by the quantum mechanics (QM). In this framework, one of the possible states of a system of N electrons is described by a wave function (WF) $\psi(\mathbf{r}_1, \mathbf{r}_2, \cdots, \mathbf{r}_N, t)$, depending on the time t, the general coordinates $\mathbf{r}_i$, and fulfilling the many-body Schrödinger equation (SE). This equation is the back bone of quantum physics theory as we will see in chapter 3.

The SE can be analytically solved only for a few systems with a single electron (hydrogenic atoms) while, for large systems, it is necessary to approximate the solution numerically. The simplest approach used in the hierarchy is the Hartree–Fock (HF) method, which describes the electron-electron interactions with a mean-field approach, as introduced by Hartree [62]. The electron-correlation effects are neglected in this approach; they are considered in several extensions of it, namely the post-HF and Density Functional Theory (DFT) methods. Among the most prominent examples of post-HF methods are perturbative approaches (e.g. MP2) or the coupled-cluster(CC) expansion [63]. Yet, these methods lack efficiency in terms of scalability. In this context, scalability refers to the ability of a computational technique to transpose its efficiency to a scaled-up system. In our case, a "large system" is a system that contains ~ 300 atoms. Even the simplest HF method scales generally as $O(M^3)$, with M being the number of atoms (Table 2.1). Finally it is apparent that DFT provides a better scalability than the post-HF techniques. It is worth mentioning that the Car-Parrinello approach manages to combine molecular dynamics and density-functional theory, extending and integrating the applicability of both methods [64]. The principles behind the various ab initio methods will be treated in the next chapter.

Chapter 3

Ab initio: principles and methods

As stated in the previous chapter, the investigation of the electronic structure of materials commands going beyond classical mechanics. In this chapter, we introduce the reader to some basic principles of quantum mechanics. This allows us to detail the theory providing basic approximations of the solution of the Schrödinger equation, such as the Hartree and the Hartree-Fock methods. Those are the starting point for the development of more elaborate ab initio frameworks, and historically led to the development of the Density Functional Theory.

3.1 Quantum model

The dynamic evolution of a system is described by the time dependent Schrödinger equation

$$i\hbar\frac{\partial}{\partial t}\psi(\mathbf{r},t) = \hat{H}(\mathbf{r},t)\psi(\mathbf{r},t) \tag{3.1}$$

where $\psi(\mathbf{r},t)$ is the wave function describing the system at the time t and space position $\mathbf{r}$, and $\hat{H}(\mathbf{r},t)$ is the Hamiltonian operator representing the total energy of the system. In the present work, we will study systems in which the total energy is constant; therefore, the corresponding Hamiltonian is time independent and the Schrödinger equation assumes the eigenvalue-eigenvector equation form

$$\hat{H}(\mathbf{r})\psi(\mathbf{r}) = E\psi(\mathbf{r}) \tag{3.2}$$

where E is the energy eigenvalue corresponding to the eigenfunction $\psi(\mathbf{r})$, solution of the equation. Equation 3.2 can be written as

$$\hat{H}\left|\psi\right\rangle = E\left|\psi\right\rangle \tag{3.3}$$

by using the Dirac notation [65].

As in classical mechanics, the Hamiltonian is generally written as

$$\hat{H} = \hat{T} + \hat{V}, \tag{3.4}$$

which is the sum of the kinetic ($\hat{T}$) and the potential ($\hat{V}$) operators, respectively, associated with the kinetic and the potential energy of the system. The solution of Equation 3.2 allows access to the expectation value of any physical quantity of the system such as the energy, or the probability density of the presence of a particle. Unfortunately, we are only able to obtain the exact solution of the Schrödinger equation for the case of hydrogen-like atoms, by considering the Coulombic interaction between the protons in the nucleus and the only electron bound to it, and neglecting the spin-spin coupling. This is due to the functional form of the Hamiltonian $\hat{H}$, which becomes overly complicated when we consider atoms with more than one electron or forming molecules or crystals. These cases are termed *many body problems*, and the search for the solution of the relative SE requires approximations. The general expression for the Hamiltonian of an ordinary many body atomic system is

$$\hat{H}_{tot} = \hat{T}_e + \hat{V}_{e-N} + \hat{V}_{e-e} + \hat{T}_N + \hat{V}_{N-N} \tag{3.5}$$

where:

- $\hat{T}_e$ is the kinetic energy of the electrons,
- $\hat{V}_{e-N}$ is the potential acting on the electrons due to the nuclei,
- $\hat{V}_{e-e}$ is the electron-electron interaction,
- $\hat{T}_N$ is the kinetic energy of the nuclei, and
- $\hat{V}_{N-N}$ is the nucleus-nucleus interaction.

More explicitly:

$$\hat{H}_{tot} = \underbrace{-\frac{\hbar^2}{2m_e}\nabla_i^2}_{\hat{T}_e} \underbrace{-\sum_{i,\alpha}\frac{Z_\alpha e^2}{|\mathbf{r}_i - \mathbf{R}_\alpha|}}_{\hat{V}_{e-N}} + \underbrace{\frac{1}{2}\sum_{i\neq j}\frac{e^2}{|\mathbf{r}_i - \mathbf{r}_j|}}_{\hat{V}_{e-e}} + \underbrace{\sum_{\alpha}\frac{\hbar^2}{2M_N}\nabla_\alpha^2}_{\hat{T}_N} + \underbrace{\frac{1}{2}\sum_{\alpha\neq\beta}\frac{Z_\alpha Z_\beta e^2}{|\mathbf{R}_\alpha - \mathbf{R}_\beta|}}_{\hat{V}_{N-N}}, \tag{3.6}$$

where summations run on α, β atoms, and i, j electrons. Z_α is the atomic number of the α-th ion, while e is the elementary charge.

The Born-Oppenheimer approximation [66] provides a widely used first simplification to the many body problem: since the inertia of the nuclei is far larger than

that of the electrons ($m_n \gtrsim 1836\ m_e$), we can consider that the electrons are moving in a potential created by the nuclei which are at rest in the reference frame of the laboratory. The separability of the variables allows us then to split the eigenvalues problem Equation 3.2 into two eigenvalue-eigenvector equations

$$\hat{H}_e\psi_e(\mathbf{r}) = [\hat{T}_e + \hat{V}_{e-e} + \hat{V}_{n-e}]\psi_e(\mathbf{r}) = E_e\psi_e(\mathbf{r}) \tag{3.7}$$

for the electrons, and:

$$[\hat{T}_n + \hat{V}_{n-n} + E_e]\phi(\mathbf{R}) = E\phi(\mathbf{R}) \tag{3.8}$$

for the nuclei.

The electronic Hamiltonian $\hat{H}_e$ from Equation 3.7 can be rewritten as

$$\hat{H}_e = -\frac{1}{2}\sum_{i=1}^{N}\nabla_i^2 + \sum_{i=1}^{N}\sum_{j>i}^{N}\frac{1}{r_{ij}} - \sum_{i=1}^{N}\sum_{A=1}^{M}\frac{Z_A}{r_{Ai}} \tag{3.9}$$

where atomic units have been used for simplicity. The r_{ij} and r_{Aj} terms stand for the distance between electron i and j, and the distance between atom A and electron i, respectively. N indicates here the total number of electrons, while M is the total number of atoms. The last term V_{n-e} depends on the electric charge carried by the atom, denoted by the atomic number Z_A.

We see from Equation 3.8 that solving the electronic Schrodinger equation Equation 3.7 gives us the potential energy E_e felt by the nuclei. Since the potential V_{n-n} can be seen as an "offset" that can be computed classically, and T_n can be neglected in this approximation, solving the many-body problem reduces to solving the electronic equation Equation 3.7 for any given position of the ions.

Historically, the Hartree approximation aims to solve the problem by writing the electronic Wave Function (WF) as a product of monoelectronic WFs. The interaction between electrons is replaced by an interaction of each electron with a mean potential created by all the other electrons surrounding it. The problem is then solved by using the variational principle. This approach is incomplete yet, as it does not take into account the antisymmetry of the electronic WF, a consequence of the fermionic nature of the electrons (Pauli's principle) [67, 68]. The Hartree-Fock approximation, later introduced, aimed to correct this. However, it does not take into account the correlation effects of the electrons' motion: since the spatial separation between the electrons is not accurately described, so is the Coulombic

repulsion between them [69]. When the correlation effects are small compared to the exchange effects, the Hartree-Fock approximation gives good results; otherwise, this description is not sufficient. This problem was tackled by the introduction of post-HF and DFT methods.

3.2 Hartree method

The Hartree method [70] is the simplest type of ab initio calculation of the electronic structure. It is based on a single particle picture: the assumption is to consider that electrons occupy single particle orbitals. Instead of considering an electronic WF which includes all the electrons as a whole, the idea is to consider that the electrons are all living in the middle of a mean potential, created by themselves. Each electron then contributes to this potential and interacts with the others through it. The ansatz for the many-electron WF, solution of Equation 3.15, is that it is simply a product of these single electronic WFs, or Hartree states:

$$\psi = \psi_1(\mathbf{r}_1)\psi_2(\mathbf{r}_2)...\psi_n(\mathbf{r}_n), \tag{3.10}$$

where $\mathbf{r_i}$ refers to generalized coordinates that can include spatial and also spin degrees of freedom.

From here, the determination of ψ relies on the variational principle. The variational principle states that, for any trial WF, the expectation value of the electronic Hamiltonian $\hat{H}_e$ is always higher than or equal to the electronic ground state energy ($E[\psi] \geq E_0\,[\psi_0]$), i.e., the lowest energy state. Only when the WF is the one of the true ground state, the equality is verified. In essence, the variational procedure consists of improving the quality of the initially guessed WF ψ, by minimizing the energy $E[\psi]$. This is obtained by finding the *stationary* solution of the equation

$$\left\langle \hat{H}_e - E \right\rangle_\psi = \int \Big(\langle\psi|\hat{H}_e|\psi\rangle - E\,\langle\psi|\psi\rangle \Big) = 0 \tag{3.11}$$

which is the solution of the Schrödinger equation for the system of electrons (Equation 3.7). Indeed, if we take the functional derivative

$$\delta \left\langle \hat{H}_e - E \right\rangle_\psi = \int d^3r \delta\psi^*(r) \left[\hat{H}_e\psi(\mathbf{r}) - E\psi(\mathbf{r}) \right] \tag{3.12}$$

we see that the variation is equal to zero when $\psi(\mathbf{r})$ is the solution of the SE. When considering a system of distinguishable electrons, the general electronic Hamiltonian has the form of a sum of single particle energy terms of the particles i plus a pair

interaction term:

$$\hat{H}_e = \underbrace{\sum_i \frac{\mathbf{p}_i^2}{2m} + V_s(\mathbf{r}_i)}_{\hat{H}_i} + \frac{1}{2}\sum_{i\neq j} V_{ij} \tag{3.13}$$

with V_s being the single particle potential and V_{ij} the pair interaction potential between particles i and j.

If we assume that the eigenstates of the total Hamiltonian can be written as a product of single particle eigenstates as stated in Equation 3.10, the quantity to be stationary is now

$$\begin{aligned}\sum_i \int d^3\mathbf{r}_i \psi_i^*(\mathbf{r}_i)\hat{H}_i\psi_i(\mathbf{r}_i) + \frac{1}{2}\sum_{i\neq j}\int d^3\mathbf{r}_i d^3\mathbf{r}_j \psi_i^*(\mathbf{r}_i)\psi_j^*(\mathbf{r}_j)V_{ij}\psi_i(\mathbf{r}_i)\psi_j(\mathbf{r}_j) \\ - E\prod_i \int d^3\mathbf{r}_i \psi_i^*(\mathbf{r}_i)\psi_i(\mathbf{r}_i),\end{aligned} \tag{3.14}$$

and then the functional derivative with respect to $\psi_m^*(\mathbf{r}_m)$ for the m-th particle gives:

$$\int d^3\mathbf{r}_m \left(\hat{H}_m\psi_m(\mathbf{r}_m) + \sum_{i\neq m}\int d^3\mathbf{r}_i \psi_i^*(\mathbf{r}_i)V_{im}\psi_i(\mathbf{r}_i)\psi_m(\mathbf{r}_m) - E\psi_m(\mathbf{r}_m)\right)\delta\psi_m^*(\mathbf{r}_m) = 0, \tag{3.15}$$

the factor ½ disappearing due to the equality of the second term when $m = i$ and $m = j$. This means that each single particle state must satisfy the Hartree equation:

$$\hat{H}_m\psi_m(\mathbf{r}_m) + \left(\sum_{i\neq m}\int d^3\mathbf{r}_i \psi_i^*(\mathbf{r}_i)V_{im}\psi_i(\mathbf{r}_i)\right)\psi_m(\mathbf{r}_m) = E\psi_m(\mathbf{r}_m). \tag{3.16}$$

We now see in this first attempt that solving the N-particles problem leads to the reformulation into a set of single-particle equations. These equations are connected by the interaction between the particles contained in the Hartree potential

$$V_H(\mathbf{r}_m) = \int d^3\mathbf{r}_i \sum_{i\neq m} |\psi_i(\mathbf{r}_i)|^2 V_{int}(|\mathbf{r}_i - \mathbf{r}_m|). \tag{3.17}$$

through which each m-th particle interacts with the probability density of all the other particles i, with a probability

$$\mathcal{P}^m(\mathbf{r}) = \sum_{i\neq m} |\psi_i(\mathbf{r}_i)|^2. \tag{3.18}$$

The potential for a given particle m then depends on the states of all the other

$N-1$ particles; for this reason, it is called a *self consistent* potential. First, an initial guess is made for the potential, then the eigenvalue equation is solved, the density is calculated from the obtained wave function, and a new potential is found. Such steps are repeated until the wave function obtained in subsequent steps does not change significantly: in this case, we say that *self-consistency* is reached. This set of equations constitutes what we call the *self consistent field* (SCF) equations.

Let's summarize the procedure here:

1. guess a set of single particle states ψ_i,
2. compute the Hartree potential V_H for each particle by using the states ψ_i,
3. solve the single particle equations by using the V_H obtained the step before, and
4. if the states obtained at step (3) are different than the states used as a guess in step (1), use them as a new guess and repeat the procedure.

Of course, many technicalities are applied in the process. An important point is that the new guess of the states at the beginning of one cycle is a mix of the old guess and the new solutions [71, 72, 73]. This mix can be obtained by using various distributions, with the goal to reduce possible numerical oscillations. Although necessary in most cases, this procedure can be quite resource demanding.

The SCF procedure is a basic scheme that is used in other more sophisticated methods. However, as we are about to see in the next section, the Hartree method comes with a serious drawback. By neglecting the spinorial nature (i.e., Pauli principle) of the electronic WF, it underestimates the value of the energy of a Fermionic system.

3.3 Hartree-Fock

The Hartree-Fock (HF) method follows the Hartree one, and takes into consideration the antisymmetry of the Fermionic states while solving the many-body Hamiltonian [74, 75, 76]. An orbital is a wave description of the size, shape, and orientation of the region in space that an electron can occupy. The Pauli principle states that the quantum state of an electronic system is uniquely defined. This means that for two electrons to occupy the same orbital, i.e., having the same quantum numbers, they have to possess different spin. This is equivalent writing that the total WF of a Fermionic system is antisymmetric with respect to the exchange of any pair of

electrons:

$$\psi(\mathbf{x}_1, \mathbf{x}_2, ..., \mathbf{x}_i, ..., \mathbf{x}_j, ..., \mathbf{x}_N) = (-1)^n \psi(\mathbf{x}_1, \mathbf{x}_2, ..., \mathbf{x}_j, ..., \mathbf{x}_i, ..., \mathbf{x}_N) \tag{3.19}$$

where the index n runs over all $N!$ permutations of the N single-particle states, and the $\mathbf{x}_i$ variable incorporates the spatial coordinates and spin for each particle, that is $\mathbf{x}_i = (\mathbf{r}_i, \sigma_i)$. In the HF scheme, the wave function is approximated with single electron WFs describing non interacting particles. Here, each single electron wave function is the product of a spatial wave function of the electron position $\mathbf{r}$ multiplied by a function of the spin component S_z, thus obtaining the spin-orbital $|\psi_i(\mathbf{x}_i)\rangle = |\phi(\mathbf{r_i})\rangle\,|\sigma_i\rangle$ [65]. The wave function is then given by a Slater determinant of N spin-orbitals:

$$\psi^{HF} = \psi(\mathbf{x}_1, \mathbf{x}_2, ..., \mathbf{x}_N) \;=\; \frac{1}{\sqrt{N!}} \begin{vmatrix} \psi_1(\mathbf{x}_1) & \psi_2(\mathbf{x}_1) & \dots & \psi_N(\mathbf{x}_1) \\ \psi_1(\mathbf{x}_2) & \psi_2(\mathbf{x}_2) & \dots & \psi_N(\mathbf{x}_2) \\ \vdots & \vdots & & \vdots \\ \psi_1(\mathbf{x}_N) & \psi_2(\mathbf{x}_N) & \dots & \psi_N(\mathbf{x}_N) \end{vmatrix} \tag{3.20}$$

where the factor $1/\sqrt{N!}$ ensures the normalization of the many body wave function. The change of sign of the many-body wave function with the exchange of two electrons corresponds to the switch of two rows in the determinant. The expectation value of the energy is

$$\left\langle \psi^{HF} \middle| \hat{H} \middle| \psi^{HF} \right\rangle = \sum_i \left\langle \psi^{HF} \middle| \hat{h}_i \middle| \psi^{HF} \right\rangle + \sum_{ij} \frac{1}{2} \left\langle \psi^{HF} \middle| \hat{V}_{e-e} \middle| \psi^{HF} \right\rangle \tag{3.21}$$

where, again, we have separated the monoelectronic part of the Hamiltonian, $\hat{h}_i = \hat{T}_e + \hat{V}_{n-e}$, from the inter-electron interaction $\hat{V}_{e-e}$. The potential V_{e-e} is the result of the Coulombic interaction and depends on the distance among the particles. The use of the variational principle gives us again the set of orbitals that minimize the energy

$$E = \min_{\phi} \left\langle \psi^{HF} \middle| \hat{H} \middle| \psi^{HF} \right\rangle = \min_{\phi} \left\langle \psi^{HF} \middle| \hat{h}_i + \hat{V}_{e-e} \middle| \psi^{HF} \right\rangle. \tag{3.22}$$

The Coulomb interaction yields two contributions:

$$\left\langle \psi^{HF} \middle| \hat{V}_{e-e} \middle| \psi^{HF} \right\rangle = \left\langle \psi^{HF} \middle| \frac{1}{|\mathbf{r}_j - \mathbf{r}_i|} \middle| \psi^{HF} \right\rangle = V_H[\psi] + E_x[\psi]; \tag{3.23}$$

the first term is the Hartree term, which represents the electrostatic energy of the charge density while $E_x[\psi]$ is the exchange integral, also called *Fock term*. This is a

contribution to the energy that arises from Pauli's exclusion principle and it is the result of the integration over the occupied orbitals:

$$E_x[\phi_i] = -\frac{1}{2}\sum_{\sigma}\sum_{i,j}\int d^3r \int d^3r' \frac{\phi^*_{i\sigma}(\mathbf{r})\phi^*_j\sigma(\mathbf{r}')\phi^*_{i\sigma}(\mathbf{r}')\phi^*_{j\sigma}(\mathbf{r})}{|\mathbf{r}-\mathbf{r}'|}. \tag{3.24}$$

This contribution is orbital dependent. For a system of one electron, the Fock term is the opposite of the Hartree potential; this is expected, as there is no interaction V_{ee} between electrons. As the number of electrons grows, the difference between the Hartree energy and the exact one increases. For first row elements and noble gases, the HF energy differs from the exact one by 20-40 mHa/electron [77]. This difference comes from the fact that the correlation between the electrons is not taken into account. Despite the fact that the HF equations allow us to find a self consistent set of orbitals in a relatively easy way, the problem that arises now is the difficulty to quantify this correlation. Several post-HF methods incorporate the correlation effect [78, 79]; however, perturbative approaches can be computationally very expensive after the 2^{nd} order, and lack scalability. In the next section, we will see how the Density Functional Theory solves this problem, by defining a systematic approach for a system of interacting particles.

3.4 Density functional theory

Density Functional Theory was developed while aiming to solve the many-body problem. It essentially consists of a mapping between a system of interacting electrons into a system of non-interacting ones. Nowadays, it is one of the most widely used and reliable first principles ab initio techniques in materials science field. The description of an ensemble of N electrons by using an electronic wave function of N electrons requires consideration of $3N$ spatial and N spin coordinates. The calculation of a wave function with $3N + N$ degrees of freedom implies a relatively huge computational load, and calls for the need to develop new methods that attain the same results while using a smaller number of variables. In 1964, Pierre Hoenberg and Walter Kohn introduced the core theorems of the DFT [80]. They proved that, given a system in a non-degenerate ground state, the system energy, the wave function and all the other electronic properties are uniquely determined by the probability density of the electronic ground state, which is a function of only three spatial coordinates. The electron density $\rho(\mathbf{r})$, rather than the many-electron wave function ψ, becomes the central quantity to calculate, in order to access any observable of the system. The DFT allows us to see the problem from another point

of view, by focusing on the density of electrons $\rho(\mathbf{r})$, which becomes the fundamental variable, instead of the total many-body WF [77]. The standard DFT procedure to obtain the ground state electronic density $\rho_0(\mathbf{r})$ is summarized in Figure 3.1.

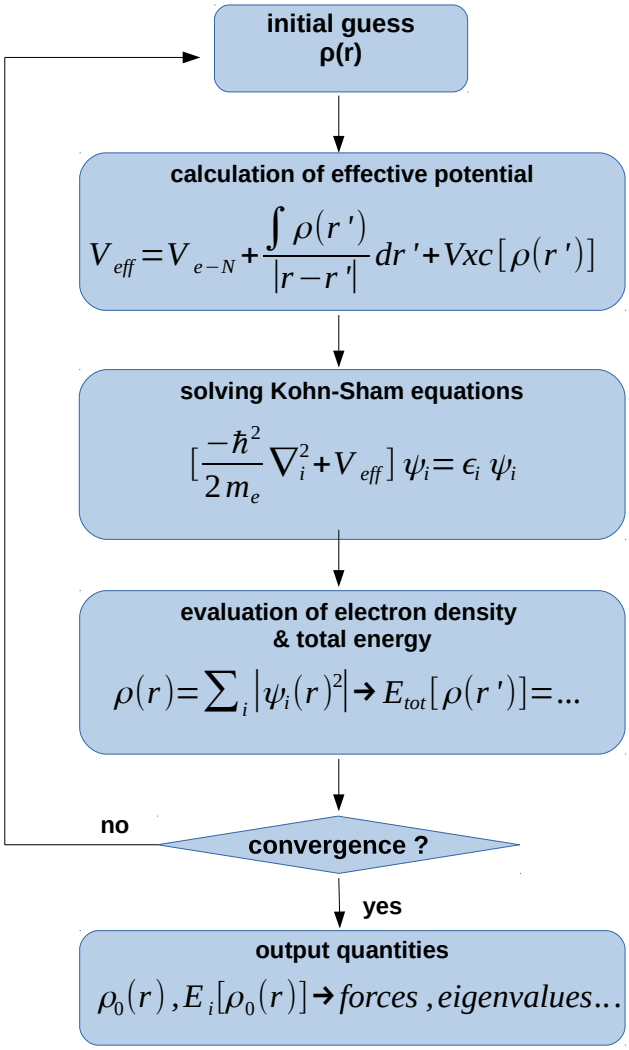

Figure 3.1: Scheme of the iterative procedure for the determination of the density ρ_0 and the physical observables.

3.4.1 The Kohn-Sham Equations

The Hohenberg and Kohn theorem results can be implemented in different ways. The form created by Khon and Sham [81] casts the problem in a one-body formalism and expresses the density $\rho(\mathbf{r})$ in terms of single-particle orbitals $\psi_i(\mathbf{r})$; the problem is then reduced to a set of coupled differential equations that can be solved iteratively. The kinetic energy term in Equation 3.7 can be written as $\hat{T}_e = \hat{T}_s + \hat{T}_c$,

where $\hat{T}_s$ is the kinetic energy of a non interacting electronic system [80] and $\hat{T}_c$ $=\hat{T}_e$-$\hat{T}_s$ represents all the correlation effects not included in the non-interacting system. Likewise, $\hat{U} = \hat{U}_H + \hat{U}_c$, with U_H being the mean-field Hartree potential of the electrostatic Coulomb interaction. The main idea of the DFT is to consider that a system of interacting electrons is equivalent to a system of non-interacting electrons "seeing" a mean effective potential which is a function of the electron density. This is condensed by the results of the two Hoenberg and Kohn theorems [80, 77]:

- the ground state properties of a many-electron system are uniquely determined by an electron density depending only on 3 spatial coordinates; this allows us to move the study from a $3N$-dimension to a 3-dimension problem where we aim to find the functional of the density;

- the form of the energy functional of the whole system is minimal for the ground state electron density $\rho_0(\mathbf{r})$.

The mean value of a general observable $\hat{O}$ is then a functional of the ground-state electron density:

$$\langle \hat{O}[\rho_0] \rangle = \langle \Psi[\rho_0] | \hat{O} | \Psi[\rho_0] \rangle \tag{3.25}$$

which, in the case of the Hamiltonian, is

$$E[\rho_0] = \langle \Psi[\rho_0] | \hat{T} + \hat{V}_{ext} + \hat{V_{XC}} | \Psi[\rho_0] \rangle. \tag{3.26}$$

The external potential contribution $\langle \Psi[\rho_0] | \hat{V}_{ext} | \Psi[\rho_0] \rangle$, independent of the system, can be re-written as a functional of ρ_0

$$V_{ext}[\rho_0] = \int V_{ext}[\mathbf{r}] \rho_0[\mathbf{r}] d^3\mathbf{r} \tag{3.27}$$

while the kinetic and exchange-correlation terms are universal, i.e., they have the same expression whatever the external potential is. The system energy can then be expressed in the form

$$E[\rho(\mathbf{r})] = F_U + \int V_{ext}[\mathbf{r}] \rho[\mathbf{r}] d^3\mathbf{r} \tag{3.28}$$

with F_U being the *universal functional*. Finally, according with the second theorem, the energy of the ground state is written as

$$E_0 = E(\rho_0(\mathbf{r})) = \min_{\rho} E(\rho(\mathbf{r})). \tag{3.29}$$

The solution of this equation by Kohn and Sham [81] leads to a system of coupled single particle equations:

$$\begin{cases} \hat{H}^{KS}\psi_i &= \varepsilon_i\psi_i \\ V_{eff}(\mathbf{r}) &= V_{ext}(\mathbf{r}) + V_H(\mathbf{r}) + V_{XC}(\mathbf{r}) \\ \rho(\mathbf{r}) &= \sum_i n_i|\psi_i|^2 \end{cases} \tag{3.30}$$

where we have *i*) the Kohn-Sham states ψ_i, *ii*) the energies of Kohn-Sham one electron orbitals, and *iii*) the Kohn-Sham monoelectronic operator $\hat{H}_{KS}$

$$\hat{H}_{KS} = -\frac{1}{2}\nabla_i^2 + V_{ext}(\mathbf{r}) + V_H(\mathbf{r}) + V_{XC}(\mathbf{r}). \tag{3.31}$$

Looking at the form of $\hat{H}_{KS}$, we can see that the right hand side potential terms can be seen as an effective potential V_{eff} depending on the position. In what follows, we will refer to this effective potential as the Kohn-Sham (KS) potential V_{KS}. We finally stress again that the exchange and correlation term V_{XC} is unknown, and must be approximated. The choice of the approximation is one of the main difficulties in a material simulation based on the DFT. Energy functionals can be categorized into non-empirical (formulated only by satisfying some physical rules), or empirical ones, the latter designed by adding "by hand" some parameters fitted to known results obtained for properties of some atoms or molecules. As is often the case in simulations, there is a trade-off to make, between choosing a versatile, widely applicable non-empirical functional, or an empirical functional designed for computing the properties of a particular type of material with a better precision, but that will fail when used outside of its range of application. The ratio of computation time *vs.* precision is also an important factor to consider. A useful categorization of functionals has been proposed by Perdew [82], and is known as "Jacob's Ladder" (Figure 3.2). In what follows, we detail the important aspects of the implementation of a DFT simulation, and discuss the specificities of some of the most common used exchange-correlation functionals.

3.4.2 Practical implementation of the DFT equations

In subsection 3.4.1 we saw that the complex problem represented by Equation 3.7 has been reformed into the equivalent set of coupled differential equations 3.30. The

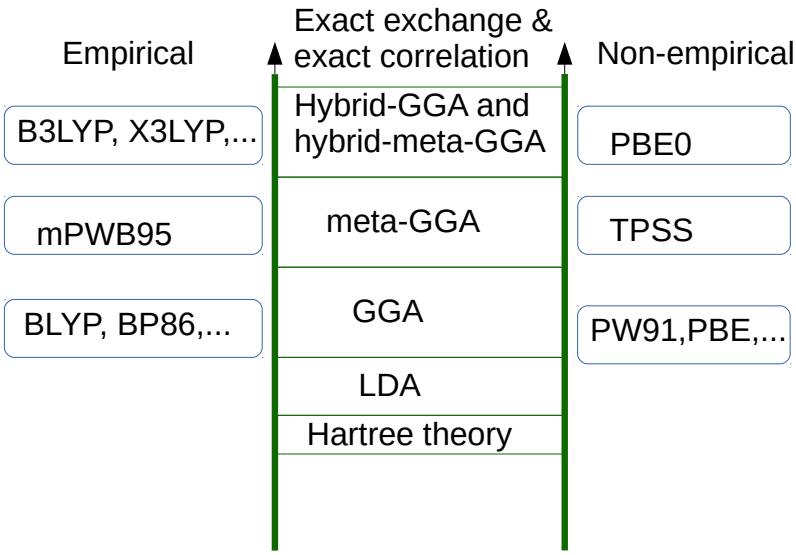

Figure 3.2: Schematic diagram of "Jacob's ladder" detailing the hierarchy of exchange-correlation functionals proposed by J. P. Perdew. Adapted from [82].

formalism does not provide an explicit analytic form and various approximations need to be implemented to find a numerical solution of Equations 3.30.

Choice of the basis set. The unknown Kohn orbitals $\phi(\mathbf{r})$ can be expanded into a set of known functions and the KS equations can be written in terms of the expansion coefficients. This possible set of functions is conventionally divided into two categories: plane-wave and localised basis sets.

In a plane-wave basis set, the density is expressed in terms of periodic and oscillatory wave functions, forming a complete representation of the Hilbert space. To obtain the exact WF, an infinite number of basis functions would be necessary for the basis to be complete. Of course, this is not computationally affordable, and so the precision of the approximated WF is determined by truncating the basis set according to appropriate cutoffs. This is the most suitable choice when dealing with periodic systems [83].

In a localized basis set, the electron density is described in terms of functions centered on the atomic positions, like Gaussian [84] or Slater-type orbitals [85]. This is the preferred choice when electrons are localized around ions, like in the case of metal oxides and molecules, where the WF exponentially decays to zero at large distances from the nuclei.

Exchange-Correlation Functional and its approximations. As we explained in section 3.4, the exact form of the exchange-correlation potential $V_{XC}(\mathbf{r}) = \frac{\partial E_{XC}(\mathbf{r})}{\partial \rho(\mathbf{r})}$ is not known and so approximations have to be made. The simplest forms of these approximations are introduced below:

- The Local Density Approximation (LDA) is based on the hypothesis that the exchange and correlation terms depend only on the local value of the electronic density $\rho(\mathbf{r})$. Its expression is:

$$E_{XC}^{LDA}(\rho(\mathbf{r})) = \int \rho(\mathbf{r}) \epsilon_{XC}\left(\rho(\mathbf{r})\right) d\mathbf{r} \tag{3.32}$$

  where $\epsilon_{XC}(\rho(\mathbf{r}))$ is the exchange and correlation energy per electron, of a homogeneous electron gas with density $\rho(\mathbf{r})$. In this approach, the electronic density is assumed to be homogeneous; consequently, this is a reliable approximation for isotropic systems and when the electronic density varies weakly. The LDA performs rather poorly in the study of molecules in which the electron density can be highly inhomogeneous.

- The Generalized Gradient Approximation (GGA) consists in taking into account the local variations of the electronic density by including its gradient $\nabla\rho(\mathbf{r})$ in the description. The exchange and correlation term is then written as

$$E_{XC}^{GGA}(\rho(\mathbf{r})) = \int \rho(\mathbf{r}) \epsilon_{XC}\left(\rho(\mathbf{r}), \nabla\rho(\mathbf{r})\right). \tag{3.33}$$

  This is the preferred approximation for systems where the electrons are loosely localized.

Van der Waals interactions. Van der Waals (vdW) interactions are non-local and long-range interactions by nature. The long range correlations responsible for these interactions can be described in several ways:

- By using a self-consistent non-local functional that can be included explicitly in the KS equations, thus providing a vdW correction directly from the electron density; this method is generally computationally expensive [86].

- By adding an empirical a posteriori correction to the solution of the KS equations. In this category there fall the DFT-D methods, namely DFT-D2 [87], DFT-D3[88] and DFT-D3(BJ) [89]. In these cases, pair-wise terms, and 3-body corrections like in DFT-D3 and DFT-D3(BJ), are added to the DFT energy. Since they are independent of the electronic density, these methods

are called *non-self consistent*. This represents a relatively light computational method when compared to a self consistent one, but decouples completely the vdW description from the electron density. We can here include the maximally localized Wannier functions (MLWFs) methods. In these, the pair-wise terms contain the contributions of pairs of MLWFs instead of pairs of atoms. The vdW-WF2 [90] and vdW-QHO-WF [91] were both used in this study in the benchmarking procedure (section 4.8).

- Meta Generalized Gradient Approximation (meta-GGA): The meta-GGA type of functionals offer a flexible choice of semi-local forms. The exchange-correlation energy functionals depend not only on the density ρ and its gradient, but also on its second order derivative through the kinetic energy density:

$$\tau(r) = \sum_i \frac{1}{2} |\nabla^2 \psi_i(\boldsymbol{r})|^2 \tag{3.34}$$

  where the sum runs on the occupied orbitals. Largely used meta-GGA functionals are tHCTH [92, 93], TPSS [94] or VSXC [95].

Pseudopotentials. Because of the fact that the nuclei are point-like (positive) charges, the variation of the potential around them is steep as the density of charges varies rapidly. This behaviour can become an issue when we need to find a numerical solution of the problem. Indeed, to describe a rapidly varying function, a huge number of basis functions is needed. When we are not interested in the behaviour of the density close to the nuclei, a solution to reduce the number of basis functions is to use pseudopotentials. The pseudopotential method is based on an ansatz which separates the total wave function into an oscillatory part and a smooth part, which is called *pseudo wave function*. Given the fact that the chemical bonding is mainly created by valence electrons, while the inner electronic structure is kept unchanged, it is useful to replace the strong, true potential of the ions by a weaker potential, that approaches the shape of the true potential for distances larger than the core radius. The outer valence electrons now feel a flatter, softer mean potential, and can be described with a smaller number of WFs.

Throughout this thesis, we use two different types of pseudopotentials, the norm-conserving [96] and projected augmented wave (PAW) [97] pseudopotentials, as provided by the ABINIT package [98].

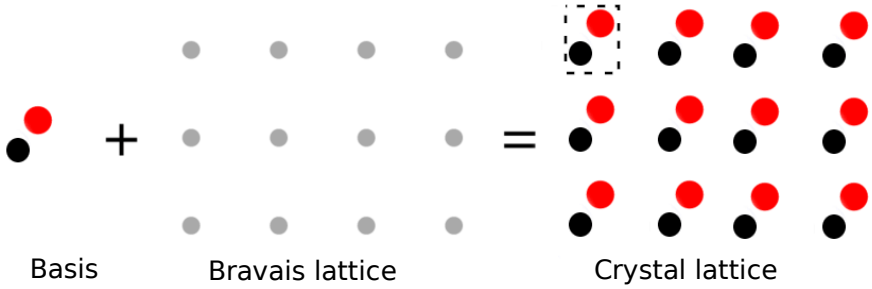

Figure 3.3: The crystal structure is composed of a basis associated to a space lattice.

3.5 Crystal structure and Brillouin zone

The quantum theory of crystals was introduced in 1928 by the physicist Felix Bloch [99, 67]. The fundamental distinction between amorphous solids, like glass and crystals, is that crystals are formed by the repetition of groups of atoms. Such a group is called a *basis*, while a set of mathematical points to which the base is attached is called *lattice* [67]. The lattice is described by means of vectors, say $\mathbf{a}_1$, $\mathbf{a}_2$, $\mathbf{a}_3$. These vectors are such that the crystal "looks" the same in $\mathbf{r}$ and in every point $\mathbf{r}'$ that is translated from $\mathbf{r}$ by a vector $\mathbf{T}$:

$$\mathbf{r}' = \mathbf{r} + \mathbf{T} \tag{3.35}$$

with

$$\mathbf{T} = u_1\mathbf{a}_1 + u_2\mathbf{a}_2 + u_3\mathbf{a}_3, \tag{3.36}$$

and u_1,u_2,u_3 being integer coefficients. When the primitive translation vectors $\mathbf{a}_i$ describe the smallest building block of the crystal structure, the enclosed volume is called the *primitive cell*. One possible choice of primitive cell is the Wigner-Seitz cell [100], as illustrated in Figure 3.4.

There are only 14 distinct three-dimensional configurations of points used to describe the orderly arrangement of atoms in a 3-dimensional crystal. They are called Bravais lattices. These lattices are classified into groups according to their type of cell. The group corresponding to our TMD structures is the hexagonal one (Figure 3.5).

The periodicity of a crystal that we detailed in the beginning of this section creates an ideal situation for the application of the Fourier transform. According to the Fourier theorem, any periodic function that is sufficiently continuous can be decomposed into a series of sinusoidal components, each having a specific amplitude

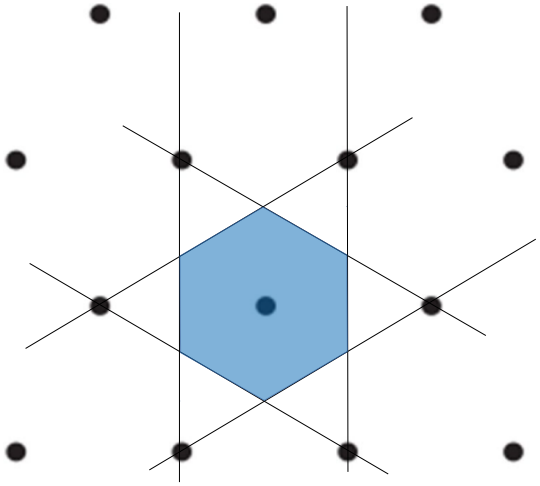

Figure 3.4: Wigner-Seitz unit cell for the case of a 2D hexagonal lattice. The construction is made in 3 steps. Step 1: bisecting lines are drawn to the segments connecting the origin with the neighboring points. Step 2: these lines shape a polygon - the Wigner-Seitz unit cell. Step 3: the Wigner-Seitz unit cell is shown in blue together with lines bisecting segments to more distant lattice points.

and phase coefficient. Since a crystal is invariant under a translation of the form of $\mathbf{T}$, consequently, any physical property of the system is invariant under such translation.

Following the reasoning in Ref. [67] as an example, we consider the function ρ describing the electron density, such as $\rho(\mathbf{r}) = \rho(\mathbf{r} + \mathbf{T})$. In one dimension, the expansion of ρ in a Fourier series gives

$$\rho(x) = \rho_0 + \sum_{p>0} \left[C_p cos(\frac{2\pi px}{T}) + S_p sin(\frac{2\pi px}{T}) \right], \tag{3.37}$$

where T is the periodicity, p belongs to $\mathbb{Z}^+$, and C_p and S_p are real constants named *Fourier coefficients*. The condition on the periodicity $\rho(x+T) = \rho(x)$ implies that

$$\begin{aligned} &\rho_0 + \sum_{p>0} \left[C_p \cos\left(\frac{2\pi px}{T} + 2\frac{\pi}{T}\right) + S_p \sin\left(\frac{2\pi px}{T} + 2\frac{\pi}{T}\right) \right] \\ &= \rho_0 + \sum_{p>0} \left[C_p \cos\left(\frac{2\pi px}{T}\right) + S_p \sin\left(\frac{2\pi px}{T}\right) \right]. \end{aligned} \tag{3.38}$$

Bravais lattice	Parameters	Simple (P)	Volume centered (I)	Base centered (C)	Face centered (F)
Triclinic	$a_1 \neq a_2 \neq a_3$ $\alpha_{12} \neq \alpha_{23} \neq \alpha_{31}$	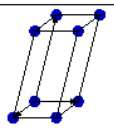			
Monoclinic	$a_1 \neq a_2 \neq a_3$ $\alpha_{23} = \alpha_{31} = 90°$ $\alpha_{12} \neq 90°$	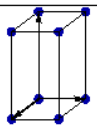	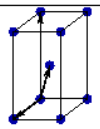		
Orthorhombic	$a_1 \neq a_2 \neq a_3$ $\alpha_{12} = \alpha_{23} = \alpha_{31} = 90°$	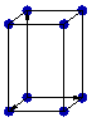	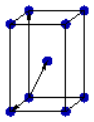	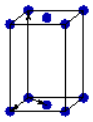	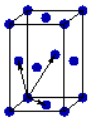
Tetragonal	$a_1 = a_2 \neq a_3$ $\alpha_{12} = \alpha_{23} = \alpha_{31} = 90°$	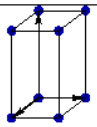	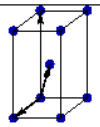		
Trigonal	$a_1 = a_2 = a_3$ $\alpha_{12} = \alpha_{23} = \alpha_{31} < 120°$	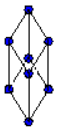			
Cubic	$a_1 = a_2 = a_3$ $\alpha_{12} = \alpha_{23} = \alpha_{31} = 90°$		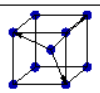		
Hexagonal	$a_1 = a_2 \neq a_3$ $\alpha_{12} = 120°$ $\alpha_{23} = \alpha_{31} = 90°$	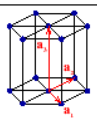			

Figure 3.5: The parameters a_i correspond to the lattice parameters, while the a_{ij} correspond to the angle between $\mathbf{a}_i$ and $\mathbf{a}_j$ vectors.

Hence, Equation 3.37 can be rewritten as a series of complex exponentials

$$\rho(x) = \sum_p \rho_p e^{\frac{i2\pi px}{a}} \tag{3.39}$$

where p belongs to $\mathbb{Z}$, and the ρ_p coefficients are complex numbers. Considering the fact that the function ρ must be real as it refers to an observable (i.e., the density) [67], the extension in 3 dimensions gives:

$$\rho(\mathbf{r}) = \sum_{\mathbf{p}} \rho_{\mathbf{p}} e^{\frac{i2\pi \mathbf{p}\cdot\mathbf{r}}{a}} \tag{3.40}$$

with a suitable choice of the $\mathbf{p}$ vectors such that Equation 3.40 is invariant under $\mathbf{T}$. How are these vectors $\mathbf{p}$ connected to the lattice introduced in Equation 3.35? If the vectors $\mathbf{a}_i$ introduced in Equation 3.35 are the edges of each identical 3-D unit cell, with volume $L \times L \times L = L^3$ (for simplicity), the position $\mathbf{r}$ of an atom

M can be labeled by using the set of unit cell vectors:

$$\mathbf{r} = u_1\mathbf{a}_1 + u_2\mathbf{a}_2 + u_3\mathbf{a}_3, \tag{3.41}$$

where now the values of the u_i parameters are integers belonging to $[-\frac{L}{2}; \frac{L}{2}]$ because of the periodic boundary conditions. The latter require that the phase of each allowed plane wave is periodic in the edge of the crystal, i.e., for all $\mathbf{p}$,

$$e^{iL\mathbf{p}\cdot\mathbf{a}_1} = e^{iL\mathbf{p}\cdot\mathbf{a}_2} = e^{iL\mathbf{p}\cdot\mathbf{a}_3} = 1. \tag{3.42}$$

We then define a new set of vectors $\mathbf{b}_i$ in this way:

$$\begin{aligned}
\mathbf{b}_1 &= 2\pi\frac{\mathbf{a}_2\times\mathbf{a}_3}{|\mathbf{a}_1\cdot(\mathbf{a}_2\times\mathbf{a}_3)|} \\
\mathbf{b}_2 &= 2\pi\frac{\mathbf{a}_3\times\mathbf{a}_1}{|\mathbf{a}_1\cdot(\mathbf{a}_2\times\mathbf{a}_3)|} \\
\mathbf{b}_3 &= 2\pi\frac{\mathbf{a}_1\times\mathbf{a}_2}{|\mathbf{a}_1\cdot(\mathbf{a}_2\times\mathbf{a}_3)|}
\end{aligned} \tag{3.43}$$

where $|\mathbf{a}_1 \cdot (\mathbf{a}_2 \times \mathbf{a}_3)|$ is the unit cell volume, here equal to L^3. This set of new vectors defines a basis in the reciprocal space, and the reciprocal lattice is defined as:

$$\mathbf{q} = u_1\mathbf{b}_1 + u_2\mathbf{b}_2 + u_3\mathbf{b}_3. \tag{3.44}$$

If the $\mathbf{a}_i$ vectors are primitive vectors of the crystal lattice, then the $\mathbf{b}_i$ vectors are the primitive vectors of the corresponding reciprocal lattice. Both the real and the reciprocal space are connected by the Fourier transform.

We showed in Equation 3.44 that the $\mathbf{q}$ vectors describe the primitive cell of the reciprocal lattice; as a consequence, the electron density at this position sees a translational invariance: the $\mathbf{p}$ and $\mathbf{q}$ vectors are therefore equivalent. This theoretical consideration can be verified experimentally: as a matter of fact, the X-ray diffraction pattern of a crystal represents the reciprocal lattice of the crystal itself [67].

The electronic, vibrational and magnetic properties that occur in a crystal have the same symmetry of the crystal. At the beginning of this section, we discussed the importance of defining the primitive cell of a crystal, since it contains all the properties of the structure under study. The Brillouin zone (BZ) is defined as the primitive cell of the reciprocal space: in this respect, it corresponds to the primitive

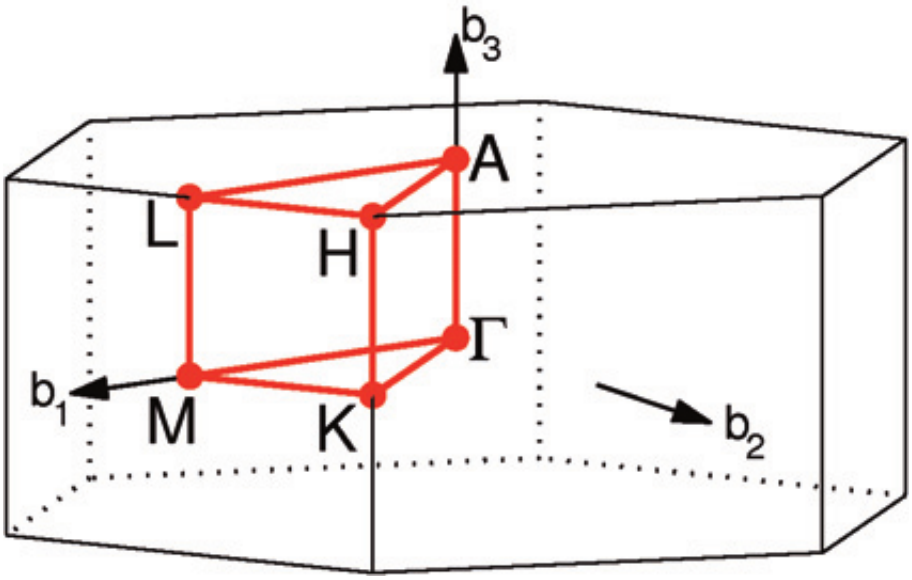

Figure 3.6: Brillouin zone of the hexagonal lattice: the red lines join the high-symmetry points (Γ, A, M...); the $\mathbf{b}_i$ labels indicate the reciprocal vectors.

cell of the direct lattice. For this reason, the study of the crystalline system can be restricted to the study of the BZ. This simplification is a consequence of the form of the wave function within a periodic potential. The Bloch theorem [67] states that, in the presence of a periodic potential, the electronic wave function in a crystal can be written as

$$\Psi_{\mathbf{k}}(\mathbf{r}) = u_{\mathbf{k}}(\mathbf{r})e^{i\mathbf{k}\cdot\mathbf{r}} \tag{3.45}$$

where the function $u_{\mathbf{k}}$ has the periodicity of the crystal [67]. Equation 3.45 implies that, if a vector $\mathbf{k}'$ falls outside the first Brillouin zone, it can be remapped into it as $\mathbf{k} = \mathbf{k}' + \mathbf{G}$, with $\mathbf{G}$ being a reciprocal lattice vector, and where $\mathbf{k}$ falls inside the BZ. The geometry of our interest has the symmetries of the hexagonal Bravais lattice; the corresponding Brillouin zone is represented in Figure 3.6 where the high symmetry points are also reported.

3.5.1 Parallelization of the computations

We have seen that the DFT is a technique that allows us to solve the Schrödinger equation at a reduced computational cost. However, numerical modeling of systems with hundreds of atoms, involving surface reconstruction [101, 102], and/or vdW interactions, which is our case, can be too long to be performed on a desktop workstation. The parallelization of ab initio software is indeed necessary.

In plane-wave based ab initio codes, most of the computational cost is taken

by eigensolvers, used for iterative diagonalization of the Hamiltonian matrix, and *Fast Fourier Transform* (FFT) libraries, that allows for switching from the real to reciprocal space [103, 104]. Efficient parallelization during this steps of the procedure is then needed. When structuring a parallel code, the goal is to avoid computational bottlenecks, i.e., situations in which the flow of the computation is slowed down at a single or several particular steps. As the size of the system increases, the impact of the bottlenecks becomes more and more significant. The way to solve this problem is to partition the data over the different computing cores. In ABINIT, the WF of the system $\psi_{n,\mathbf{k}}$ is Fourier-expanded as

$$\psi_{n,\mathbf{k}} = \sum_{\mathbf{G}} c_{n,\mathbf{k}}(\mathbf{G}) e^{i(\mathbf{k}+\mathbf{G})\cdot\mathbf{r}}, \tag{3.46}$$

and during the SCF loop the data partitioning is done with respect to the different $\mathbf{k}$-points, the blocks of bands n, and the spatial partitioning in the Fourier space of plane-wave coefficients $c_{n,\mathbf{k}}$ [105].

Chapter 4

Methodology

In order to perform this study, we used a set of descriptors and theoretical frameworks that allowed us to individuate the subtle interplay of the electronic and the dynamic features of the system, and hence, to characterize the frictional response at the nanoscale.

4.1 Electron density analysis

The electron density is the central quantity determining all the properties of the system. It measures the probability of finding an electron at a specific point in space. If Ψ is the wave function solution of the Schrödinger equation, the charge density ρ is defined as $|\Psi|^2$ over the whole space.

Electron Localisation Function. The Electron Localisation Function (ELF) [106] is a dimensionless measure of how localized the electronic density is:

$$ELF(\boldsymbol{r}) = \frac{1}{\left(1 + \frac{D(\boldsymbol{r})}{D^0(\boldsymbol{r})}\right)} \tag{4.1}$$

and it can assume values between 0 and 1. The quantity $D(\boldsymbol{r})$ represents the electron localization

$$D(\boldsymbol{r}) = \tau(\boldsymbol{r}) - \frac{1}{8}\frac{|\nabla\rho(\boldsymbol{r})|^2}{\rho(\boldsymbol{r})} \tag{4.2}$$

and depends on the electron charge density $\rho(\mathbf{r})$. The ratio in Equation 4.1 is made with respect to $D^0(\boldsymbol{r})$ that refers to the electron localization of the homogeneous electron gas. Consequently, a value of $ELF = 1/2$ corresponds to the one of the electron gas. A value of $ELF = 1$ corresponds to a perfect localization. In

Equation 4.2, τ refers to the kinetic energy density

$$\tau(\boldsymbol{r}) = \frac{1}{2}\sum_{k}\sum_{n} f(E_{nk})|\nabla\psi_{nk}(\boldsymbol{r})|^2 \tag{4.3}$$

that depends on the gradient of the WF ψ_{nk} components and the Fermi distribution f.

Density of States and atom-projected Density of states. The density of states (DOS) [67] is the number of states that are accessible to the system per energy unit. The atom-projected DOS measures how an atom or a group of atoms participate in the formation of the DOS; it is calculated by projecting the wave function onto hydrogen-like functions centered at the atomic site.

Orbital Polarization. The orbital polarization [107] represents the relative electron occupancy of two orbitals. It is defined for two sets of atomic orbitals a and b as:

$$\mathcal{P}_{a,b} = \frac{n_a - n_b}{n_a + n_b} \tag{4.4}$$

where n_a and n_b are the occupation numbers of the respective orbitals. $\mathcal{P}_{a,b}$ is a measure of the excess of charge occupation in the orbital a compared to the one in b. By selecting the sets of orbitals corresponding to particular regions of the space, it is possible to investigate the nature of the charge transfers within the system.

Bond Covalency. The covalency of a bond is a measure of the amount of charge density shared between two atoms when forming the bond. Among the existing definitions, we adopt the one based on the atom-projected density of states as in the following [108].

The center of mass of an atomic orbital $|n, l, m_l, m_s>$ of an atom A in the range energy $[E_0, E_1]$ is defined as

$$cm^A(n, l, m_l, m_s) = \frac{\int_{E_0}^{E_1} E g^A_{|n,l,m_l,m_s>}(E)dE}{\int_{E_0}^{E_1} g^A_{|n,l,m_l,m_s>}(E)dE}, \tag{4.5}$$

where $g^A_{|n,l,m_l,m_s>}$ is the contribution of the atomic orbital $|n, l, m_l, m_s>$ of the atom A to the total density of state of the solid $g(E)$:

$$g(E) = \sum_{A}\sum_{n,l}\sum_{m_l,m_s} g^A_{|n,l,m_l,m_s>}(E). \tag{4.6}$$

The bond covalency is then defined as

$$C_{A,B} = -|cm^A - cm^B|, \tag{4.7}$$

which is a measure of the overlap of the charge density formed by the A and B atoms. With this definition, the greater the value of $C_{A,B}$, the higher the overlap, the larger the covalent character of the A–B bond. According to this definition, the bond covalency is indicated in units of energy.

4.2 Phonons

In the previous chapter, we discussed the electronic structure inside the material. We will now see how we can use the vibrational excitations of the crystal as a way to predict the frictional behaviour, after introducing the notion of phonons.

A *phonon* is a collective excitation of a periodic, elastic arrangement of atoms or molecules in condensed matter. We have seen in section 3.5 that the crystal periodicity is defined by the primitive cell, the smallest unit needed to generate the infinite lattice by translation. In the following, we use the index l to label each cell, and the vector $\mathbf{r}_l$ to identify its position. If there are N atoms per cell, their equilibrium positions will be specified by the set of vectors $\mathbf{r}^0_{\kappa l}$:

$$\mathbf{r}^0_{\kappa l} = \mathbf{r}_l + \mathbf{r}^0_\kappa, \tag{4.8}$$

with $\kappa = 1, ..., N$ and $l = 1, 2, ...$. At time t, the κ-th atom within the l-th primitive cell, will be at the position $\mathbf{r}_{\kappa l}(t)$.

For a general conservative system close to the equilibrium, the potential energy V of a system that is subjected to a small elastic deformation can be Taylor expanded up to the second order in the time-dependent displacement $\mathbf{u}_{\kappa l}(t) = \mathbf{r}_{\kappa l}(t) - \mathbf{r}^0_{\kappa l}$. If we consider all the atoms and all the possible directions of oscillations, the expansion reads

$$V = V^0 + \sum_{\kappa l}\sum_{\alpha=1}^{3} u^\alpha_{\kappa l}(t)\left(\frac{\partial V}{\partial u^\alpha_{\kappa l}}\right)_0 + \frac{1}{2}\sum_{\kappa l}\sum_{\kappa' l'}\sum_{\alpha=1}^{3}\sum_{\beta=1}^{3} u^\alpha_{\kappa l}(t)\left(\frac{\partial^2 V}{\partial u^\alpha_{\kappa l}\partial u^\beta_{\kappa' l'}}\right)_0 u^\beta_{\kappa' l'}(t) \tag{4.9}$$

where the Greek letters are the Cartesian indices and the derivatives are evaluated at the equilibrium.

At the equilibrium, the first derivative is equal to zero and so the first order term vanishes. V_0 is a constant that can be set to zero by shifting the reference

energy. This is equivalent to saying that the elastic response is a linear function of the force [67]. The potential energy then reads:

$$V = \frac{1}{2}\sum_{\kappa l}\sum_{\kappa' l'}\sum_{\alpha=1}^{3}\sum_{\beta=1}^{3} u_{\kappa l}^{\alpha}(t) V_{\alpha\beta}(\kappa l, \kappa' l') u_{\kappa' l'}^{\beta}(t) \tag{4.10}$$

with

$$V_{\alpha\beta}(\kappa l, \kappa' l') = \left(\frac{\partial^2 V}{\partial u_{\kappa l}^{\alpha} \partial u_{\kappa' l'}^{\beta}}\right)_0 \tag{4.11}$$

We can then define the force constant matrix as

$$\mathbb{V}(\kappa l, \kappa' l') = \begin{bmatrix} V_{11}(\kappa l, \kappa' l') & V_{12}(\kappa l, \kappa' l') & V_{13}(\kappa l, \kappa' l') \\ V_{21}(\kappa l, \kappa' l') & V_{22}(\kappa l, \kappa' l') & V_{23}(\kappa l, \kappa' l') \\ V_{31}(\kappa l, \kappa' l') & V_{32}(\kappa l, \kappa' l') & V_{33}(\kappa l, \kappa' l') \end{bmatrix} \tag{4.12}$$

where each element corresponds to the interaction constant between the κ-th and the κ'-th atoms in the l-th and l'-th cell, respectively.

If we consider $\mathbf{p}_{\kappa l}$ and m_κ respectively as the momentum and the mass of the atom κ in the unit cell replica l, the Hamiltonian of the harmonic crystal can be written as

$$\hat{H} = \sum_{\kappa l}\frac{\mathbf{p}_{\kappa l}^2}{2m_\kappa} + \frac{1}{2}\sum_{\kappa l}\sum_{\kappa' l'}\mathbf{u}_{\kappa l}\mathbb{V}(\kappa l, \kappa' l')\mathbf{u}_{\kappa l} \tag{4.13}$$

and the force applied on the atom is of the spring type. As a consequence, the equation of motion for the atom κ reads [109]

$$m_\kappa \frac{d^2\mathbf{u}_{\kappa l}}{dt^2} = -\sum_{\kappa' l'}\mathbb{V}(\kappa l, \kappa' l')\mathbf{u}_{\kappa' l'} \tag{4.14}$$

with the solution

$$\mathbf{u}_{\kappa l}^{\pm}(\mathbf{q}, j) = \frac{1}{\sqrt{N m_\kappa}}\mathbf{e}_\kappa(\mathbf{q}, j) e^{i(\mathbf{q}\cdot\mathbf{r}_{\kappa l} \pm \omega_{\mathbf{q},j} t)} \tag{4.15}$$

which is a plane wave characterized by the wavevector $\mathbf{q}$, the polarization vector $\mathbf{e}_\kappa$ and oscillation frequency $\omega_{\mathbf{q},j}$. At each wave vector $\boldsymbol{q}$, the index $j = 1, ..., 3N$ identifies the vibrational mode; such vibrational modes are termed *phonons*. It is important to stress that for each wavevector $\mathbf{q}$, there are $3N$ different modes of vibration characterized by a displacement direction $\mathbf{e}_\kappa$ and an oscillation frequency ω.

4.2.1 The dynamical matrix

When using Equation 4.15 as a solution of the equations of motion 4.14, we obtain the eigenvector-eigenvalue equation

$$\begin{aligned}\omega^2_{\mathbf{q},j}\mathbf{e}_\kappa(\mathbf{q},j) &= \sum_{\kappa' l'}\sqrt{\frac{1}{m_\kappa m_{\kappa'}}}\left[\mathbb{V}(\kappa l,\kappa' l')e^{i\mathbf{q}(\mathbf{r}_{l'}-\mathbf{r}_l)}\right]\mathbf{e}_{\kappa'}(\mathbf{q},j)\\ &= \sum_{\kappa'}\sqrt{\frac{1}{m_\kappa m_{\kappa'}}}\left[\sum_{l'}\mathbb{V}(\kappa l,\kappa' l')e^{i\mathbf{q}(\mathbf{r}_{l'}-\mathbf{r}_l)}(\mathbf{q})\right]\mathbf{e}_{\kappa'}(\mathbf{q},j)\end{aligned} \tag{4.16}$$

where the summation runs over all the unit cells. By writing Equation 4.16 as

$$\omega^2_{\mathbf{q},j}\mathbf{e}_\kappa(\mathbf{q},j) = \sum_{\kappa'}\sqrt{\frac{1}{m_\kappa m_{\kappa'}}}\mathbb{F}_{\kappa\kappa'}(\mathbf{q})\mathbf{e}_{\kappa'}(\mathbf{q},j), \tag{4.17}$$

it becomes apparent that the matrix $\mathbb{F}$ is the Fourier transform of the force constants and contains the interactions between all the possible couple of atoms. For a given vibration $(\mathbf{q},j)$, if we combine the 3-dimensional polarization vectors $e_{\kappa'}(\mathbf{q},j)$ into a $3N$-dimensional polarization vector $\mathbf{e}(\mathbf{q},j)$, in matrix notation Equation 4.17 reads

$$\omega^2_{\boldsymbol{q},j}\mathbf{e}(\mathbf{q},j) = \left[\mathbb{M}\mathbb{F}(\boldsymbol{q})\mathbb{M}\right]\boldsymbol{e}(\boldsymbol{q},j) = \mathbb{D}(\mathbf{q})\mathbf{e}(\mathbf{q},j) \tag{4.18}$$

where $\mathbb{M}$ is the mass tensor, containing the masses of all the atoms. This is an eigenvalue-eigenvector equation. The squares of the frequencies $\omega_{\boldsymbol{q},j}$ are the eigenvalues, and the $\mathbf{e}(\mathbf{q},j)$ are the eigenvectors of the *dynamical matrix*

$$\mathbb{D}(\boldsymbol{q}) = \mathbb{M}\mathbb{F}(\boldsymbol{q})\mathbb{M}, \tag{4.19}$$

that contains the information about the dynamics of the crystal, i.e., how the atoms are moving relatively to each other. Diagonalizing $\mathbb{D}(\boldsymbol{q})$ gives the values of the frequencies $\omega^2_{\boldsymbol{q},j}$ and the eigenvectors $\mathbf{e}(\mathbf{q},j)$. The Equation 4.18 must be solved at each $\boldsymbol{q}$-point of the Brillouin zone in order to obtain a complete description of the atomic motions. The whole $3N$-dimensional set of atomic displacements $\mathbf{u}_l$ can then be written as a linear combination of the eigenvectors $\mathbf{e}(\mathbf{q},j)$ of the dynamical matrix $\mathbb{D}$ [109]:

$$\mathbf{u}_l = \frac{1}{\sqrt{N}}\sum_{\mathbf{q}}\sum_{j}Q_{\mathbf{q},j}\mathbb{M}\mathbf{e}(\mathbf{q},j)e^{i(\mathbf{q}\cdot\mathbf{r}_l+\omega_{\boldsymbol{q},j}t)} \tag{4.20}$$

where the normal coordinates $Q_{\mathbf{q},j}$ are coefficients that account for the oscillation amplitude of each particular mode $(\mathbf{q},j)$. Their value depends on the temperature of the system and have to be determined by using statistical methods.

4.2.2 Imaginary frequencies and instabilities

In the analysis of the phonon spectrum, the value of the frequencies gives us important insights on the stability of the system. Given the definition of the dynamical matrix (Equation 4.19), the eigenvalues $\omega^2_{\boldsymbol{q},j}$ are real quantities and $\omega^2_{\boldsymbol{q},j} = \omega^2_{-\boldsymbol{q},j}$. This has the following physical interpretation. As seen above, the dynamical matrix is constructed from the force constant matrix which, in turn, is built with the second derivative of the potential energy with respect to the displacements. Consequently, the phonon frequencies are a measure of the curvature of the surface of the potential energy about an equilibrium configuration: if they are positive, the curvature is positive, so the energy increases quadratically ($V \propto Q^2_{\boldsymbol{q},j}$) when atoms are slightly displaced towards the direction corresponding to the associated eigenvector. If the system is at its ground state, or at a local minimum of the potential energy surface, the eigenvalues have to be greater than zero. On the contrary, imaginary frequencies, for which $\omega^2_{\boldsymbol{q},j} < 0$, indicate that the energy decreases quadratically along the atom displacements represented by the eigenvector: the reference configuration is unstable with respect to such displacements and corresponds a saddle point of the energy. For convenience of representation in $\omega_j(\boldsymbol{q})$ band dispersion plots, imaginary frequencies are reported as negative numbers rather than imaginary ones.

4.2.3 Cophonicity

The cophonicity metric [110] is a lattice dynamic descriptor that we use to parameterize the atomic type and its effect on the vibrational properties, and to connect the latter to the electronic features of the system. The cophonicity C_{ph}(A-B) measures the relative atomic contributions to a specific range of phonon eigenfrequencies and it is defined in the following way. Let us consider a set of two interacting atoms A and B. By analogy with the center mass of an atomic orbital (section 4.1), we introduce the center mass CM^A of the phonon DOS projected on the atom A, $g^A(\omega)$:

$$CM^A = \frac{\int_{\omega_0}^{\omega_1} \omega g^A(\omega) d\omega}{\int_{\omega_0}^{\omega_1} g^A(\omega) d\omega}. \tag{4.21}$$

The integral over the frequency ω in the denominator expresses the contribution of the atom A to the total phonon density of states.

The relative position of the center mass of $g^A(\omega)$ with respect to the center mass of $g^B(\omega)$ is given as:

$$C_{ph}(\text{A-B}) = CM^A - CM^B, \tag{4.22}$$

the units being the same as those of the frequency ω. A positive (negative) sign of C_{ph}(A-B) implies that the A (B) atom contributes more to the high frequency modes of the specified range. The closer $|C_{ph}$(A-B)$|$ is to zero, the more A and B contributions to the frequency band are mixed. In this case we can say that the two atoms have the same weight in the determination of the modes specific to the considered energy range. As we will see in the results part (chapter 5), the value depends on the frequency range $[\omega_0, \omega_1]$, which is selected according to the part of the phonon spectrum that we want to investigate.

4.3 Sliding-related vibrational modes in a crystal

Friction is the result of the interactions resisting the relative motion of neighboring atoms; it is therefore important to distinguish the various contributions at the nanoscale. The *microscopic friction* is defined as the friction created at the atomic scale by the relative motion of adjacent atom layers. It includes the presence of structural irregularities, such as dislocations and layer truncations, that exist in a non-ideal crystal. If the structure is free from defects and irregularities, and the microscopic friction is due to only to the local electronic (depending on the atomic types) and structural features (geometry), it is termed as *intrinsic friction* [37]. In the following discussion, we will focus on the intrinsic friction and will refer to it simply as "friction". The dynamical process of friction occurring during the motion of two adjacent layer planes of atoms can be studied by detailing the interaction of such planes in translation on top of each other. However, since this is a time dependent process, the study of it would require long ab initio dynamic simulations which are very demanding in terms of computational resources. As an alternative, we choose to analyse the vibrational contributions of the atoms to the intrinsic friction; in this respect, several previous studies on similar TMD materials already observed that specific low frequency phonon modes are directly related to the sliding of adjacent layers [110, 37].

As a first approximation, friction can be described as a harmonic restoring force f, that follows Hooke's law

$$f = -Cx = m\omega^2 x, \tag{4.23}$$

with x being the relative layer displacement, m the mass of the system, C the force constant, and ω a characteristic frequency. A translation in space can be described as a particular linear combination of atomic displacements, mathematically represented by the phonon eigenvectors. Since at each **q**-point the set of eigendisplacements constitutes a basis for the Cartesian components of the atomic positions,

there is then a one-to-one correspondence between the Cartesian and the phonon description of the sliding event. The phonons that have the largest component in the linear combination representing the layer sliding are called *sliding-related* phonons. At a constant system energy, the lower the frequency of these modes, the higher the amplitude of the corresponding atomic displacement. When the displacement is associated to a layer sliding (translation), high amplitudes correspond to large shifts of one layer with respect to another adjacent one. A lower frequency then corresponds to a facilitated sliding. Consequently, it was shown that the translation, hence the intrinsic friction, can be finely tuned by acting on these particular sliding related modes [110]. In such a study, the projection of the components of the displacement vectors showed that there were only a few of these sliding related modes. A sliding-related phonon mode may be responsible of pure rigid layer translations or of layer shifts combined with intralayer motions, like stretching and/or bending of the atomic bonds. Such layer shifts can occur along directions either parallel or orthogonal to the MX_2 sheets; the former are associated with the layer sliding (*shearing modes*), the latter correspond to variations of the interlayer distance (*breathing modes*). Indeed, like at the macroscopic scale, the intensity of the friction at the nanoscale depends on the interplane distance.

Using a standard convention, the labels of the modes are specified by increasing integers, corresponding to dispersion branches with increasing frequencies. As an example, the $\Gamma(4)$ mode corresponds to the 4th branch at the Γ point of the reciprocal lattice. The frequency of the $\Gamma(5)$ is higher or equal (because of the degeneracy in our case) to the one of $\Gamma(4)$, and the frequency of $\Gamma(6)$ is higher than those of the previous modes. At the Γ point, the shearing modes are the 4th and 5th modes, and are related to rigid sliding along the a and b crystallographic axes, while the 6th mode is a breathing mode (Figure 4.1). When following the acoustic branches from the Γ point towards the A point, we can see that the rigid sliding-related modes in Γ continuously transform into composite modes at the A point. These modes also contribute to the sliding as they describe shifts between the layers, also including intralayer displacements. The goal here is to find a way to modify the frequency of these identified sliding modes, by acting on the electronic structure with a fine engineering of the cation environment or with the use of external electrostatic fields.

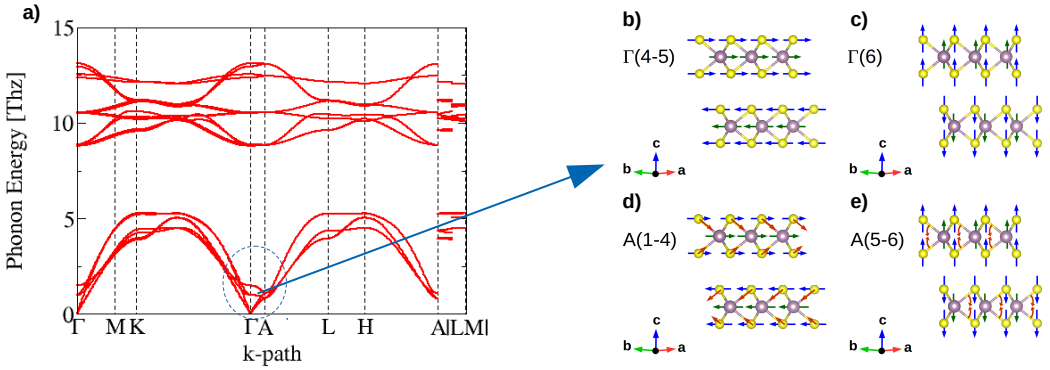

Figure 4.1: Identification of the phonon modes associated to the sliding. The notation $\Gamma(4-5)$ $A(1-4)$ is used to signify the range of modes that are degenerated. (a) Phonon band structure of MoS_2 computed along the path connecting the high symmetry points in the first Brillouin zone. (b) Rigid sliding modes $\Gamma(4-5)$ and (c) breathing mode $\Gamma(6)$. (d) $A(1-4)$ and (e) $A(5-6)$ composite sliding modes at the A point. Blue arrows symbolize interlayer displacements while red arrows indicate intralayer displacements.

4.4 The modern theory of polarization

Finite-field calculations in periodic insulators is not a trivial technical task, as it has been difficult to correctly define the polarization in extended solids, even conceptually.

In a molecule, the dipole moment $\mathbf{d}$ of a collection of charges q_i at the positions $\mathbf{r}_i$ is defined as:

$$\mathbf{d} = \sum_i q_i \mathbf{r}_i. \tag{4.24}$$

The difficulty arises when dealing with periodic boundary conditions in the presence of an electric field. In a periodic system, the usual way to define a quantity is to express it as this quantity per unit volume, or unit mass. The quantity is then evaluated in the unit cell and normalized over the cell volume. In our case, the electric polarization should be represented by the electric dipole moment per unit cell. For the sake of the example, let us write the case of a finite number of point charges in a 1−D system:

$$\mathbf{P} = \frac{1}{a} \sum_i q_i \mathbf{x}_i, \tag{4.25}$$

the units being charge per unit length. As it is apparent in Figure 4.2, the choice of the unit cell becomes critical, as two equally valid unit cells can have completely opposite orientations of the polarization. Here for the cell on the left $\mathbf{P} = 1/2\hat{\mathbf{e}}_x$,

Figure 4.2: Two different choices of representative unit cells, indicated by the dashed lines, in a one-dimensional chain of alternating anions and cations. a is the lattice constant. Though both are valid, the unit cells present opposite polarizations.

while for the cell on the right $\mathbf{P} = -1/2\hat{\mathbf{e}}_x$. Therefore, the polarization defined in Equation 4.25 cannot be applied to periodic systems.

This ambiguity requires a reformulation of the expression for the polarization. This was done by Stengel and coworkers [111] in 2009, with their Modern Theory of Polarization (MTP). When an external electric field is applied to a non polar bulk material (like a TMD) along a specific direction, a change of the polarization can occur. Such change is a quantity that can be measured, using the Sawyer-Tower method [112], for example in the case of the spontaneous polarization of a ferroelectric. Let's now rewrite Equation 4.25 in the more realistic hypothesis of a continuous electronic charge density $en(\mathbf{r})$:

$$\mathcal{P} = \frac{1}{\Omega} \int d\mathbf{r} en(\mathbf{r}) \mathbf{r} \tag{4.26}$$

where the number density $n(\mathbf{r})$ is calculated as a sum over the occupied states:

$$n(\mathbf{r}) = \sum_{n}^{occ} |\psi_n(\mathbf{r})|^2. \tag{4.27}$$

The issue here lies in the fact that the position operator appearing in Equation 4.26 is not compatible with the Born-von Karman boundary conditions. In a cell with lattice vectors $\mathbf{a}_i$ $(i = 1, 2, 3)$, the latter requires that $\psi(\mathbf{r}) = \psi(\mathbf{r} + m_i \mathbf{a}_i)$ for a set of integers m_i. Moreover, an operator is supposed to map a function of this Hilbert space into a function belonging to the same space. It is trivial to show that, if $\psi(\mathbf{r})$ is periodic, $\mathbf{r}\psi(\mathbf{r})$ is not, and so $\mathbf{r}$ is not a viable operator in infinite solids [113]. As we will see below, $\mathbf{r}$ is replaced by a Berry-phase expression. This removes possible potential discontinuities and the mathematical difficulties created by the unbound nature of the electric perturbation term.

Under the effect of a finite electric field $\mathbf{E}$, the total energy of the crystal to

minimize is [111]

$$E = E_0 - \Omega \mathbf{P} \cdot \mathbf{E} \tag{4.28}$$

with E_0 being the ground state energy obtained in the absence of the electric field, $\mathbf{P}$ the total polarization containing an ionic and an electronic contributions, and Ω the volume of the unit cell. The electronic part can be computed following the Modern Theory of Polarization. In the MTP, the change in the electric polarization per unit volume that is induced by an adiabatic change in the crystalline potential v_λ is written as

$$\Delta \mathbf{P} = \int_{\lambda_1}^{\lambda_2} \frac{\delta \mathbf{P}}{\delta \lambda} d\lambda, \tag{4.29}$$

the parameter λ describing a continuous path in the space of the Khon-Sham Hamiltonians [114]. From Equation 4.26 and the expresion of $n(\mathbf{r})$, the derivative with respect to λ writes as:

$$\frac{d\mathbf{P}}{d\lambda} = -\frac{e}{\Omega} \sum_n^{occ} \left\langle \psi_n^\lambda \right| \mathbf{r} \left| \frac{d\psi_n^\lambda}{d\lambda} \right\rangle + c.c. \tag{4.30}$$

At the first order of the perturbation theory, the ket is approximated as

$$\left| \frac{d\psi_n^\lambda}{d\lambda} \right\rangle = \sum_{m \neq n} \left| \psi_m^\lambda \right\rangle \frac{\left\langle \psi_m^\lambda \right| \frac{dv_\lambda}{d\lambda} \left| \psi_n^\lambda \right\rangle}{\epsilon_n - \epsilon_m}; \tag{4.31}$$

plugging it into Equation 4.30 yields

$$\frac{d\mathbf{P}}{d\lambda} = -\frac{e}{\Omega} \sum_n^{occ} \sum_{m \neq n} \frac{\left\langle \psi_n^\lambda \right| \mathbf{r} \left| \psi_m^\lambda \right\rangle \left\langle \psi_m^\lambda \right| \frac{dv_\lambda}{d\lambda} \left| \psi_n^\lambda \right\rangle}{\epsilon_n - \epsilon_m} + c.c. \tag{4.32}$$

which is the expression of the variation of the polarization due to a variation of the crystalline potential. From the commutation relation with the Hamiltonian, $[\mathbf{r}, \hat{H}_\lambda] = \frac{i\hbar \mathbf{p}}{m_e}$, the non diagonal terms can be rewritten as

$$\frac{ie\hbar}{m_e \Omega} \frac{\left\langle \psi_n^\lambda \right| \mathbf{p} \left| \psi_m^\lambda \right\rangle}{\epsilon_n - \epsilon_m} \tag{4.33}$$

leading to:

$$\frac{d\mathbf{P}}{d\lambda} = \frac{ie\hbar}{m_e \Omega} \sum_n^{occ} \sum_{m \neq n} \frac{\left\langle \psi_n^\lambda \right| \mathbf{p} \left| \psi_m^\lambda \right\rangle \left\langle \psi_m^\lambda \right| \frac{dv_\lambda}{d\lambda} \left| \psi_n^\lambda \right\rangle}{(\epsilon_n - \epsilon_m)^2} + c.c. \tag{4.34}$$

It should be noted that this quantity doesn't depend on the cell, nor on the phase chosen for the Bloch function. It uniquely specifies the macroscopic polarisation change due to an adiabatic change of the crystal potential.

From this, it can be shown that the change in polarization ΔP can be written as a sum of ionic and electronic terms [113]:

$$\Delta \mathbf{P} = \Delta \mathbf{P}_{ion} + \Delta \mathbf{P}_{el} \tag{4.35}$$

The ionic contribution can be computed classically, by considering ions as classical point charges eZ_μ summed over the cell,

$$\mathbf{P}_{ion}(\lambda) = \frac{e}{\Omega} \sum_{\mu} Z_{\mu}^{ion} r_\mu \tag{4.36}$$

while $\mathbf{P}_{el}$ is computed as a Berry phase, meaning that it is a gauge invariant phase of the WF [115]:

$$\mathbf{P}_{el}(\lambda) = -\frac{2ie}{(2\pi)^3} \int_{BZ} d\boldsymbol{k} \sum_{n} \left\langle u_{n\boldsymbol{k}}^{\lambda} \right| \nabla_{\mathbf{k}} \left| u_{n\boldsymbol{k}}^{\lambda} \right\rangle , \tag{4.37}$$

where e is the electron charge, the factor 2 accounts for the spin, and the $u_{n\boldsymbol{k}}^{\lambda}$ represents the periodic part of the Bloch function. The WF derivatives are finally computed by using a finite-difference scheme, so that a coherent phase relationship between the k-points may be ensured.

4.5 Computing the response to an electrostatic field

The implementation of the modern theory of polarization in the ABINIT software is based on two methods which are available to us:

- The *finite electric field technique*, that has the advantage of being very general and easy to implement. It also allows to use the exchange-correlation energy functionals already available for zero-field ground-state calculations.

- The *density functional perturbation theory* (DFPT) approach, which offers a more systematic way to compute nonlinear response functions. By using the perturbation theory, it is possible to obtain analytic expressions of the derivatives of the energy with respect to electric fields up to any order.

We will now briefly see the details of both methods.

4.5.1 Finite electric field calculations

The concept behind the constant electric field method, as in the ABINIT implementation, relies on the direct minimization of the electric enthalpy functional $\mathcal{F}$:

$$\mathcal{F}(\mathbf{E}) = E_{KS} - \Omega \mathbf{E} \cdot \mathbf{P}, \tag{4.38}$$

defined for a finite electric field $\mathbf{E}$ and depending on the internal coordinates through the internal energy E_{KS} and the polarization $\mathbf{P}$ [111]. The subtlety here is that a new functional $\tilde{\mathcal{F}}$ is introduced for convenience:

$$\begin{aligned} \tilde{\mathcal{F}} &= U - \frac{\Omega}{4\pi} \mathbf{E} \cdot \mathbf{D} \\ &= \mathcal{F} - \frac{\Omega}{8\pi} \mathbf{E}^2. \end{aligned} \tag{4.39}$$

As seen in Equation 4.39, $\tilde{\mathcal{F}}$ and $\mathcal{F}$ differs only by a function of $\mathbf{E}$, and consequently yield the same equilibrium state for a fixed value of E, which is the case we are considering here. The electric displacement $\mathbf{D} = \mathbf{E} + 4\pi\mathbf{P}$, rather than the electric field $\mathbf{E}$ or the polarization $\mathbf{P}$, becomes the fundamental electrical variable. $\tilde{\mathcal{F}}$ is chosen to be the energy functionals for fixed electric field condition. By analogy, the internal energy $U(\mathbf{D})$, defined as

$$U(\mathbf{D}) = E_{KS} + \frac{\Omega}{8\pi} [\mathbf{D} - 4\pi\mathbf{P}]^2, \tag{4.40}$$

is chosen for a fixed displacement field condition. The minimization of the functional $\tilde{\mathcal{F}}$ is performed using the preconditioned conjugate-gradient algorithm [116]. At the minimum, Equation 4.38 gives the values of the energy and the polarization of the material at a fixed field. The Hellman-Feynman theorem is then used to compute the forces at a non-null field. In this way, the force on an atom along a direction can be computed as the sum of the standard Hellmann-Feynman term with no electric field plus a term arising from the ionic contribution [116, 117]. The force felt by an atom κ in a given direction α expresses as

$$f_{\kappa,\alpha} = -\frac{\partial E_{KS}}{\partial \lambda_{k,\alpha}} + e Z_k E_\alpha, \tag{4.41}$$

with λ being a continuous parameter. The stresses can be computed as a function of the electronic and ionic Berry phases terms summed over all the directions [116].

4.5.2 Density Functional Perturbation Theory calculations

A perturbation theory of the static response of insulating crystals to homogeneous electric fields integrating the MTP [114] has been implemented in the ABINIT software [118], later followed by the PAW extension [119] that we also use in this study. Performing phonon computations with this method is faster than the finite electric field method. However, the ABINIT implementation of the calculation of the forces on the atoms with the DFPT in the presence of a finite electric field presents some bugs when used in a multicore environment; in this case, only a serial calculation gives reliable results. Nonetheless, due to the computational requirements of our calculations, we needed to exploit the parallelization features of ABINIT to obtain the results in a reasonable time. For this reason, we made use of the finite electric field method our simulations. The bug was found during this present study together with the joint effort of ABINIT team.

4.6 CI-NEB method and energy barrier

To study the energy barrier preventing the sliding of one layer on top of the other we use the *climbing image nudged elastic band* (CI-NEB) method. The CI-NEB method [120] is a modification of the *nudged elastic band* (NEB) [121] that allows to find minimum energy paths between an initial state and a final one, both corresponding to energy minima. In the present section we introduce the basics of these methods.

In the NEB method, an elastic band with $N+1$ images is expressed as a set of vectors $\mathbf{R}$ containing the geometrical positions of every atoms, $[\mathbf{R}_0, \mathbf{R}_1, \mathbf{R}_2, \ldots, \mathbf{R}_N]$, with $\mathbf{R}_0$ and $\mathbf{R}_N$ corresponding to the fixed geometric configurations realizing the initial and final minima, respectively. Since a first order saddle point is an energy maximum along one direction and an energy minimum along all the other directions, finding saddle points generally involves the simultaneous maximization of one degree of freedom and minimization of the other degrees of freedom. This is done by optimizing a set of intermediate images along the geometrical path. These images correspond to states created by the sliding of one layer on top of each other. Each image finds its lowest energy possible while maintaining equal spacing to neighboring images. The constraining is done by adding spring forces along the band between images, hence the total force acting on an image is the sum of the spring force along the local tangent $\mathbf{F}_i^S|_\parallel$ and the true force perpendicular to the local tangent $\nabla E(\mathbf{R}_i)|_\perp$:

$$\mathbf{F}_i = \mathbf{F}_i^S|_\parallel - \nabla E(\mathbf{R}_i)|_\perp \tag{4.42}$$

where E is the energy of the system, depending on the atomic coordinates.

The spring force has the simple form:

$$\mathbf{F}_i^S|_{\|} = k\left(|\mathbf{R}_{i+1} - \mathbf{R}_i| - |\mathbf{R}_i - \mathbf{R}_{i-1}|\right) \cdot \hat{\tau}_i \tag{4.43}$$

where k is the force constant and $\hat{\tau}_i$ the normalized local tangent vector at image i. The particularity of the NEB method is that during the minimization, at each image, the true force and the spring force are decomposed into these components parallel and perpendicular to the hyper-tangent between the images. Introducing only the perpendicular component of the true force, and only the parallel component of the spring force ensures that:

- the spring forces do not interfere with the convergence of the elastic band.
- the true force does not affect the distribution of images along the minimum energy path.

This choice for the force projection is referred to as "nudging". An optimization algorithm is then used to move the images according to the value of the force. Excluding a lucky scenario, none of the images lands on the saddle point and thus the saddle point energy needs to be estimated by interpolation.

In the CI-NEB method, the specificity is that the highest energy image is driven up to the saddle point. First, a few iterations using the regular NEB are performed, and the image with the highest energy is identified. Then the value of the true force at this image i_{max} along the tangent is inverted, meaning that the total force acting on this image is now

$$\mathbf{F}_{i_{max}} = -\nabla E(\mathbf{R}_{i_{max}}) + 2\nabla E(\mathbf{R}_{i_{max}})|_{\perp}. \tag{4.44}$$

The energy of the image i_{max} is maximized (hence "climbing") along the elastic band, and minimized in all other directions. The importance of the other images in the band is that they allow to define the one degree of freedom for which a maximization of the energy is performed. When this image converges, it will be at the exact saddle point, realizing the maximum of the energy along the path.

4.7 Software

In this study we use the ABINIT package [98] to perform ab initio simulations within the DFT framework. The PHONOPY software [122] is used as a post processing tool

to calculate the phonon spectrum for a subsequent analysis of the frequencies and the eigendisplacements. All the pristine TMD compounds here examined have the symmetry of the $P6_3/mmc$ space group (#194), while the structures containing a molecule have the symmetry of the $P1$ space group (#1). In both PHONOPY and ABINIT, the crystal symmetries are exploited in order to reduce the computational load.

4.8 Benchmark

We stated in subsection 3.4.2 that ad hoc parameters can suffer from a lack of transferability. It is then necessary to perform a benchmark on the fundamental input parameters (e.g., energy cutoff, BZ sampling and vdW correction) in order to reproduce the experimental structure as close as possible. We report the result of the benchmarking in Table 4.1 and compare it to experimental data [123, 124, 125, 126, 127, 128]. The vdW-WF2 [90] and vdW-QHO-WF [91] van der Waals corrections tend to overestimate the volume of the cell. The vdW-DFT-D3(BJ) [89], based on the Becke-Jonhson method [129], gives the most accurate description, and is selected to carry on the calculations in the presence of a finite field. It is worthy to mention that the vdW-DFT-D2 correction [87] has given satisfying results for the ground state calculation of similar TMDs [110, 130]. However, at the time of this study, the implementation of the latter in the ABINIT code does not include the parameterisation for the tungsten atom, and therefore cannot be used for our purposes.

4.9 Computational details

We focus here on 6 different MX_2 prototypes of layered TMDs with M = Mo, W and X = S, Se, Te. The plane defined by the a and b lattice vectors and separating the two layers of the bulk MX_2 structure is considered as our sliding plane. The exchange-correlation functional used is the Perdew-Burke-Ernzerhof [131] derived within the Generalized Gradient Approximation. As stated in the previous section, we use the vdw-DFT-D3(BJ) correction to account for vdW interactions. The choice is made after benchmarking and comparison of the simulations with the geometrical data obtained experimentally for the respective compounds. We perform Density Functional Theory calculations with a plane-wave energy cutoff set to a minimum of 18.4 Ha. The Brillouin zone is sampled with a minimum of $7\times7\times5$ k-mesh divisions. We consider that we achieve convergence of the electronic distribution when the

Table 4.1: Geometry parameters obtained by using the PBE functional with various choices of vdW corrections. The best correspondence with the experimental data is obtained by using the long range dispersion correction vdW-DFT-D3. For all the structures, the symmetry space group is $P6_3/mmc$ (symmetry table number 194). Angles between the primitive vectors are α=90°; β=90°; γ=120 °.

Experimental data								
			M			X		
System	$a=b$	c	x	y	z	x	y	z
MoS_2[123]	3.1610	12.2950	⅓	⅔	¼	⅓	⅔	0.6275
$MoSe_2$[124]	3.2880	12.9300	0	0	¼	⅓	⅔	0.1220
$MoTe_2$[125]	3.5170	13.9490	⅓	⅔	¼	⅓	⅔	0.6250
WS_2[126]	3.1532	12.2401	⅓	⅔	¼	⅓	⅔	0.6225
WSe_2[127]	3.2860	12.9800	⅔	⅓	¼	⅓	⅔	0.1200
WTe_2[128]	3.4910	14.3100	⅓	⅔	¼	⅓	⅔	0.6210
vdW-WF2								
			M			X		
System	$a=b$	c	x	y	z	x	y	z
MoS_2	3.1910	13.7735	⅓	⅔	¼	⅓	⅔	-0.1365
$MoSe_2$	3.5775	12.9097	⅓	⅔	¼	⅓	⅔	-0.1277
$MoTe_2$	3.5203	14.3680	⅓	⅔	¼	⅓	⅔	-0.1195
WS_2	3.1778	12.4191	⅓	⅔	¼	⅓	⅔	-0.1237
WSe_2	3.4297	13.0040	⅓	⅔	¾	⅓	⅔	0.3741
WTe_2	3.5203	14.3680	⅓	⅔	¼	⅓	⅔	-0.1226
vdW-QHO-WF								
			M			X		
System	$a=b$	c	x	y	z	x	y	z
MoS_2	3.1906	14.1619	⅓	⅔	¼	⅓	⅔	-0.1395
$MoSe_2$	3.5775	12.9097	⅓	⅔	¼	⅓	⅔	-0.1277
$MoTe_2$	3.5189	13.9530	⅓	⅔	¼	⅓	⅔	-0.1195
WS_2	3.1913	13.9849	⅓	⅔	¼	⅓	⅔	-0.1376
WSe_2	3.4956	13.3404	⅓	⅔	¾	⅓	⅔	0.3703
WTe_2	3.5203	14.3680	⅓	⅔	¾	⅓	⅔	-0.1226
vdW-DFT-D3(BJ)								
			M			X		
System	$a=b$	c	x	y	z	x	y	z
MoS_2	3.1556	12.2368	⅓	⅔	¼	⅓	⅔	-0.1220
$MoSe_2$	3.2862	12.8660	⅓	⅔	¾	⅓	⅔	0.3801
$MoTe_2$	3.5172	13.8237	⅓	⅔	¾	⅓	⅔	0.3816
WS_2	3.1601	12.2401	⅓	⅔	¾	⅓	⅔	0.3787
WSe_2	3.2885	12.9228	⅓	⅔	¼	⅓	⅔	-0.1196
WTe_2	3.5197	13.8306	⅓	⅔	¾	⅓	⅔	0.3819

difference of the total energy calculated between two subsequent Self Consistent Field cycles occurs twice in a row to be less than 10^{-12} Ha. The electrostatic field is applied perpendicular to the sliding plane, along the c crystallographic axis. The electric field values range from 0 to 0.0025 a.u., which correspond to a range of 0 to $\sim$ 1.28 V/nm. For some of the prototypes, at some values of the field, we observe some unstable displacements. The latter can be removed only by changing the value of the field. For this reason, the values of the field used can vary depending on the type of system.

Chapter 5

Effect of the electric fields on the intrinsic friction in transition metal dichalcogenides

During this PhD study, we completed three core investigations, each representing a different angle of approach in controlling the nanotribological behaviour of TMDs. In the present chapter, we propose a case study of the effect of an electrostatic field on the nanoscale frictional properties. The article reporting this study is mentioned in Ref. [132]; in what follows, we summarize the methodology and the main results.

We begin the study by optimizing the 6 selected prototypes by using the lattice data cited in section 4.8, in the absence of any field. We then apply an electrostatic field along an axis orthogonal to the atom layers. The impact on the systems can be seen at various structural levels. First, the ground state geometry of the starting point was modified: as shown in Figure 5.1, the largest volume variation is found for the $MoSe_2$, $MoTe_2$, and WSe_2 systems, mainly due to the change in the length of the **c** lattice vector; this is expected, since such crystallographic axis is parallel to the direction of the applied field **E**. It is important to note that the range of values of the electric field is not common for all the systems. Some structures become unstable when the field value reaches a certain threshold depending on the chemical composition.

Regarding the phonon spectrum, we observe that an increase of the field produces a general hardening of the modes along the Γ-A linear path; at the same time, some sliding branches are softened and may become unstable beyond some critical field value E ($E = |\mathbf{E}|$), depending on the system. This is what is observable when we consider the average frequency ω as a function of E (Figure 5.2): the MoS_2, WS_2 and WTe_2 systems are the most stable ones against large field perturbations

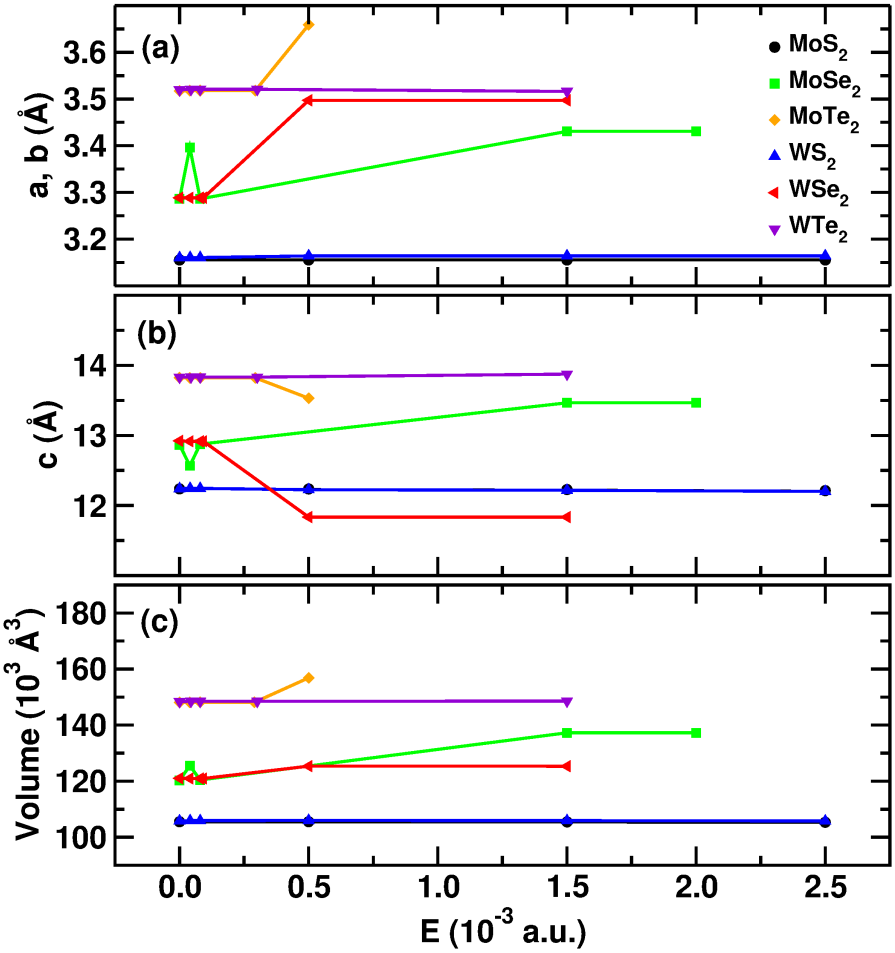

Figure 5.1: The effect of the electric field on the lattice parameters of the model systems is visible here: (a) lattice constants a and b, (b) lattice constant c, (c) cell volume. Values relative to MoS_2 and WS_2 systems are almost identical. Lines are a guide for the eye.

while, in the remaining compounds, some of the sliding modes become unstable already at $E = 0.5 \times 10^3$ a.u. The dependency of each sliding and breathing mode frequency as a function of the field is reported in Figure 5.3, where we plotted the phonon band structures for each system. We can see the appearance of branches with negative frequencies upon the activation of the field. As stated in section 4.3, the frictional force is directly related to the frequency of the sliding modes. There is no clear relation between the magnitude of the field, the phonon frequency, and the atomic types. This shows that the coupling between the electronic structure and the dynamical response of the system is not trivial.

In order to disentangle the contribution of the two responses, we quantify how the electronic charge redistributes across the structure under the effect of the field. To this end, we use the orbital polarization descriptor defined in section 4.1. We

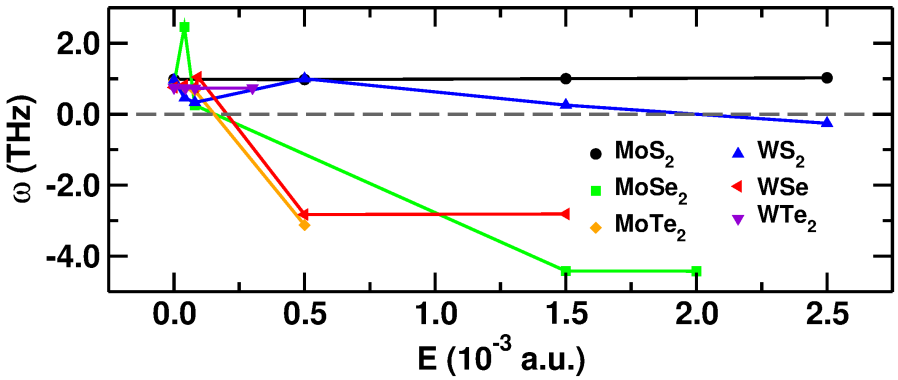

Figure 5.2: Average frequency as a function of the applied electrostatic field. Instabilities arise when the field magnitude is above a threshold value. Lines are a guide for the eye.

consider the p_x , p_y and p_z orbitals centered at the anion sites, and the t_{2g} and the e_g orbitals centered at the cation sites, in order to calculate the following polarizations: $\mathcal{P}_{p_x,p_y}$, $\mathcal{P}_{p_x,p_z}$, $\mathcal{P}_{p_y,p_z}$, $\mathcal{P}_{t_{2g},e_g}$, $\mathcal{P}_{d_{x^2-y^2},d_{z^2}}$ (Figure 5.4). We do not notice any significant change in the relative occupation of the p_x with respect to the p_y orbital with the presence of the field. The fluctuation around zero of $\mathcal{P}_{p_x,p_y}$ indicates that the electrons are equally distributed between the two orbitals. This behaviour is expected given the symmetries present in the a, b plane; similarly, we observe the same trend both for $\mathcal{P}_{p_x,p_z}$ and $\mathcal{P}_{p_y,p_z}$ orbital polarizations (Figure 5.4(b-c)). The negative values of $\mathcal{P}_{p_x,p_z}$ and $\mathcal{P}_{p_y,p_z}$ imply an excess of electrons along an axis orthogonal to the layers at the anion site. This excess remains nearly constant regardless the value of the applied field. When looking into the relative occupation of the t_{2g} and e_g orbitals, in the $MoSe_2$, $MoTe_2$ and WSe_2 systems, we notice that an increase of the field induces a transfer of electrons towards the e_g orbitals (Figure 5.4(d)), in detail from the $d_{x^2-y^2}$ to the d_{z^2} orbital (Figure 5.4(e)). This denotes a charge transfer along an axis orthogonal to the a, b plane and passing through the cation sites. On the contrary, in the MoS_2, WS_2, and WTe_2 systems the variation of the field leaves almost unchanged both the P_{t_{2g},e_g} and $P_{d_{x^2-y^2},d_{z^2}}$ polarizations.

The transfer can be visualized by looking into the projections of selected charge density differences $\rho(E)$ (Figure 5.5)

$$\rho(E) = \rho(\boldsymbol{E}) - \rho(\mathbf{0}), \tag{5.1}$$

where $\rho(\boldsymbol{E})$ is the charge density of the optimized structure in the presence of non-null field $\boldsymbol{E}$, and $\rho(\mathbf{0})$ is the charge density relative to the structure relaxed in the absence of field. The red lobes, that point along the $\boldsymbol{c}$-direction orthogonal to the

layer planes, represent the portion of space where an accumulation of charge occurs when compared to the null-field case.

At this point, the present analysis suggests that the applied field induces an accumulation of charge along the $\boldsymbol{c}$ direction in the $MoSe_2$, $MoTe_2$ and WSe_2 systems. The result is a significant variation of the c lattice constant (Figure 5.1) and the consequent instability of the sliding modes (Figure 5.2).

It was shown [133] that the covalency of the M–X bonds in TMDs can be affected by the changes in the charge distribution. A quantification of the effect of the field on the bonds is here necessary. We then calculate the bond covalency $C_{M,X}$ introduced in section 4.1. The relation between $C_{M,X}$ and the polarization of the d orbitals is then plotted in Figure 5.6. In MoS_2, $MoSe_2$ and $MoTe_2$ systems, the bond covalency is nearly constant despite the large variation of the orbital polarizations; in WS_2 and WSe_2 systems, the covalent character of the bond is more sensitive to the charge rearrangement. In the case of the WTe_2 compound, the variation of the orbital polarization is too small to induce significant changes in the bond covalency. This shows that there is no trivial relation connecting the mode eigendisplacements and frequency (and consequently, the atomic motions) and the covalency, the orbital polarizations, and the atomic types forming the structure.

That being said, the interatomic forces, that determine the dynamic response of a system, are imposed by the type of atoms and the geometry shaping the electronic environment. The values of the mode frequencies of the system are determined by the interatomic force constant tensor that is involved in the dynamical matrix. It is then necessary to find a way to parameterize the effect of the atomic type on the coupling between the electronic and the atomic structure. The use of the cophonicity metric C_{ph}(M-X) introduced in subsection 4.2.3 can then help us to quantify such effect.

The cophonicity values that we obtained in absence of electrostatic field are similar to those realized previously in finite n-layered TMDs [37]. We compute C_{ph}(M-X) in the frequency range including the sliding-related modes, and plot its evolution with the field, and its connection to the modes frequency in Figure 5.7. What we observe is that the cophonicity is nearly constant for low values of the electric field, i.e., when the system is still stable. In this respect, we can consider it as an intrinsic characteristic of the stable system. For each system, there is a critical electric field beyond which the cophonicity deviates significantly from the value at zero field. Over this threshold, the structure becomes highly unstable against the sliding and breathing distortions. This corresponds to a more pronounced relative layer motion than what is observed for low values of the field field. In Figure 5.7(b),

we see that in general the systems are stable when the C_{ph}(M-X) is close to zero.

Let us illustrate the meaning of this result: if the overall layer displacement is formed by atomic motions in which the M and X atoms move on average at the same velocity, the sliding is favored at low electric field values; on the contrary, higher field values require that cations and anions move at a very different velocity in order to produce easy gliding of the layers. The present case study could be extended by considering different geometric configurations, corresponding to other local energy minima. This would allow access to a more complete set of values for the electric field, facilitating the identification of additional parameters.

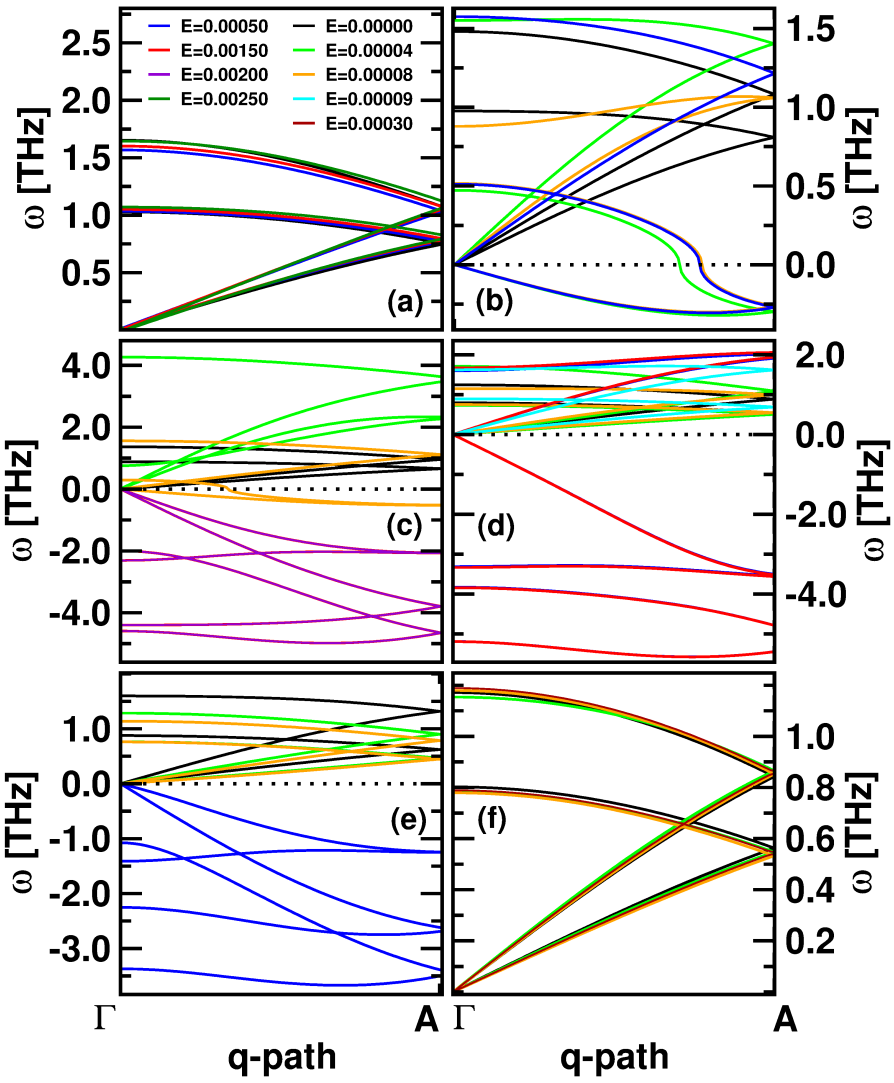

Figure 5.3: Phonon dispersion of $\Gamma - A$ modes for each of the studied MX_2 systems. The set of electric field values is different for each system, due to instabilities shown by the negative frequencies (see discussion above). For an optimal visualization of the band structures, all the values are collected in the same legend.

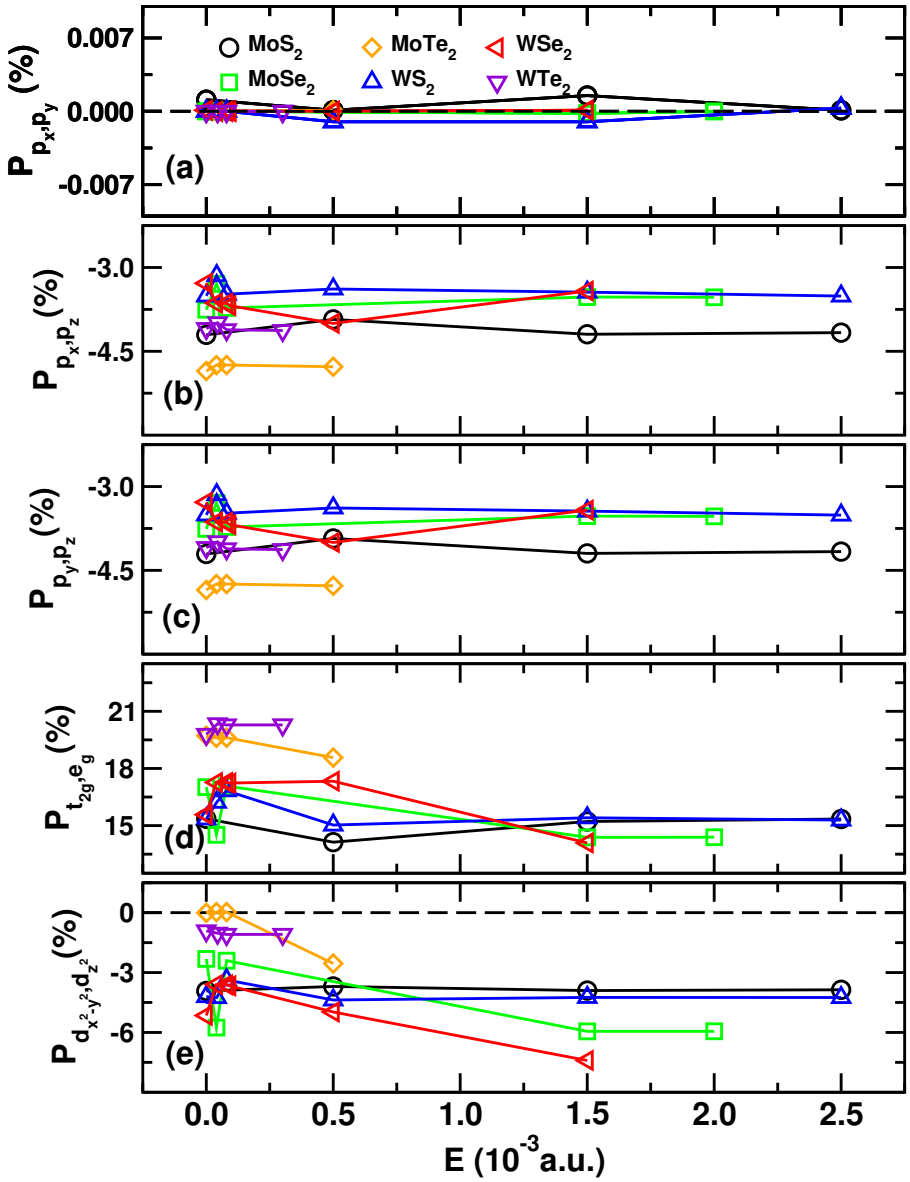

Figure 5.4: Orbital polarization of the MX_2 systems as a function of the electric field. An increase of the field magnitude induces a charge transfer along the direction orthogonal to the lattice planes. Legend is common to all the subplots; lines are a guide for the eye.

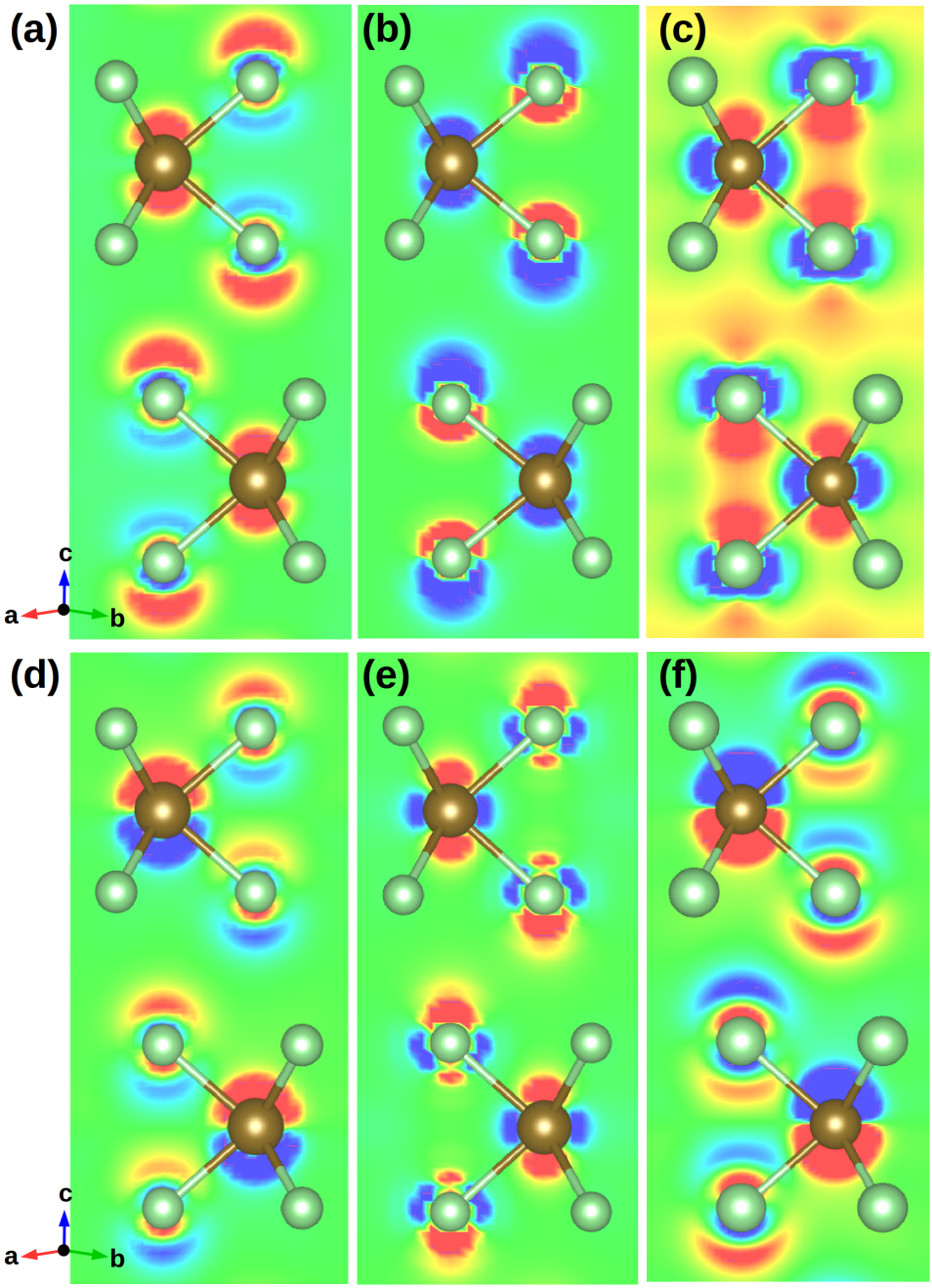

Figure 5.5: Projections of the charge density difference onto a plane orthogonal to the (110) crystallographic direction and containing the M cations: (a) MoS_2, $\rho(1.5)$; (b) $MoSe_2$, $\rho(2.0)$; (c) $MoTe_2$, $\rho(0.5)$; (d) WS_2, $\rho(1.5)$; (e) WSe_2, $\rho(1.5)$; (f) WTe_2, $\rho(0.08)$. The charge difference values are represented (red = highest, blue = lowest) by a RGB color gradient.

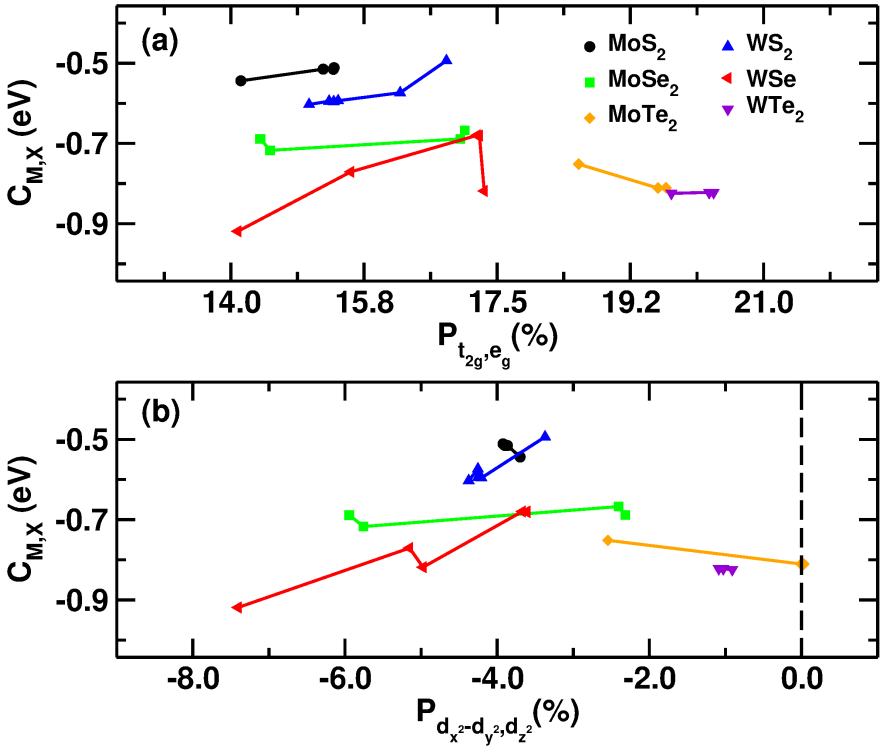

Figure 5.6: M-X bond covalency as a function of the d orbitals: (a) $\mathcal{P}_{t_{2g},e_g}$ and (b) $\mathcal{P}_{d_{x^2-y^2},d_{z^2}}$ orbital polarizations. Depending on the system, the charge rearrangement does not affect the covalent character of the bond. The legend is common to both subplots.

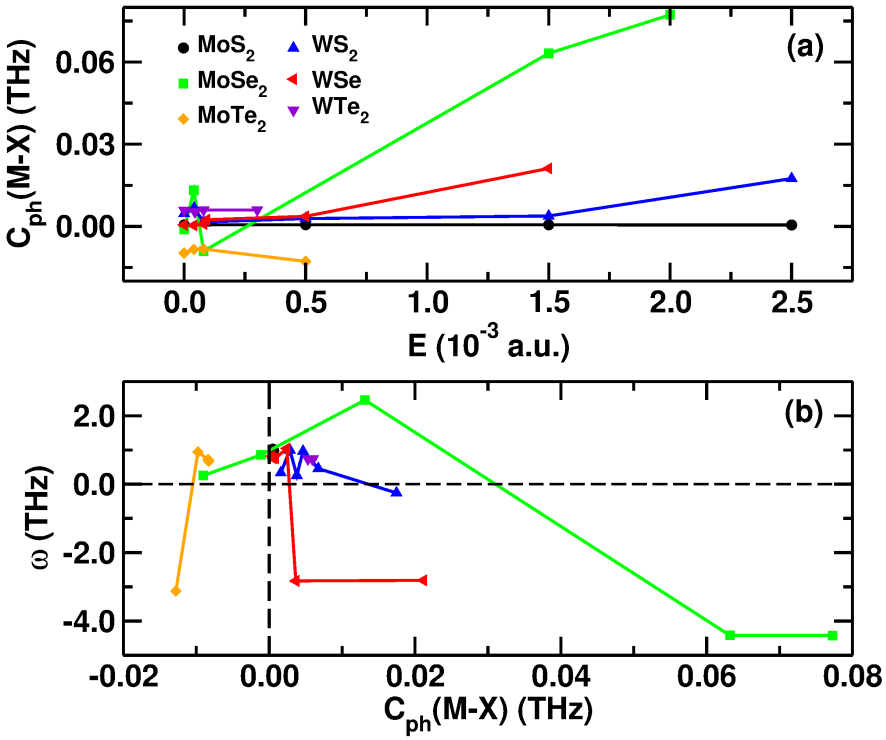

Figure 5.7: (a) Cophonicity of the M-X pair as a function of the electric field. (b) Average frequency as a function of the cophonicity. The legend is common to both plots.

Chapter 6

Effect of noninteracting intercalants on layer exfoliation in transition metal dichalcogenides

In this chapter, we present the conclusions of a second investigation on the tribological behaviour of TMDs at the nanoscale, and how it relates to the predictability of exfoliation processes. The latter correspond to the separation of the layers as a consequence of the combined action of external forces acting along the shear and vertical directions with respect to the layer plane. More specifically, in this type of situation, the external forces overcome the internal vdW forces that bind the layers together. The consequence is a relative motion of the plane of atoms, that can be a sliding motion if the resulting force component tangent to the surface is non null.

As we explained in section 4.3, phonon modes are related to these atomic motions, as any atomic displacement can be described using an appropriate linear combination of phonon eigendisplacements [134, 135]. As these eigendisplacements constitute a complete basis, the description of the atomic motions in the system is complete. There is then an equivalency between the real description of the atomic motions, using a set of Cartesian vectors, and the "mode" description. The phonon eigenvectors that represent a relative layer displacements in the direction parallel to the layer planes are naturally called "*sliding modes*".

Furthermore, another type of displacement relates to the exfoliation process. During the sliding, the overlap between the electronic densities around the atoms increases in the interlayer region. Due to the Coulomb interaction and the Pauli exclusion principle, a repulsive force emerges. When the relative motion of the layer in the direction perpendicular to the sliding plane is allowed, the resultant of the repulsive forces will push away the layers from each other. The resulting

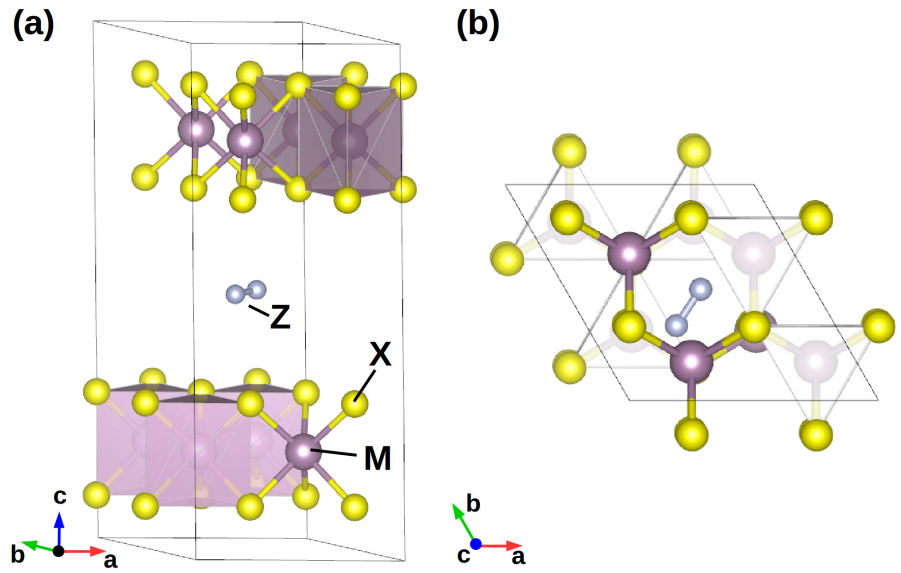

Figure 6.1: Schematic view of a Z-MX_2 model geometry; the Z molecule stands for N_2 or CO_2 molecule. It shows how the valence band width can be a suitable parameter to follow the effect of molecular intercalation of inert molecules on TMD friction properties. Each M cation coordinates six X anions via covalent bonds formes MX layers; (a) side view of the layer, the Z molecule sits in the interlayer gap and influence the van der Waals forces binding the layers together (b) top view of the plane perpendicular to the lattice vector **c**.

increasing separation will allow for an easier sliding, and then exfoliation. On the other hand, if the interlayer distance was nearly fixed as a result of the layer adhesion, the repulsive force would oppose the lateral sliding. Consequently, phonon modes that represent a relative layer displacement perpendicular to the sliding plane are related to the sliding, and called "*breathing modes*". If one wants to enhance the exfoliation of layered materials, the control of friction at the atomic scale is therefore fundamental. This work is an opportunity for the reader to better comprehend the efficiency of our method in breaking down and describing the exfoliation dynamics, scenarios commonly seen in experimental studies. It constitutes the subject of an article published in the Physical Review Applied journal [136].

Exfoliation methods based on intercalation of inert molecules have been regarded as an efficient way to reduce several layered compounds into thin sheets [137]. This study focuses on how inert molecules Z can change the tribological properties of TMD layers when intercalated in the interlayer gap (Figure 6.1). The molecule is introduced in the interlayer gap of a $2\times2\times1$ supercell of the pristine geometry. The choice for the exchange-correlation potential and the vdW correction is the same as specified in chapter 5, as well as the energy and force tolerance for the convergence. The cutoff energy for the plane wave basis is set equal to 25.7 Ha and we sample

the Brillouin zone by using a $7 \times 7 \times 5$ Monkhorst-Pack division.

As in the previous study, the first step is to observe how the general geometry of the system is impacted by the intercalation of the molecule. For fixed M and X atomic species, the **a** and **b** lattice parameters are not affected by the type of contaminant. The main variation is observed for the **c** crystallographic axis which is responsible for the increase in volume. There is no significant difference when comparing the cases with the two different molecules (Figure 6.2).

One quantity that is highlighted is the width of the valence band. Despite the fact that the valence-band width is not correlated with the geometry of the cell, the length of the lattice vectors and the system volume (Figure 6.3(a)), it decreases when the value of Z is going from 0 (i.e., the pristine structure) to N_2, and finally CO_2, independently of the chemical composition of the MX_2 layers. As a general trend, an increase of the valence-band width corresponds to higher sliding and breathing frequencies. This result suggests that narrowing the valence band would be a good way to reduce the lateral friction and the layer adhesion, and consequently allow an easier layer exfoliation.

We show that the inert intercalant molecule determines the width of the valence band, although it does not interact with the atoms of the layers. The valence-band width seems to correlate with the vibrational properties related to the intrinsic friction: small width values correspond to small interlayer binding forces, hence to reduced friction and easy layer sliding and separation. This result allow us to make predictions on the behavior of the system during a sliding event, in which the system is out of equilibrium. Such a prediction is made from the extraction of the system's properties at the equilibrium.

In order to test the efficiency of such a prediction, and the reduction of the adhesion force between the layers, it is necessary to look at the sliding barriers. For each Z–MX_2 system, a guess is built for a possible sliding path, i.e., a set of 11 geometrical configurations (Figure 6.4a), starting from the optimized geometry and considering the distortions induced by the $\Gamma(4-5)$ modes corresponding to a rigid sliding. The set of eigenvectors is chosen in a way derived from the *normal-mode transition approximation* method (NMTA), described in Ref. [42]. The path is then relaxed without any constraint on the ionic positions or the volume of the cell. To this aim, we use the CI-NEB method [121] presented in section 4.6 and implemented in the VASP software [120].

The order of magnitude of the potential energy barriers ΔE_{bar} associated to the relative layer sliding is comparable with those obtained in a previous study using

the NEB method [42]. We then define the average friction force as

$$\Delta f_{fr} = \frac{\Delta E_{bar}}{\Delta R_{NEB}} \tag{6.1}$$

where ΔE_{bar} is the difference between the energy of ground state and the maximum energy value realized along the path; ΔR_{NEB} measures the displacement of the atoms during the sliding:

$$\Delta R_{NEB} = \sqrt{\sum_{\kappa=1}^{N} \mathbf{R}_{bar}^{\kappa} - \mathbf{R}_{0}^{\kappa}}, \tag{6.2}$$

where $\mathbf{R}_0^\kappa$ represents the position of the κ-th atom in the configuration corresponding to equilibrium geometry and $\mathbf{R}_{bar}^\kappa$ the position of the same atom in the maximum energy configuration.

In a similar way, we estimate the adhesion force. As in the previous step, we consider a new set of geometric configurations, starting from the equilibrium geometry. This time, the geometric configurations correspond to the situation where the distance between the two layers is progressively increased along the c-axis direction as shown in Figure 6.4(b). For each configuration, we fix the lattice parameters and the positions of the M cations, and optimize the coordinates of the remaining atoms. By following the evolution of the system energy as a function of the interlayer distance, we observe an asymptotic behaviour. This ensures that the last configuration corresponds to non-interacting (separated) layers. Analogously as for f_{fr}, we can define the average adhesion force f_{ad} as

$$f_{ad} = \frac{\Delta E_{sep}}{\Delta R_{sep}} \tag{6.3}$$

where ΔE_{sep} is the difference between the energy of the ground state and the last configuration, while ΔR_{sep} corresponds to the interlayer distance. We see that, in a way similar to what is observed for the sliding and breathing frequencies, large values of the frictional and adhesion forces correspond to large values of the band width (Figure 6.5).

Finally, since both lateral friction and adhesion forces appear during the exfoliation process, considering an average force $f_{ave} = \frac{f_{fr}+f_{ad}}{2}$ is a natural choice to quantify the force resisting the exfoliation; analogously, we consider the average frequency $\omega_{ave} = \frac{(\omega_{sl}+\omega_{br})}{2}$. In general, both quantities increase with the value of the valence-band width Figure 6.6.

According to these results, we believe that the valence-band width is a useful

descriptor to parameterize the forces opposing the layer exfoliation in the presence of inert intercalated molecules. Future studies, in which the presented analysis method is applied on more inert species and geometries, should be considered in order to further confirm these conclusions.

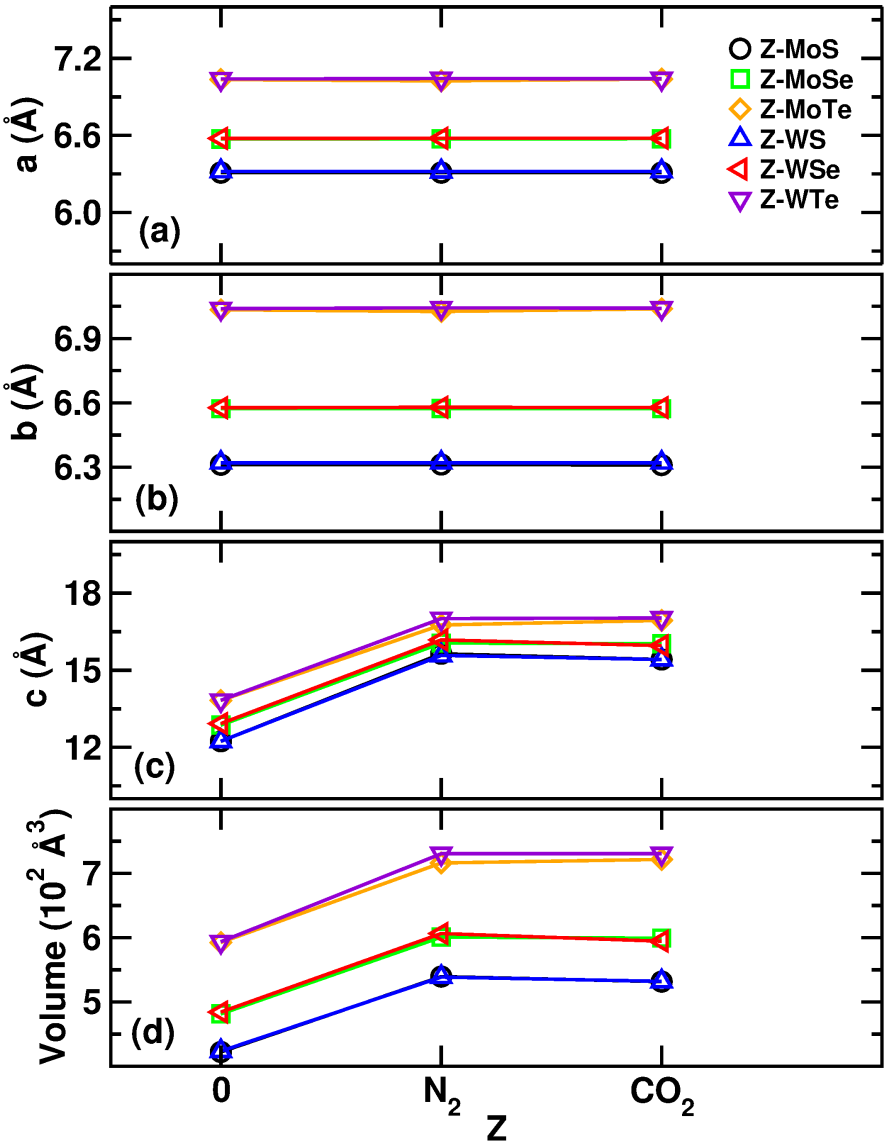

Figure 6.2: Length of the lattice vectors and volume of the unit cell for each type of contaminant molecule in the interlayer gap. For a given Z, the values relative to systems with the same X anion are very close and the corresponding data points almost overlap in all the plots. Legend is common to all the subfigures.

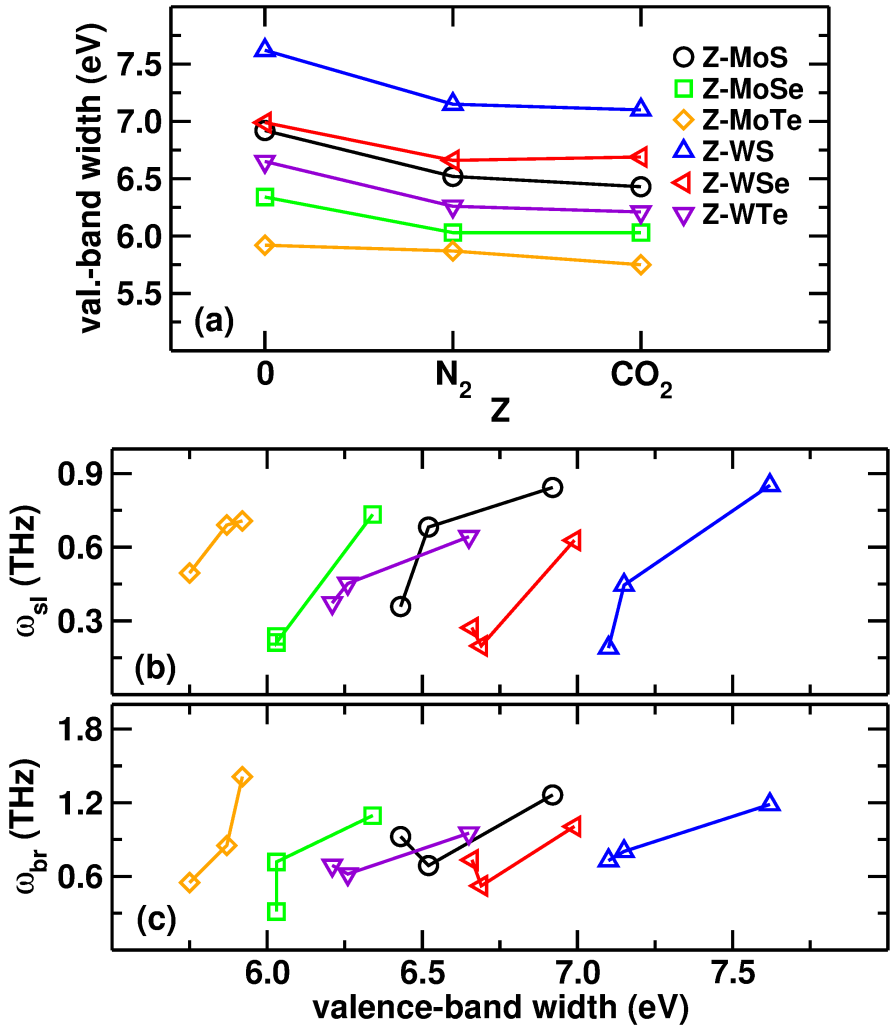

Figure 6.3: (a) Width of the valence band as a function of the intercalated molecule Z. Average frequencies of the sliding (b) and breathing modes (c) as a function of the width of the valence band. Legend is common to the 3 subfigures.

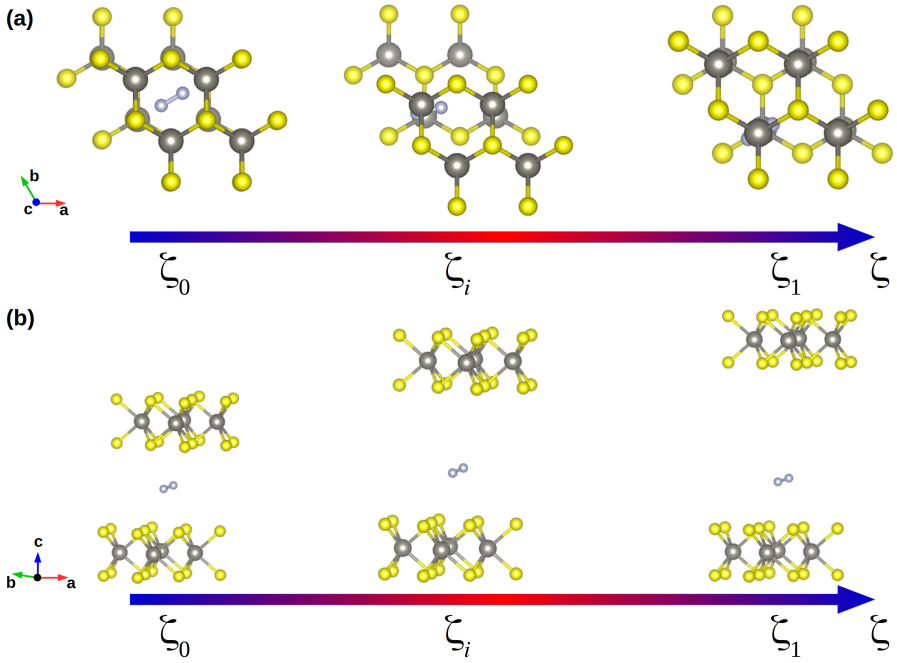

Figure 6.4: Illustration of the set of geometrical images chosen for the sliding (a) and layer separation (b) paths. ζ_0, ζ_i and ζ_1, are used to indicate the initial, an intermediate and the final states respectively, along the configurational coordinate ζ.

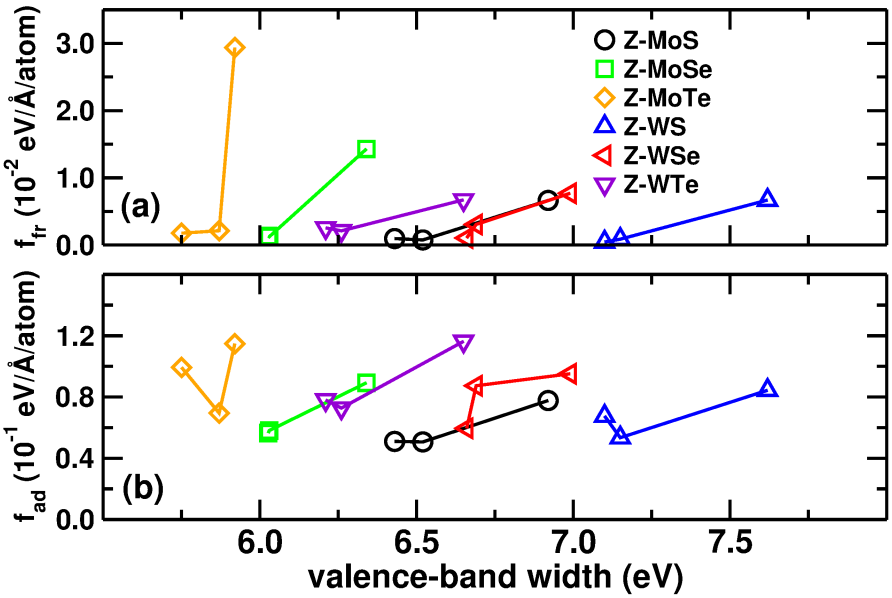

Figure 6.5: (a) Lateral frictional force and (b) adhesion force as a function of the width of the valence band. Both forces display large values in correspondence with large values of the band width.

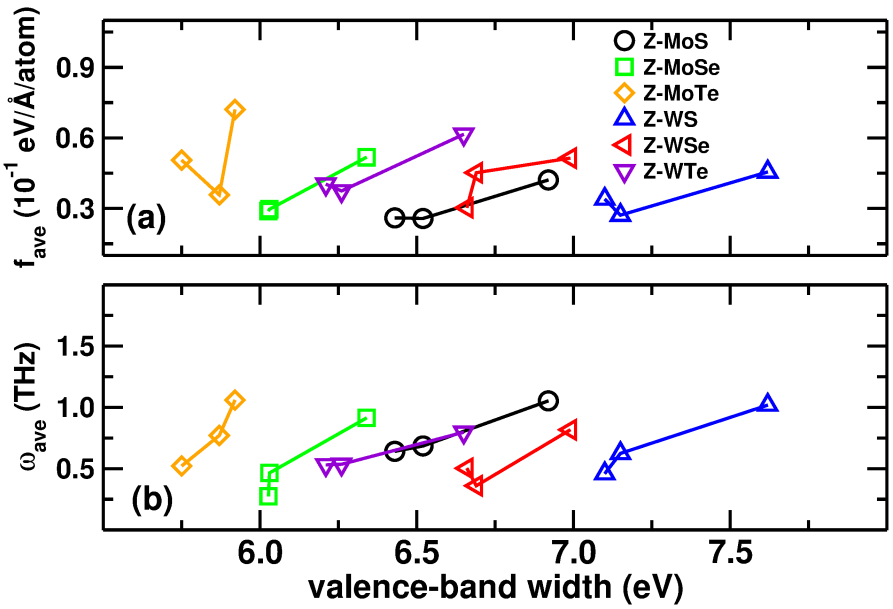

Figure 6.6: (a) Average force and (b) average mode frequency as a function of the width of the valence band. In general, we see an increase of the values when the band width increases. Legend is common to all the subfigures.

Chapter 7

Effect of the simultaneous use of contaminant and electrostatic fields on the nanoscale friction in transition metal dichalcogenides

This work was made in collaboration with the VASP team of Vienna university, who are implementing the force calculation within the PAW formalism and in the presence of an electric field; in this collaboration, we provided this case study. It intends to show how the simultaneous use of electric field and proper choice of contaminant molecules can lower the intrinsic friction.

We build our geometric models starting from the hexagonal $P6_3/mmc$ crystalline MX_2 compounds as reference structures, and choosing M=Mo, W and X=S, Se, Te as before. We consider $2\times2\times1$ supercells and introduce one N_2 molecule in the interlayer gap (Figure 7.1). The choice of N_2 is made considering that it is the most abundant molecule in ordinary tribological working conditions. The introduction of the N_2 molecule reduces the symmetries of the reference structures, as specified in the previous chapter; in fact, all the model geometries present the symmetries of the triclinic $P1$ space group. The DFT calculations are performed using the Perdew-Burke-Ernzerhof (PBE) energy functional used before [131], and implemented in the VASP software. The Van der Waals interactions are taken into account by using the Grimme correction [87]. We sample the Brillouin zone with a minimum of a $3\times3\times3$ k-point mesh with a plane wave cutoff of 500 eV. We use the diffraction data specified in chapter 5 to initiate atomic and lattice structural relaxations, while the forces are minimized using a 0.5 meV $Å^{-1}$ tolerance.

The analysis starts again by the geometric features of the systems. We notice

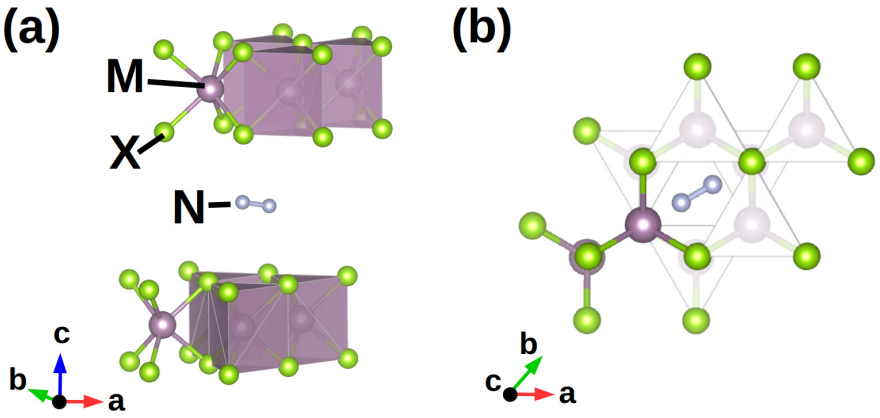

Figure 7.1: (a) lateral and (b) c-axis view of the model structure of MX_2 TMD compounds with an N_2 molecule, inserted as an impurity.

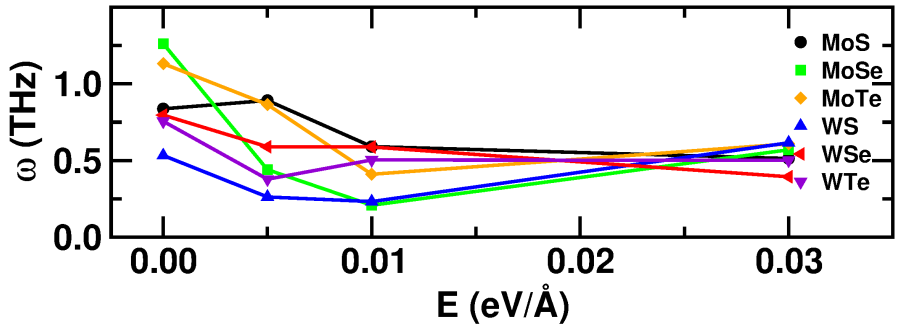

Figure 7.2: Average frequency ω as a function of the applied electric field E.

that the presence of the N_2 molecule in the interlayer region does not affect the topology of the system. The isotropy of the inner electronic environment between the layers is preserved; consequently the response of the system along the **a** and **b** lattice directions is homogeneous (Figure 7.3(a-b)), which is coherent with what was observed in the first study, since the field is also applied along the c axis. Along this direction, the crystal is more sensitive to the field variation (Figure 7.3(c)), resulting in an increase of the cell volume as shown in Figure 7.3(d).

When looking into the average frequency ω, we first observe that the frequencies of the sliding-related modes generally decrease for $E \leq 0.01$ eV/Å^{-1}, when the field is switched on (Figure 7.2). The variation range of ω depends mostly on the chemical composition. The average frequency of the N_2–WTe_2 system is less sensitive to the intensity variation of the field; the opposite holds for the N_2–$MoSe_2$ and N_2–$MoTe_2$ systems. The change in the cell volume can be partially responsible for the change of the phonon frequencies [134], but there is no direct relation between the average frequency ω and the lattice parameters.

The frequency ω is determined by the atomic types and the interatomic in-

teractions within the crystal, which settle the dynamic features and the electronic density. To understand the subtle connection between ω and the interatomic effects, it is necessary to look extensively into the electronic distribution and its relation to the phonon behaviour. As before, we compare the variations of the different polarizations as a function of E; this gives us the preferential distribution of the electrons as a function of the field. By selecting the same set of orbitals as in the previous studies described in chapter 5 and chapter 6, we observe the same low sensitivity of $\mathcal{P}_{p_x,p_y}$ to the field (Figure 7.4(a)). This, again, accounts for the symmetry of the system response along the directions parallel to the a, b plane. At fixed M and X species, $\mathcal{P}_{p_x,p_z}$ and $\mathcal{P}_{p_y,p_z}$ have similar values, and the N_2–WTe_2 system is the one displaying the less variation. The negative values of $\mathcal{P}_{p_x,p_z}$ and $\mathcal{P}_{p_y,p_z}$ indicate an excess of charge along an axis orthogonal to the layer plane and passing through the anionic sites (Figure 7.4(b-c)). However, the variation at $E \neq 0$ is small sitting at about 1%. When looking at the region around the cations, we see that the P_{t_{2g},e_g} orbital polarization is more sensitive to the field than $P_{d_{x^2-y^2},d_{z^2}}$. The positive value of P_{t_{2g},e_g} indicates an excess of electron charge off the c-axis (Figure 7.4(d-e)). At the M cation, there is no accumulation of charge along an axis parallel to the field. Globally, the field effect on the relative occupation of the orbitals is weak. This response is different than what we observed in the same pristine systems without any contaminants (chapter 5). The main indication from this different outcome is that the molecule stabilizes the inner electronic distribution of the layers, and makes it less sensitive to the variations of the field.

Despite the fact that the field does not significantly affect the electronic distribution, yet there are still some changes in the sliding-related frequencies. The relative occupation of t_{2g} against e_{2g} affects the sliding-related frequencies in various ways, depending on the atomic type of the cation. When the field is switched on, low ω frequencies are reached at critical values of P_{t_{2g},e_g} in the N_2–MoX_2 systems (Figure 7.5(a)); in the N_2–WX_2 systems instead, the low values correspond to an overpopulation of the e_g orbital compared to the t_{2g} (Figure 7.5(b)). The information obtained with the orbital polarization analysis is incomplete in the sense that we don't know how it translates into changes of the nature of the M-X bonds.

We provide the analysis of the bond covalency $C_{M,X}$ calculated in terms of atomic contributions to the density of states (section 4.1). The small variations of the orbital polarizations do not have a significant impact on the covalent character of the bond, which is nearly constant with the field. Despite that, such small variations induce a different relation between ω and $C_{M,X}$ depending on the atomic type of the cation. Interestingly, at small field values, low ω frequencies are realized

at low covalency values in the N_2–MoX_2 systems, as we see in Figure 7.5(c). This corresponds to a more ionic Mo-X bond character; for the N_2–WX_2 systems, we observe an opposite behaviour (Figure 7.5(d)).

The pieces of information gathered so far can be condensed as such: the external variation of the applied electric field induces subtle perturbations to the electronic distribution. Such modification changes the interatomic forces which, in turn, determine the final values of the phonon frequencies and the associated displacements, as they intervene in the definition of the dynamical matrix (subsection 4.2.1). The electronic and dynamical features are then coupled together by non-trivial relations.

The cophonicity metric descriptor (subsection 4.2.3) is the tool that allows us to parameterize such coupling. We observe that the cophonicity is nearly constant with the field at a constant chemical composition (Figure 7.6(a)), unlike what we found in the pristine systems without contaminants in chapter 5. This means that the molecule also stabilizes the dynamic features of the system against the field perturbation. In detail, the small perturbations induced by the field into the electronic distribution affect the atomic participation to only few sliding-related phonon bands. This is highlighted when we consider how the cophonicity varies with the P_{t_{2g},e_g} orbital polarization (Figure 7.6(b-c)): in general, the larger the charge unbalance between the t_{2g} and e_g orbitals, the larger the anion contribution to the sliding motion. This means that the charge redistribution induced by the field gives rise to *an effective ionic mass*, which is in general different to than the one of the unperturbed system, and changes with the value of the field.

The impact of this effective mass on the overall atomic displacement pattern is now analysed. We consider the atomic participation to the phonon band dispersion along the linear path Γ-A in the irreducible Brillouin zone. At each $\mathbf{q}$-point along the path, the atomic character of the j-th band is defined according to the components of the $\mathbf{e}_{\mathbf{q},j}$ eigenvector. For example, a $(\mathbf{q}, j)$ phonon mode is of M-character if the largest $\mathbf{e}_{\mathbf{q},j}$ eigenvector components are those corresponding to the M atoms. For instance, in the N_2–MoSe system, the general character of the sliding-related modes is of mixed Mo- and Se-kind at small fields, while the Mo-character becomes predominant at $E = 0.03$ eV/Å (Figure 7.7(a-d)). Looking at the N_2–WSe_2 system, we observe that the bands at about 1 THz show a Se-character at $E = 0.0$ and 0.03 eV/Å^{-1}, while for intermediate fields both ions contribute in a similar way (Figure 7.7(e-h)).

By studying the combined effect of an electrostatic field and the presence of a small inert molecule as a contaminant on the nanoscale frictional properties in TMDs, we showed that the insertion of N_2 molecules in the interlayer region stabi-

lizes the nanotribological response of the system against the perturbations induced by an applied electrostatic field. The present results constitute a starting point: future studies involving different kinds of contaminants and relative concentrations, along with different field orientations, will be necessary in order to design new tribological materials with a tuned frictional response.

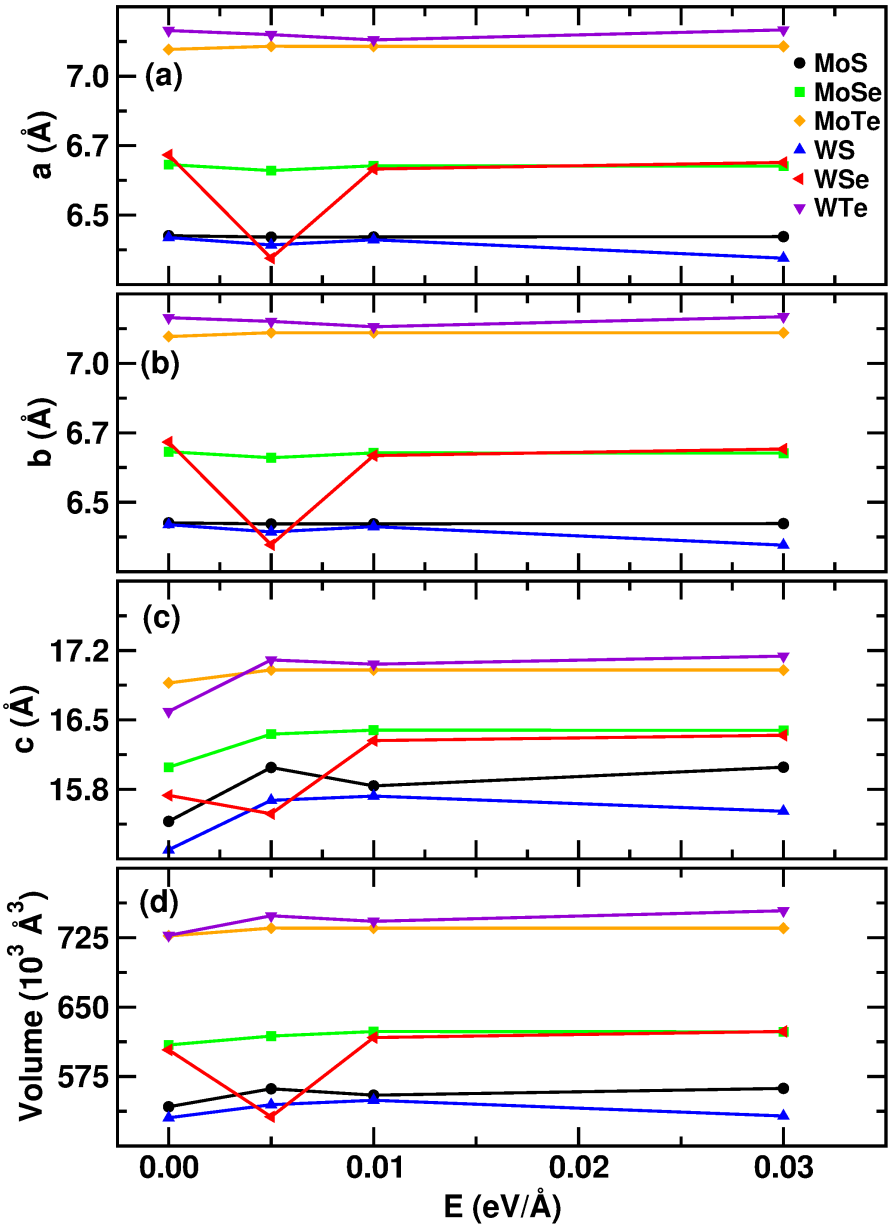

Figure 7.3: Geometric parameters of the unit cell of all the N_2–MX_2 systems as a function of the applied field E.

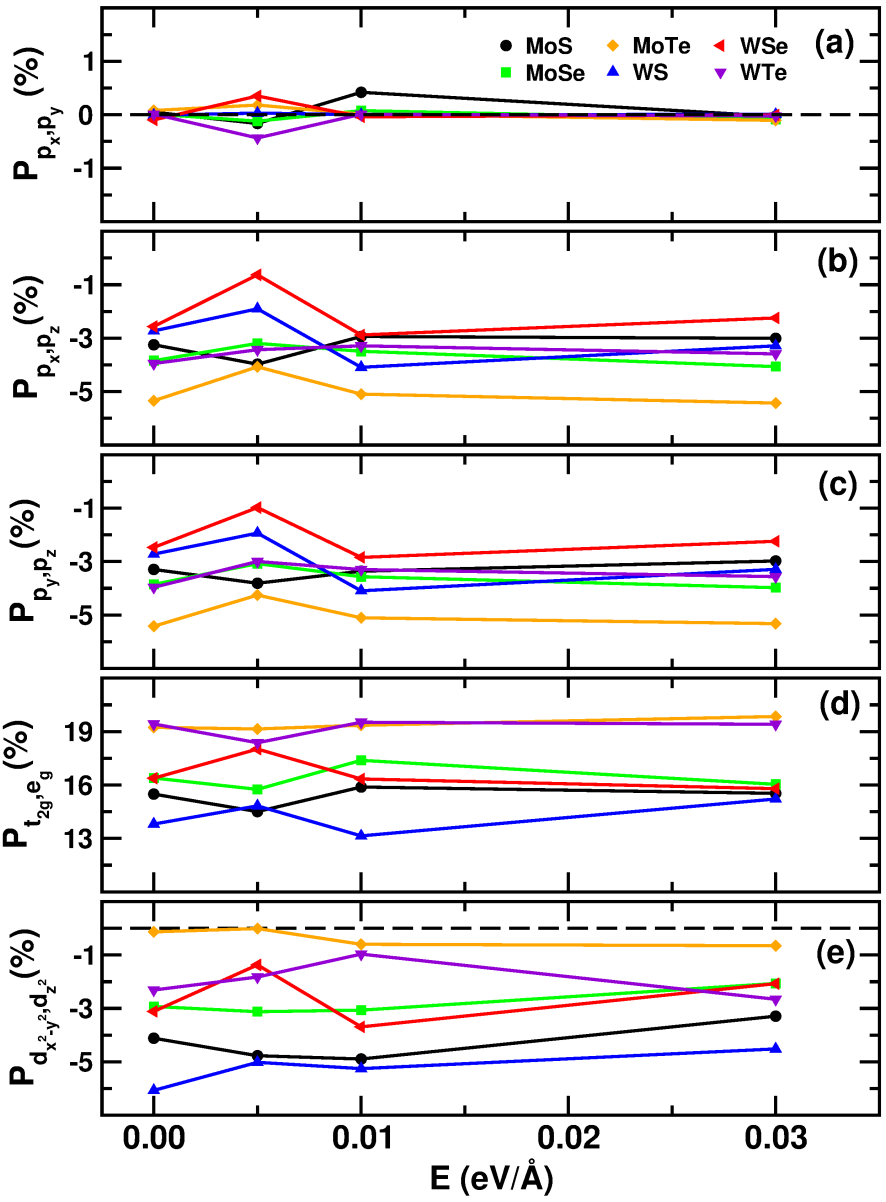

Figure 7.4: Orbital polarization of all the systems in the range of considered electric field values.

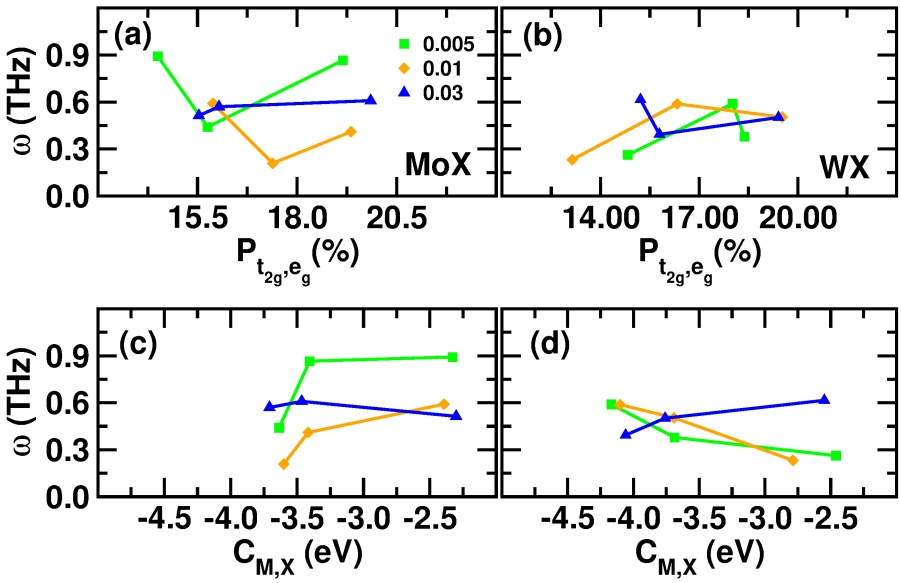

Figure 7.5: Relation between the average frequency and (a-b) the orbital polarization P_{t_{2g},e_g}, and (c-d) the M–X bond covalency for N_2–MoX_2 (left panels) and N_2–WX_2 systems (right panels). Field values are reported in the legend, common to all the plots.

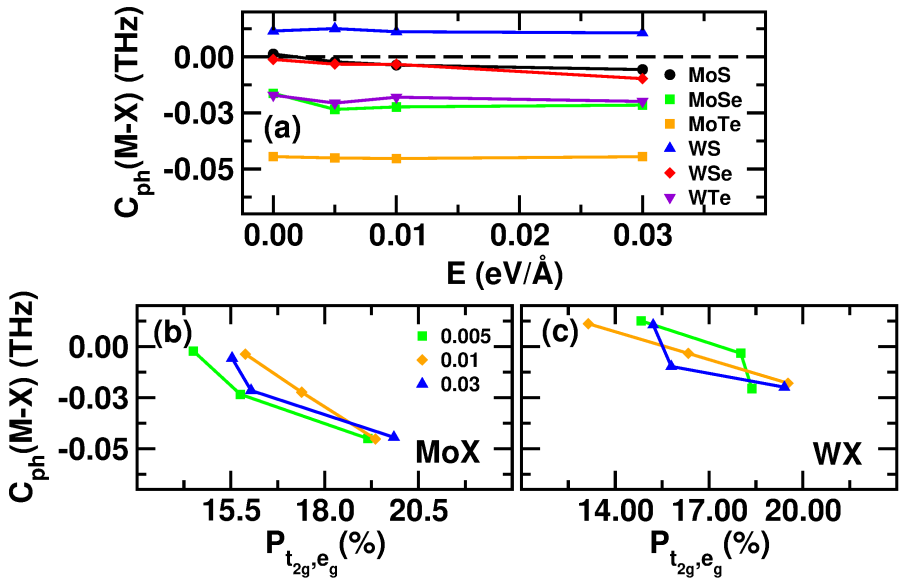

Figure 7.6: (a) M-X pair cophonicity calculated for each N_2–MX_2 model as a function of the electric field E. (b-c) Cophonicity as a function of the P_{t_{2g},e_g} orbital polarization in N_2–MoX_2 and N_2–WX_2 systems; field values are reported in the legend.

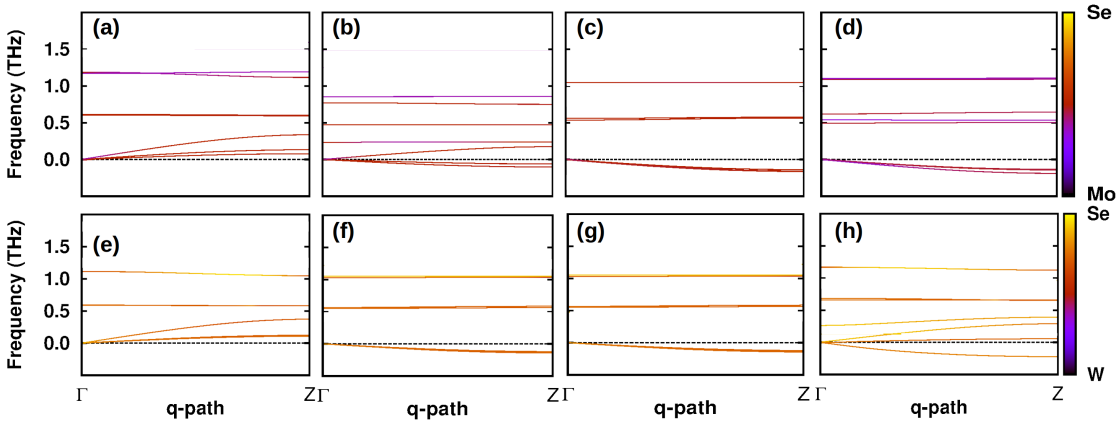

Figure 7.7: Atomic character of the phonon band dispersion along the $\Gamma - A$ linear path in the irreducible Brillouin zone for the N_2–$MoSe_2$ (top) and N_2–WSe_2 (bottom) systems for $E = 0.0$ (a, e) , 0.005 (b, f), 0.01 (c, g) and 0.03 (d, h) eV/Å^{-1}, respectively. The field magnitude modifies the effective mass of the ions, hence the character of the sliding-related phonon bands.

Chapter 8

Conclusions

Throughout this thesis, we investigated the frictional properties of lamellar materials at the nanoscale. For this aim, we considered six transition metal dichalcogenides prototypes as a case study.

We first simulated the effect of an electrostatic field on the nanoscale frictional properties. We showed that the application of an electrostatic field along an axis orthogonal to the atom layers induces a transfer of charge along the same axis; this transfer does not affect significantly the covalent character of the bond, but it modifies the interatomic forces. The consequence of this modification is the softening of the sliding modes, until the systems become unstable when the field reaches a critical value, specific to the chemical composition. The cophonicity metric shows that large differences between the cation and anion velocities lead to strongly unstable phonon modes, and a lower intrinsic friction.

We then contributed to a second study of the nanotribological response of the very same materials under the introduction of inert contaminants in the interlayer environment. This work showed that the inert intercalant molecule determines the width of the valence band. The valence-band width seems to correlate with the vibrational properties related to the intrinsic friction: small width values correspond to small interlayer binding forces, and consequently to reduced friction and easy layer sliding and separation. Similar correlation is found with the friction and the adhesion forces: the larger the valence band width, the larger the forces. Since such forces arise during the exfoliation process, such results then suggest that a suitable tuning of the value of the band width may be one way to assist the exfoliation in similar systems. The presented analysis protocol can be used in systematic studies on the frictional response in the presence of inert intercalated species. This would help to define the potentiality and the limitations of the valence-band width as a friction indicator.

We finally studied the combined effect of an electrostatic field and a contaminant to the layer sliding. We showed that the insertion of N_2 molecules in the interlayer region stabilizes the response of the system against the perturbations induced by the application of an electrostatic field.

The lowest values of the field are compatible with those already used in experimental studies of similar materials, and can be used to constraint future experiments [138]. These conclusions represent a theoretical procedure for future investigations aiming to parameterize the triboresponse of 2D materials to electric fields. It is also a starting point for further studies where different directions of the field other than that orthogonal to the atomic layers are considered. More generally, the present study can be used to predict the preferential electronic redistribution in nanomechanical devices. This may help to understand how to avoid or use metal-to-insulator transitions within the material during working conditions [139], as well as how to act to locally optimize the electric transport.

The results obtained by comparing different chemical compositions, geometries and directions of the applied electric field can be used to suggest how to select proper fields and contaminants to design new tribological materials with a customized frictional response. Such a study is already planned by taking into consideration bilayer heterostructures, and will allow to predict behavior and control parameters useful for thin films manipulation.

Finally, our methodology could be extended to consider the effect of finite temperatures, and used in the aim to control the friction between nanocontacts (typically a tip against a surface). In fact, in a dry environment, thermal vibrations can increase the friction; it was shown that, in this case, the friction can be reduced by enforcing the mechanical resonances of the sliding system perpendicular to the contact plane [140]. By selecting in detail the modes to enforce, our method could be used in this type of stick-slip motion studies.

List of publications

- **F. Belviso** et al., Viewpoint: Atomic-Scale Design Protocols toward Energy, Electronic, Catalysis, and Sensing Applications, *Inorg. Chem.* **58**, 14939, (2019)
- **F. Belviso**, A. Cammarata, J. Missaoui, T. Polcar, Effect of electric fields in low-dimensional materials: Nanofrictional response as a case study, *Phys. Rev. B* **102**, 155433, (2020)
- J. Missaoui, A. Cammarata, **F. Belviso**, T. Polcar, Effect of Noninteracting Intercalants on Layer Exfoliation in Transition-Metal Dichalcogenides, *Phys. Rev. Appl.* **15**, 064041 (2021)

Bibliography

[1] K. S. Novoselov et al. "Electric Field Effect in Atomically Thin Carbon Films". In: *Science* 306.5696 (2004), pp. 666–669. ISSN: 0036-8075. DOI: 10.1126/science.1102896.

[2] A. K. Geim and I. V. Grigorieva. "Van der Waals heterostructures". In: *Nature* 499.7459 (July 2013), pp. 419–425. ISSN: 1476-4687. DOI: 10.1038/nature12385.

[3] B. Yu et al. "High-power triboelectric nanogenerator prepared from electrospun mats with spongy parenchyma-like structure". In: *Nano Energy* 34 (2017), pp. 69–75. ISSN: 2211-2855. DOI: 10.1016/j.nanoen.2017.02.010.

[4] C. Lee et al. "Measurement of the Elastic Properties and Intrinsic Strength of Monolayer Graphene". In: *Science* 321.5887 (2008), pp. 385–388. ISSN: 0036-8075. DOI: 10.1126/science.1157996.

[5] X. Zhao et al. "Enhanced mechanical properties of graphene-based poly (vinyl alcohol) composites". In: *Macromolecules* 43.5 (2010), pp. 2357–2363. DOI: 10.1021/ma902862u.

[6] F. Chianese et al. "Linear conduction in N-type organic field effect transistors with nanometric channel lengths and graphene as electrodes". In: *Applied Physics Letters* 112.21 (2018), p. 213301. DOI: 10.1063/1.5023659.

[7] P. Vogt et al. "Synthesis and electrical conductivity of multilayer silicene". In: *Applied Physics Letters* 104.2 (2014), p. 021602. DOI: 10.1063/1.4861857.

[8] H. Liu et al. "The Effect of Dielectric Capping on Few-Layer Phosphorene Transistors: Tuning the Schottky Barrier Heights". In: *IEEE Electron Device Letters* 35.7 (2014), pp. 795–797. DOI: 10.1109/LED.2014.2323951.

[9] N. R. Glavin et al. "Emerging Applications of Elemental 2D Materials". In: *Advanced Materials* 32.7 (2020), p. 1904302. DOI: 10.1002/adma.201904302.

[10] N. Mounet et al. "Two-dimensional materials from high-throughput computational exfoliation of experimentally known compounds". In: *Nature Nanotechnology* 13.3 (Feb. 2018), pp. 246–252. ISSN: 1748-3395. DOI: 10.1038/s41565-017-0035-5.

[11] M. Mojtabavi et al. "Single-Molecule Sensing Using Nanopores in Two-Dimensional Transition Metal Carbide (MXene) Membranes". In: *ACS Nano* 13.3 (2019). PMID: 30844249, pp. 3042–3053. DOI: 10.1021/acsnano.8b08017.

[12] S. Zang et al. "Tribology of two-dimensional materials: From mechanisms to modulating strategies". In: *Materials Today* 26 (2019), pp. 67–86. ISSN: 1369-7021. DOI: 10.1016/j.mattod.2018.12.002.

[13] J. H. Lee et al. "Nanotribology of 2D materials and their macroscopic applications". In: *Journal of Physics D: Applied Physics* 53.39 (July 2020), p. 393001. DOI: 10.1088/1361-6463/ab9670.

[14] K. Holmberg and A. Erdemir. "Influence of tribology on global energy consumption, costs and emissions". In: *Friction* 5 (Sept. 2017), pp. 263–284. DOI: 10.1007/s40544-017-0183-5.

[15] G.W. Stachowiak and A.W. Batchelor, eds. *1 Introduction*. Vol. 24. Tribology Series. Elsevier, 1993, pp. 1–9. DOI: 10.1016/S0167-8922(08)70575-3.

[16] E. W. Roberts. "Space tribology: its role in spacecraft mechanisms". In: *Journal of Physics D: Applied Physics* 45.50 (Nov. 2012), p. 503001. DOI: 10.1088/0022-3727/45/50/503001.

[17] S. Mahathanabodee et al. "Effects of hexagonal boron nitride and sintering temperature on mechanical and tribological properties of SS316L h-BN composites". In: *Materials and Design* 46 (2013), pp. 588–597. ISSN: 0261-3069. DOI: 10.1016/j.matdes.2012.11.038.

[18] J. Meyer, R. Bischoff, and G. Feltrin. "Microelectromechanical Systems (MEMS)". In: *Encyclopedia of Structural Health Monitoring*. American Cancer Society, 2009. ISBN: 9780470061626. DOI: 10.1002/9780470061626.shm123.

[19] M. Lemme et al. "Nanoelectromechanical sensors based on suspended 2D materials". In: *Research* 2020 (2020).

[20] R. F. Frindt. "Single Crystals of MoS_2 Several Molecular Layers Thick". In: *Journal of Applied Physics* 37.4 (1966), pp. 1928–1929. DOI: 10.1063/1.1708627.

[21] P. Joensen, R.F. Frindt, and S.Roy Morrison. "Single-layer MoS_2". In: *Materials Research Bulletin* 21.4 (1986), pp. 457–461. ISSN: 0025-5408. DOI: 10.1016/0025-5408(86)90011-5.

[22] Z. Zeng et al. "Single-Layer Semiconducting Nanosheets: High-Yield Preparation and Device Fabrication". In: *Angewandte Chemie International Edition* 50.47 (2011), pp. 11093–11097. DOI: 10.1002/anie.201106004.

[23] He Tian et al. "Low-symmetry two-dimensional materials for electronic and photonic applications". In: *Nano Today* 11.6 (2016), p. 763. ISSN: 1748-0132. DOI: 10.1016/j.nantod.2016.10.003.

[24] Anupama B. Kaul. "Two-dimensional layered materials: Structure, properties, and prospects for device applications". In: *J. Mater. Res.* 29.3 (2014), p. 348. DOI: 10.1557/jmr.2014.6.

[25] Hai Li et al. "Preparation and Applications of Mechanically Exfoliated Single-Layer and Multilayer MoS_2 and WSe_2 Nanosheets". In: *Accounts Chem. Res.* 47.4 (2014), p. 1067. DOI: 10.1021/ar4002312.

[26] Manish Chhowalla et al. "The chemistry of two-dimensional layered transition metal dichalcogenide nanosheets". In: *Nat. Chem.* 5.4 (2013), p. 263. ISSN: 1755-4330. DOI: 10.1038/nchem.1589.

[27] A. K. Geim and I. V. Grigorieva. "Van der Waals heterostructures". In: *Nature* 499.7459 (2013), p. 419. ISSN: 0028-0836. DOI: 10.1038/nature12385.

[28] Andrea Vanossi et al. "*Colloquium* : Modeling friction: From nanoscale to mesoscale". In: *Rev. Mod. Phys.* 85 (2 2013), p. 529. DOI: 10.1103/RevModPhys.85.529.

[29] Henrik G. Füchtbauer et al. "Morphology and atomic-scale structure of single-layer WS_2 nanoclusters". In: *Phys. Chem. Chem. Phys.* 15.38 (2013), p. 15971. DOI: 10.1039/c3cp51758f.

[30] S. Helveg et al. "Atomic-Scale Structure of Single-Layer MoS_2 Nanoclusters". In: *Phys. Rev. Lett.* 84.5 (2000), p. 951. DOI: 10.1103/physrevlett.84.951.

[31] L. Wugang et al. "Van der Waals heterostructures for optoelectronics: Progress and prospects". In: *Applied Materials Today* 16 (2019), pp. 435–455. ISSN: 2352-9407. DOI: 10.1016/j.apmt.2019.07.004.

[32] M. R. Vazirisereshk et al. "Nanoscale Friction Behavior of Transition-Metal Dichalcogenides: Role of the Chalcogenide". In: *ACS Nano* 14.11 (2020). PMID: 33090766, pp. 16013–16021. DOI: 10.1021/acsnano.0c07558.

[33] F. He et al. “In-Plane Potential Gradient Induces Low Frictional Energy Dissipation during the Stick-Slip Sliding on the Surfaces of 2D Materials”. In: *Small* 15.49 (2019), p. 1904613. DOI: 10.1002/smll.201904613.

[34] V. E. P. Claerbout, T. Polcar, and P. Nicolini. “Superlubricity achieved for commensurate sliding: MoS_2 frictional anisotropy in silico”. In: *Computational Materials Science* 163 (2019), pp. 17–23. ISSN: 0927-0256. DOI: 10.1016/j.commatsci.2019.03.019.

[35] P. Nicolini et al. “Structural Ordering of Molybdenum Disulfide Studied via Reactive Molecular Dynamics Simulations”. In: *ACS Applied Materials and Interfaces* 10.10 (2018). PMID: 29460632, pp. 8937–8946. DOI: 10.1021/acsami.7b17960.

[36] A. Cammarata and T. Polcar. “Electro-vibrational coupling effects on "intrinsic friction" in transition metal dichalcogenides”. In: *RSC Adv.* 5.129 (2015), p. 106809. DOI: 10.1039/C5RA24837J.

[37] A. Cammarata and T. Polcar. “Layering effects on low frequency modes in n-layered MX_2 transition metal dichalcogenides”. In: *Phys. Chem. Phys.* 18.6 (2016), p. 4807. DOI: 10.1039/C5CP06788J.

[38] E. Serpini et al. “Nanoscale frictional properties of ordered and disordered MoS_2”. In: *Tribology International* 136 (2019), pp. 67–74. ISSN: 0301-679X. DOI: 10.1016/j.triboint.2019.03.004.

[39] H. Wang, C. C. Huang, and T. Polcar. “Controllable Tunneling Triboelectrification of Two-Dimensional Chemical Vapor Deposited MoS_2”. In: *Scientific reports* 9.1 (2019), pp. 1–8.

[40] A. Cammarata. “Phonon-phonon scattering selection rules and control: an application to nanofriction and thermal transport”. In: *RSC Adv.* 9 (64 2019), pp. 37491–37496. DOI: 10.1039/C9RA08294H.

[41] G. Levita et al. “Sliding Properties of MoS_2 Layers: Load and Interlayer Orientation Effects”. In: *The Journal of Physical Chemistry C* 118.25 (2014), pp. 13809–13816. DOI: 10.1021/jp4098099.

[42] A. Cammarata and T. Polcar. “Vibrational contributions to intrinsic friction in charged transition metal dichalcogenides”. In: *Nanoscale* 9.32 (2017), p. 11488. DOI: 10.1039/C7NR04034B.

[43] C. Wang et al. “Effects of vdW Interaction and Electric Field on Friction in MoS_2”. In: *Tribology Letters* 59 (July 2015). DOI: 10.1007/s11249-015-0531-4.

[44] Q. Liu et al. "Tuning Electronic Structure of Bilayer MoS_2 by Vertical Electric Field: A First-Principles Investigation". In: *The Journal of Physical Chemistry C* 116.40 (2012), pp. 21556–21562. DOI: 10.1021/jp307124d.

[45] R. Rani et al. "Impact of transverse and vertical gate electric field on vibrational and electronic properties of MoS_2". In: *Journal of Applied Physics* 127.14 (2020), p. 145101. DOI: 10.1063/1.5131845.

[46] A. Socoliuc et al. "Atomic-Scale Control of Friction by Actuation of Nanometer-Sized Contacts". In: *Science* 313.5784 (2006), pp. 207–210. ISSN: 0036-8075. DOI: 10.1126/science.1125874.

[47] J. P. Oviedo et al. "In Situ TEM Characterization of Shear-Stress-Induced Interlayer Sliding in the Cross Section View of Molybdenum Disulfide". In: *ACS Nano* 9.2 (2015). PMID: 25494557, pp. 1543–1551. DOI: 10.1021/nn506052d.

[48] A.I. Vakis et al. "Modeling and simulation in tribology across scales: An overview". In: *Tribology International* 125 (2018), pp. 169–199. ISSN: 0301-679X. DOI: 10.1016/j.triboint.2018.02.005.

[49] L. Tobiska. "Johnson, C., Numerical Solution of Partial Differential Equations by the Finite Element Method. Cambridge etc., Cambridge University Press 1988. 279 pp., £ 17.50 P/b ISBN 0-521-34758-0". In: *ZAMM - Journal of Applied Mathematics and Mechanics / Zeitschrift für Angewandte Mathematik und Mechanik* 71.10 (1991), pp. 390–390. DOI: 10.1002/zamm.19910711004.

[50] Boris Grigoryevich Galerkin. "Series solution of some problems of elastic equilibrium of rods and plates". In: *Vestnik inzhenerov i tekhnikov* 19.7 (1915), pp. 897–908.

[51] D. J N Reddy. *An Introduction to the Finite Element Method*. McGraw-Hill Education, 2005. ISBN: 9780072466850.

[52] Z. Chen et al. "Investigation of the tribological behavior of chromium aluminum silicon nitride coatings via both scratch sliding test and FEM simulation". In: *AIP Advances* 9.2 (2019), p. 025116. DOI: 10.1063/1.5085373.

[53] M. Kubica, W. Skoneczny, and D. Jedrzejczyk. "Application of finite element method to analysis of tribological properties of aluminum oxide nanolayers". In: *Proceedings of the Institution of Mechanical Engineers, Part J: Journal of Engineering Tribology* 227.8 (2013), pp. 861–867. DOI: 10.1177/1350650112473221.

[54] B. J. Alder and T. E. Wainwright. "Studies in Molecular Dynamics. I. General Method". In: *The Journal of Chemical Physics* 31.2 (1959), pp. 459–466. DOI: 10.1063/1.1730376.

[55] S. Vemparala et al. "Large-scale molecular dynamics simulations of alkanethiol self-assembled monolayers". In: *The Journal of chemical physics* 121.9 (2004), pp. 4323–4330.

[56] M. Geshi, T. Hoshi, and T. Fujiwara. "Million-Atom Molecular Dynamics Simulation by Order-N Electronic Structure Theory and Parallel Computation". In: *Journal of the Physical Society of Japan* 72.11 (2003), pp. 2880–2885. DOI: 10.1143/JPSJ.72.2880.

[57] J. C. Phillips et al. "Scalable molecular dynamics with NAMD". In: *Journal of computational chemistry* 26.16 (2005), pp. 1781–1802.

[58] S. Plimpton. "Fast parallel algorithms for short-range molecular dynamics". In: *Journal of computational physics* 117.1 (1995), pp. 1–19.

[59] J.C Phillips et al. "Mapping to irregular torus topologies and other techniques for petascale biomolecular simulation". In: *SC'14: Proceedings of the International Conference for High Performance Computing, Networking, Storage and Analysis*. IEEE. 2014, pp. 81–91.

[60] P. Nicolini and T. Polcar. "A comparison of empirical potentials for sliding simulations of MoS_2". In: *Computational Materials Science* 115 (Apr. 2016), pp. 158–169.

[61] D. Frenkel and B. Smit. *Understanding Molecular Simulation*. 2nd. USA: Academic Press, Inc., 2001. ISBN: 0122673514.

[62] D. R. Hartree. "The Wave Mechanics of an Atom with a Non-Coulomb Central Field. Part I. Theory and Methods". In: *Mathematical Proceedings of the Cambridge Philosophical Society* 24.1 (1928), pp. 89–110. DOI: 10.1017/S0305004100011919.

[63] R.J. Bartlett and J.F. Stanton. *Application of Post-Hartree-Fock Methods: A Tutorial*. Vol. 5. VCH Publishers, 1990, pp. 65–169.

[64] R. Car and M. Parrinello. "Unified Approach for Molecular Dynamics and Density-Functional Theory". In: *Physical Review Letters* 55 (22 Nov. 1985), pp. 2471–2474. DOI: 10.1103/PhysRevLett.55.2471.

[65] C. Cohen-Tannoudji, B. Diu, and F. Laloe. *Quantum Mechanics, Volume 1*. Vol. 1-2. 1986.

[66] M. Born and R. Oppenheimer. "Zur Quantentheorie der Molekeln". In: *Annalen der Physik* 389.20 (1927), pp. 457–484. DOI: 10.1002/andp.19273892002.

[67] C. Kittel. *Introduction to Solid State Physics*. 8th ed. Wiley, 2004. ISBN: 9780471415268.

[68] W. Pauli. "Über den Zusammenhang des Abschlusses der Elektronengruppen im Atom mit der Komplexstruktur der Spektren". In: *Zeitschrift für Physik* 31.1 (1925), pp. 765–783.

[69] P.O. Löwdin. "Correlation Problem in Many-Electron Quantum Mechanics I. Review of Different Approaches and Discussion of Some Current Ideas". In: *Advances in Chemical Physics*. John Wiley & Sons, Ltd, 1958, pp. 207–322. ISBN: 9780470143483. DOI: 10.1002/9780470143483.ch7.

[70] A. Strich. "Quantum chemistry, 4th ed. By Ira N. Levine, Prentice-Hall, Englewood Cliffs, NJ, 1991, X+629 pp. Elementary quantum chemistry, 2nd ed. By Frank L. Pilar, McGraw Hill International Editions, New York, 1990, XVI+599 pp." In: *International Journal of Quantum Chemistry* 43 (1992), pp. 439–441.

[71] Péter Pulay. "Convergence acceleration of iterative sequences. The case of scf iteration". In: *Chemical Physics Letters* 73.2 (1980), pp. 393–398. ISSN: 0009-2614. DOI: 10.1016/0009-2614(80)80396-4.

[72] P. Pulay. "Improved SCF convergence acceleration". In: *Journal of Computational Chemistry* 3.4 (1982), pp. 556–560. DOI: 10.1002/jcc.540030413.

[73] Ron Shepard and Michael Minkoff. "Some comments on the DIIS method". In: *Molecular Physics* 105.19-22 (2007), pp. 2839–2848. DOI: 10.1080/00268970701691611.

[74] V. Fock. "Näherungsmethode zur Lösung des quantenmechanischen Mehrkörperproblems". In: *Zeitschrift für Physik* 61.1-2 (1930). cited By 1027, pp. 126–148. DOI: 10.1007/BF01340294.

[75] A. Szabo and N. S. Ostlund. *Modern Quantum Chemistry: Introduction to Advanced Electronic Structure Theory*. First. Mineola: Dover Publications, Inc., 1996.

[76] J. P. Martinez. "The Hartree-Fock method: from self-consistency to correct symmetry". In: *Annalen der Physik* 529.1-2 (2017), p. 1600328. DOI: 10.1002/andp.201600328.

[77] Kieron Burke. *The ABC of DFT*. Irvine, CA 92697, USA: Department of Chemistry, University of California, USA, 2007. URL: https://dft.uci.edu/doc/g1.pdf.

[78] M. Head-Gordon, J. A. Pople, and M. J. Frisch. "MP2 energy evaluation by direct methods". In: *Chemical Physics Letters* 153.6 (1988), pp. 503–506. ISSN: 0009-2614. DOI: 10.1016/0009-2614(88)85250-3.

[79] R. Krishnan et al. "Self-consistent molecular orbital methods. XX. A basis set for correlated wave functions". In: *The Journal of Chemical Physics* 72.1 (1980), pp. 650–654. DOI: 10.1063/1.438955.

[80] P. Hohenberg and W. Kohn. "Inhomogeneous Electron Gas". In: *Phys. Rev.* 136.3B (1964), B864. DOI: 10.1103/PhysRev.136.B864.

[81] W. Kohn and L.J. Sham. "Self-Consistent Equations Including Exchange and correlation effect". In: *Phys. Rev.* 140.4A (1965), A1133. DOI: 10.1103/PhysRev.140.A1133.

[82] J. P. Perdew et al. "Prescription for the design and selection of density functional approximations: More constraint satisfaction with fewer fits". In: *The Journal of Chemical Physics* 123.6 (2005), p. 062201. DOI: 10.1063/1.1904565.

[83] G. Kresse and J. Furthmüller. "Efficiency of ab-initio total energy calculations for metals and semiconductors using a plane-wave basis set". In: *Computational Materials Science* 6.1 (1996), pp. 15–50. ISSN: 0927-0256. DOI: 10.1016/0927-0256(96)00008-0.

[84] S. F. Boys. "Electronic Wave Functions. I. A General Method of Calculation for the Stationary States of Any Molecular System". In: *Proceedings of the Royal Society of London Series A* 200.1063 (Feb. 1950), pp. 542–554. DOI: 10.1098/rspa.1950.0036.

[85] J. C. Slater. "Atomic Shielding Constants". In: *Physical Review* 36.1 (July 1930), pp. 57–64. DOI: 10.1103/PhysRev.36.57.

[86] M. Dion et al. "Van der Waals Density Functional for General Geometries". In: *Physical Review Letters* 92.24 (June 2004), p. 246401. ISSN: 0031-9007, 1079-7114. DOI: 10.1103/physrevlett.92.246401.

[87] S. Grimme. "Semiempirical GGA-type density functional constructed with a long-range dispersion correction". In: *Journal of Computational Chemistry* 27.15 (2006), pp. 1787–1799. ISSN: 0192-8651, 1096-987X. DOI: 10.1002/jcc.20495.

[88] S. Grimme et al. "A consistent and accurate ab initio parametrization of density functional dispersion correction (DFT-D) for the 94 elements H-Pu". In: *The Journal of Chemical Physics* 132.15 (Apr. 2010), p. 154104. ISSN: 0021-9606, 1089-7690. DOI: 10.1063/1.3382344.

[89] S. Grimme, S. Ehrlich, and L. Goerigk. "Effect of the damping function in dispersion corrected density functional theory". In: *Journal of Computational Chemistry* 32.7 (Mar. 2011), pp. 1456–1465. ISSN: 0192-8651. DOI: 10.1002/jcc.21759.

[90] A. Ambrosetti and P. L. Silvestrelli. "van der Waals interactions in density functional theory using Wannier functions: Improved and coefficients by a different approach". In: *Physical Review B* 85.7 (Feb. 2012), p. 073101. ISSN: 1098-0121, 1550-235X. DOI: 10.1103/physrevb.85.073101.

[91] P. L. Silvestrelli. "Van der Waals interactions in density functional theory by combining the quantum harmonic oscillator-model with localized Wannier functions". In: *The Journal of Chemical Physics* 139.5 (Aug. 2013), p. 054106. ISSN: 0021-9606, 1089-7690. DOI: 10.1063/1.4816964.

[92] A. Boese et al. "New generalized gradient approximation functionals". In: *The Journal of Chemical Physics* 112 (Jan. 2000). DOI: 10.1063/1.480732.

[93] A. Boese and N. C. Handy. "New exchange-correlation density functionals: The role of the kinetic-energy density". In: *The Journal of Chemical Physics* 116.22 (2002), pp. 9559–9569. DOI: 10.1063/1.1476309.

[94] J. Tao et al. "Climbing the Density Functional Ladder: Nonempirical Meta–Generalized Gradient Approximation Designed for Molecules and Solids". In: *Physical Review Letters* 91 (14 Sept. 2003), p. 146401. DOI: 10.1103/PhysRevLett.91.146401.

[95] T. Van Voorhis and G. E. Scuseria. "A novel form for the exchange-correlation energy functional". In: *The Journal of Chemical Physics* 109.2 (1998), pp. 400–410. DOI: 10.1063/1.476577.

[96] D. R. Hamann, M. Schlüter, and C. Chiang. "Norm-Conserving Pseudopotentials". In: *Physical Review Letters* 43 (20 Nov. 1979), pp. 1494–1497. DOI: 10.1103/PhysRevLett.43.1494.

[97] P. E. Blöchl. "Projector augmented-wave method". In: *Physical Review B* 50 (24 Dec. 1994), pp. 17953–17979. DOI: 10.1103/PhysRevB.50.17953.

[98] X. Gonze. "A brief introduction to the ABINIT software package". In: *Zeitschrift für Kristallographie-Crystalline Materials* 220.5-6 (2005), pp. 558–562. DOI: 10.1524/zkri.220.5.558.65066.

[99] F. Bloch. "Memories of Electrons in Crystals". In: *Proceedings of the Royal Society of London. Series A, Mathematical and Physical Sciences* 371.1744 (1980), pp. 24–27. ISSN: 00804630. URL: http://www.jstor.org/stable/2990271.

[100] A.N. W et al. *Solid State Physics*. HRW international editions. Holt, Rinehart and Winston, 1976. ISBN: 9780030839931.

[101] G. Kresse, O. Dulub, and U. Diebold. "Competing stabilization mechanism for the polar ZnO(0001)-Zn surface". In: *Physical Review B* 68 (24 Dec. 2003), p. 245409. DOI: 10.1103/PhysRevB.68.245409.

[102] K. D. Brommer et al. "Ab initio theory of the Si(111)-(7×7) surface reconstruction: A challenge for massively parallel computation". In: *Physical Review Letters* 68 (9 Mar. 1992), pp. 1355–1358. DOI: 10.1103/PhysRevLett.68.1355.

[103] S. Goedecker, M. Boulet, and T. Deutsch. "An efficient 3-dim FFT for plane wave electronic structure calculations on massively parallel machines composed of multiprocessor nodes". In: *Computer Physics Communications* 154.2 (2003), pp. 105–110.

[104] E. O. Brigham. *The fast Fourier transform and its applications*. Prentice-Hall, Inc., 1988.

[105] F. Bottin et al. "Large-scale ab initio calculations based on three levels of parallelization". In: *Computational Materials Science* 42.2 (2008), pp. 329–336. ISSN: 0927-0256. DOI: 10.1016/j.commatsci.2007.07.019.

[106] A. D. Becke and K. E. Edgecombe. "A simple measure of electron localization in atomic and molecular systems". In: *Journal of Chemical Physics* 92.9 (May 1990), pp. 5397–5403. DOI: 10.1063/1.458517.

[107] A. Cammarata and J.M. Rondinelli. "Octahedral engineering of orbital polarizations in charge transfer oxides". In: *Physical Review B* 87.15 (2013), p. 155135. DOI: 10.1103/PhysRevB.87.155135.

[108] A. Cammarata and J.M. Rondinelli. "Covalent dependence of octahedral rotations in orthorhombic perovskite oxides". In: *Journal of Chemical Physics* 141.11 (2014), p. 114704. DOI: 10.1063/1.4895967.

[109] P. Paufler. "International tables for crystallography , Vol. D: Physical properties of crystals, Dordrecht/Boston/London: Kluwer Academic Publishers, 2003. ISBN 1-4020-0714-0". In: *Acta Crystallographica Section A - ACTA CRYSTALLOGR A* 62 (July 2006), pp. 316–318. DOI: 10.1107/S0108767306012001.

[110] A. Cammarata and T. Polcar. "Tailoring Nanoscale Friction in MX_2 Transition Metal Dichalcogenides". In: *Inorganic Chemistry* 54.12 (2015), p. 5739. DOI: 10.1021/acs.inorgchem.5b00431.

[111] M. Stengel, N. A. Spaldin, and D. Vanderbilt. "Electric displacement as the fundamental variable in electronic-structure calculations". In: *Nature Physics* 5.4 (Feb. 2009), pp. 304–308. ISSN: 1745-2473, 1745-2481. DOI: 10.1038/nphys1185.

[112] J. K. Sinha. "Modified Sawyer and Tower circuit for the investigation of ferroelectric samples". In: *Journal of Scientific Instruments* 42.9 (Sept. 1965), pp. 696–698. DOI: 10.1088/0950-7671/42/9/308.

[113] R. Resta. "Macroscopic polarization in crystalline dielectrics: the geometric phase approach". In: *Reviews of Modern Physics* 66 (3 July 1994), pp. 899–915. DOI: 10.1103/RevModPhys.66.899.

[114] R. D. King-Smith and D. Vanderbilt. "Theory of polarization of crystalline solids". In: *Physical Review B* 47 (3 Jan. 1993), pp. 1651–1654. DOI: 10.1103/PhysRevB.47.1651.

[115] F. Wilczek and A. Shapere. *Geometric Phases in Physics*. WORLD SCIENTIFIC, 1989. DOI: 10.1142/0613.

[116] I. Souza, J. Íñiguez, and D. Vanderbilt. "First-Principles Approach to Insulators in Finite Electric Fields". In: *Physical Review Letters* 89.11 (Aug. 2002), p. 117602. ISSN: 0031-9007, 1079-7114. DOI: 10.1103/physrevlett.89.117602.

[117] M. C. Payne et al. "Iterative minimization techniques for ab initio total-energy calculations: molecular dynamics and conjugate gradients". In: *Review of Modern Physics* 64 (4 Oct. 1992), pp. 1045–1097. DOI: 10.1103/RevModPhys.64.1045.

[118] R. W. Nunes and X. Gonze. "Berry-phase treatment of the homogeneous electric field perturbation in insulators". In: *Physical Review B* 63.15 (Mar. 2001), p. 155107. ISSN: 0163-1829, 1095-3795. DOI: 10.1103/physrevb.63.155107.

[119] J.W. Zwanziger et al. "Finite homogeneous electric fields in the projector augmented wave formalism: Applications to linear and nonlinear response". In: *Computational Materials Science* 58 (June 2012), pp. 113–118. ISSN: 0927-0256. DOI: 10.1016/j.commatsci.2012.01.028.

[120] G. Henkelman, Blas P. Uberuaga, and H. Jónsson. "A climbing image nudged elastic band method for finding saddle points and minimum energy paths". In: *The Journal of Chemical Physics* 113.22 (2000), pp. 9901–9904. DOI: 10.1063/1.1329672.

[121] H. Jonsson, G. Mills, and K. W. Jacobsen. "Nudged elastic band method for finding minimum energy paths of transitions". In: *Classical and Quantum Dynamics in Condensed Phase Simulations*, pp. 385–404. DOI: 10.1142/9789812839664_0016.

[122] A. Togo and I. Tanaka. "First principles phonon calculations in materials science". In: *Scripta Materialia* 108 (Nov. 2015), pp. 1–5.

[123] B. Schönfeld, J. J. Huang, and S. C. Moss. "Anisotropic mean-square displacements (MSD) in single-crystals of 2H- and 3R-MoS_2". In: *Acta Crystallographica B* 39.4 (1983), pp. 404–407. ISSN: 1600-5740. DOI: 10.1107/S0108768183002645.

[124] V.L. Kalikhman. "Characteristics of the crystal structure, electrophysical properties, and model of the valence band spectrum of laminar compounds of molybdenum disulfide type". In: *Inorganic Materials* 19.7 (1983), pp. 957–962.

[125] L.H. Brixner. "Preparation and properties of the single crystalline AB2-type selenides and tellurides of niobium, tantalum, molybdenum and tungsten". In: *Journal of Inorganic Nuclear Chemistry* 24.3 (1962), pp. 257–263. ISSN: 0022-1902. DOI: http://dx.doi.org/10.1016/0022-1902(62)80178-X.

[126] W.J. Schutte, J.L. De Boer, and F. Jellinek. "Crystal structures of tungsten disulfide and diselenide". In: *J. Solid State Chem.* 70.2 (1987), pp. 207–209. ISSN: 0022-4596. DOI: http://dx.doi.org/10.1016/0022-4596(87)90057-0.

[127] V. L. Kalikhman. In: *Neorganicheskie Materialy* 19.7 (1983), pp. 1060–1065.

[128] A. A. Yanaki and V. A. Obolonchik. In: *Inorganic Materials* 9.12 (1973), pp. 1855–1858.

[129] A. D. Becke and E. R. Johnson. "A simple effective potential for exchange". In: *The Journal of Chemical Physics* 124.22 (2006), p. 221101. DOI: 10.1063/1.2213970.

[130] G. Levita et al. "First-principles comparative study on the interlayer adhesion and shear strength of transition-metal dichalcogenides and graphene". In: *Physical Review B* 92 (8 Aug. 2015), p. 085434. DOI: 10.1103/PhysRevB.92.085434.

[131] J. P. Perdew, K. Burke, and M. Ernzerhof. "Generalized Gradient Approximation Made Simple". In: *Physical Review Letters* 77.18 (Oct. 1996), pp. 3865–3868. ISSN: 0031-9007, 1079-7114. DOI: 10.1103/physrevlett.77.3865.

[132] F. Belviso et al. "Effect of electric fields in low-dimensional materials: Nanofrictional response as a case study". In: *Physical Review B* 102 (15 Oct. 2020), p. 155433. DOI: 10.1103/PhysRevB.102.155433.

[133] A. Cammarata and Tomas Polcar. "Control of energy dissipation in sliding low-dimensional materials". In: *Physical Review B* 102 (8 2020), p. 085409. DOI: 10.1103/PhysRevB.102.085409.

[134] D.C. Wallace. *Thermodynamics of Crystals*. Dover books on physics. Dover Publications, 1998. ISBN: 9780486402123.

[135] H. Goldstein. *Classical Mechanics*. Addison-Wesley, 1980.

[136] J. Missaoui et al. "Effect of Noninteracting Intercalants on Layer Exfoliation in Transition-Metal Dichalcogenides". In: *Physical review Applied* 15 (6 June 2021), p. 064041. DOI: 10.1103/PhysRevApplied.15.064041.

[137] Z. Ding et al. "Intercalation and Solution Processing of Bismuth Telluride and Bismuth Selenide". In: *Advanced Materials* 13.11 (2001), pp. 797–800. DOI: 10.1002/1521-4095(200106)13:11<797::AID-ADMA797>3.0.CO;2-U.

[138] L. Li et al. "Electric field driven exfoliation of MoS_2". In: *Journal of Alloys and Compounds* 862 (2021), p. 158551. ISSN: 0925-8388. DOI: 10.1016/j.jallcom.2020.158551.

[139] F. Zhang et al. "Electric field induced semiconductor-to-metal phase transition in vertical $MoTe_2$ and $Mo_{1-x}W_xTe_2$ devices". In: *arXiv: Mesoscale and Nanoscale Physics* (2017).

[140] E. Riedo and E. Gnecco. "Thermally activated effects in nanofriction". In: *Nanotechnology* 15.4 (Mar. 2004), S288–S292. DOI: 10.1088/0957-4484/15/4/032.